

**UNIVERSITÀ DEGLI  
STUDI DI PADOVA**

Facoltà di Scienze MM.NN.FF.  
Facoltà di Ingegneria

**ISTITUTO NAZIONALE  
DI FISICA NUCLEARE**

Laboratori Nazionali di Legnaro

*in collaboration with Confindustria Veneto*

**MASTER THESIS**

in

**“Surface Treatments for Industrial Applications”**

**Thermo Mechanical Design of a High Power Neutron  
Converter**

*Supervisor: Dr. Luigi B. Tecchio  
Co-Supervisor: Dr. Vincenzo Palmieri*

*Student: Eng. Gabriela Acosta  
Matr. N° 938768*

Academic Year 2009-10



## **ABSTRACT**

The subject of present Master Work is the thermomechanical design of a high power neutron converter for the SPIRAL2 Facility, which is being developed in collaboration with the INFN – Italy and GANIL – France.

The main objective is description of an general overview about the project and its main goals. The SPIRAL2 is a linear particle accelerator for the production of high intensity exotic ion beams. It will be under operation in the existing installations of the GANIL Institute in Caen, France. Therefore a neutron converter target has been designed and it must produce 1014 fissions/second, at a working temperature up to 1850°C. Available deuteron beam for the operation of this accelerator has a power up to 200 kW and all the calculations and tests around the main critical elements of the neutron converter module are explained in the next sections of this document.

---

# Summary

<b>SUMMARY</b> .....	<b>I</b>
<b>SUMMARY OF FIGURES</b> .....	<b>II</b>
<b>SUMMARY OF TABLES</b> .....	<b>V</b>
<b>1. CHAPTER 1. INTRODUCTION</b> .....	<b>1</b>
<b>2. CHAPTER 2. THE NEUTRON CONVERTER</b> .....	<b>2</b>
2.1. REQUIREMENTS AND PERFORMANCES .....	2
2.2. PRODUCT DESCRIPTION .....	4
2.3. THE NEUTRON CONVERTER DESIGN .....	7
2.3.1. The Neutron Converter.....	7
2.3.2. Cooling System .....	10
2.3.3. The Delay Window .....	12
2.3.4. Beam Collimator .....	15
2.3.5. Electrical Structure .....	16
2.3.6. Protection and Prevention .....	17
2.3.7. Maintenance and Waste Management .....	17
2.4. ADDITIONAL SPECIFICATIONS .....	18
2.4.1. Driver And Primary Beams.....	18
2.4.2. Production Hall .....	18
2.4.3. Experimental Area .....	19
<b>3. CHAPTER 3. FUNDAMENTAL CONCEPTS: MATERIAL ACTIVATION</b> .....	<b>20</b>
3.1. CONVERTER ACTIVATION .....	20
3.2. DELAY WINDOW ACTIVATION .....	21
3.3. RADIATION DAMAGE.....	23
3.3.1. Effect of Irradiation on Thermal and Mechanical Properties of Graphite.....	24
3.3.2. Graphite Lattice Defects .....	<b>Errore. Il segnalibro non è definito.</b>
3.3.3. Estimation of a radiation durability of graphite and steel .....	35
3.4. LIFE TIME.....	38
3.5. MATERIAL SELECTION .....	39
<b>4. CHAPTER 4. THERMOMECHANICAL DESIGN</b> .....	<b>42</b>
4.1. NEUTRON CONVERTER .....	43
4.1.1. 50 kW Neutron Converter.....	44
4.1.2. 200 kW Neutron Converter .....	49
4.1.3. Cooling Panels .....	55
4.1.3.1. 50 kW Cooling Panel .....	57
4.1.3.2. 200 kW Cooling Panel .....	62
4.2. LEAD HEATING SYSTEM .....	68
<b>5. CHAPTER 5. TESTING AND MEASUREMENTS</b> .....	<b>71</b>
5.1. GRAPHITE'S EVAPORATION RATE TEST.....	71
5.2. DELAY WINDOW TEST.....	76
5.2.1. Experimental set-up .....	76
5.2.2. Experimental results.....	79
5.2.3. Long term test .....	82
5.3. BALL BEARINGS TEST .....	84
5.3.1. Experimental Set-up.....	84
5.3.2. Experimental Results .....	88
5.4. ADDITIONAL EXPERIMENTS .....	92
<b>6. CONCLUSIONS</b> .....	<b>94</b>
<b>7. REFERENCES</b> .....	<b>95</b>

---

## Summary of Figures

Figure 2.1. Schematic View of SPIRAL-2 Facility .....	2
Figure 2.2. Detail of the Production Module Location inside SPIRAL-2 Facility.....	3
Figure 2.3. A conceptual sketch of the neutron production target. ....	3
Figure 2.4. Schematic view of the 50 kW neutron converter.....	4
Figure 2.5. View of the neutron converter integrated inside the production module.....	5
Figure 2.6. Transversal cut of the neutron converter layout .....	6
Figure 2.7. A general view of the NCM and its internal components.....	7
Figure 2.8. A sketch of the 200 kW (left) and 50 kW converter (right).....	7
Figure 2.9. A view of the cooling panels. ....	7
Figure 2.10. Rotation system for the 50 kW converter. For the 200 kW converter the rotation systems demand a shorter shaft. The system has been conceived to replace the block with bearings keeping the converter in place. ....	10
Figure 2.11. A sketch of the working principle of the special connectors for water cooling and liquid lead system .....	11
Figure 2.12. Connecting solution for the water cooling system and delay window on the servitude flange. ....	12
Figure 2.13 The delay window set up for the 50 kW converter. The Delay Window is integrated in the rear cooling panel and the liquid lead play also the role of coolant. ....	13
Figure 2.14. The production module with installed the beam collimator (left) and the set up for the 50 kW converter including the water cooled graphite tube (right) . ....	16
Figure 3.1. - Decay time of the activity at the converter level.....	21
Figure 3.2. - Total activity evolution of the radionuclide produced in the liquid lead alloy of the delay window .....	22
Figure 3.3.- Activity evolution of long-lived radionuclide produced in the liquid lead alloy.....	22
Figure 3.4: Left- thermal conductivity vs. temperature for different graphite materials (data of Tanabe), right – steady-state temperature field over unirradiated converter made of ETP-10 graphite. ....	24
Figure 3.5. Transient analysis of ETP-10 graphite irradiated to 0.02 dpa. Left column– temperature ( $^{\circ}\text{C}$ ), right column – stress distribution (Pa). Data taken at 0.5 s (top raw), 400 s (middle raw), and 1200 s (bottom raw) .....	25
Figure 3.6: Left – maximum converter temperature vs. time, right – maximum thermo-mechanical stress vs. time for irradiated and unirradiated ETP-10 graphite.....	26
Figure 3.7. Left – MPG-6 graphite heat conductivity vs. neutron fluence at $T = 950 - 1050^{\circ}\text{C}$ . 1 – $T_{\text{measure}} = T_{\text{irrad}}$ ; 2 – $T_{\text{measure}} = 20^{\circ}\text{C}$ . Right – thermal conductivity curves used in the analysis. ....	27
Figure 3.8. Transient analysis of MPG-6 irradiated graphite at fluence $4 \cdot 10^{21} \text{ n/cm}^2$ . Left column– temperature ( $^{\circ}\text{C}$ ), right column – stress distribution (Pa). Data taken at 0.5 s (top raw), 400 s (middle raw), and 1200 s (bottom raw). ....	28
Figure 3.9 Left – maximum converter temperature vs. time, right – maximum thermo-mechanical stress vs. time for irradiated and unirradiated MPG-6 graphite. ....	28
Figure 3.10. The spatial distribution of displacement rate from deuterium nuclei; the average number of displaced nuclei per one deuterium nuclei is 74. ....	31
Figure 3.11. The spatial distribution of displacement rate from carbon nuclei; the average number of displaced nuclei per one deuterium nuclei is 114. ....	31
Figure 3.12. The spatial distribution of nuclear displacement rate; the average number of displaced nuclei per one deuterium nuclei is 188 (52 replacements). ....	31
Figure 3.13. The spatial distribution of nuclear displacement rate .....	32
Figure 3.14. Spatial distribution of implanted deuteron rate .....	32
Figure 3.15. Spatial distribution of absorbed dose in the graphite target.....	32
Figure 3.16. X-ray pattern of fine-grained dense CGD graphite samples in semilogarithmic scale. Curves 1 and 2 correspond to a compact plate and ground sample, respectively. The 002 peak height is appreciably larger in the former case, since the plate is characterized by the texture, i.e., the preferred orientation in the [001] direction. For POCO and MPG-6 graphite samples, x-ray patterns are almost identical to curve 2.....	34
Figure 3.17. Lifetime dependence vs return temperature for MPG samples (at the left) and CGD samples (on the right). ....	39
Figure 4.1. Gauss Distribution of Deuteron Primary Beam of 50kW.....	42
Figure 4.2. Gauss Distribution of Deuteron Primary Beam of 200kW.....	42
Figure 4.3. 50 kW Graphite Wheel Model .....	44
Figure 4.4. 50 kW Graphite Wheel. Geometry and meshing.....	45
Figure 4.5. 50 kW Graphite Wheel Temperature Distribution. ....	45
Figure 4.6.. 50 kW Graphite Wheel . Deformation in X direction.....	46
Figure 4.7. 50 kW Graphite Wheel . Deformation in Y direction.....	46
Figure 4.8. 50 kW Graphite Wheel . Deformation in Z direction .....	47
Figure 4.9. 50 kW Graphite Wheel . Total Deformation .....	47
Figure 4.10. Total Stress Von Mises.....	48

---

Figure 4.11. 200 kW Graphite Wheel Virtual Model .....	49
Figure 4.12. 200 kW Graphite Wheel Virtual Model .....	49
Figure 4.13. 200 kW Graphite Wheel Temperature Distribution. ....	50
Figure 4.14. 200 kW Graphite Wheel . Deformation in X direction.....	51
Figure 4.15. 200 kW Graphite Wheel . Deformation in Y direction.....	51
Figure 4.16. 200 kW Graphite Wheel . Deformation in Z direction .....	52
Figure 4.17. 200 kW Graphite Wheel .Total Deformation .....	52
Figure 4.18 Graphite Wheel .Total Stress Von Mises .....	53
Figure 4.19. Graphite Wheel .Maximum Stress.....	53
Figure 4.20. 50 kW Assembly Front View .....	55
Figure 4.21. 50 kW Assembly Rear View .....	55
Figure 4.22. 50 kW Assembly Half Section .....	56
Figure 4.23. 200 kW Assembly Half Section .....	56
Figure 4.24. 50kW Metal Delay Window Temperature .....	57
Figure 4.25. 50kW Liquid Lead Temperature .....	57
Figure 4.26. 50kW Rear Panel Temperature.....	58
Figure 4.27. 50kW Front Panel Temperature .....	58
Figure 4.28. 50kW Rear Panel Water Temperature.....	59
Figure 4.29. 50kW Front Panel Water Temperature.....	59
Figure 4.30.. 50kW Front Panel Stress .....	60
Figure 4.31. 50kW Rear Panel Stress .....	60
Figure 4.32. 50kW Front Panel Deformation .....	61
Figure 4.33. 50kW Rear Panel Deformation .....	61
Figure 4.34. 200kW Metal Delay Window Temperature. ....	62
Figure 4.35. 200kW Liquid Lead Temperature. ....	62
Figure 4.36.. 200kW Rear Panel Temperature.....	63
Figure 4.37. 200kW Front Panel Temperature .....	63
Figure 4.38. 200kW Rear Panel Water Temperature .....	64
Figure 4.39. 200kW Rear Panel Water Temperature .....	64
Figure 4.40. 200kW Front Panel Stress .....	66
Figure 4.41. 200kW Rear Panel Stress .....	66
Figure 4.42. 200kW Front Panel Deformation .....	67
Figure 4.43. 200kW Rear Panel Deformation.....	67
Figure 4.44. Delay Window Arrangement.....	68
Figure 4.45. Delay Window Section.....	68
Figure 4.46. Liquid Lead and Nitrogen Pipe Section .....	69
Figure 4.47. Liquid Lead Temperature Distribution.....	70
Figure 4.48. Nitrogen Temperature Distribution .....	70
Figure 5.1. Sample geometry and detectors positioning .....	72
Figure 5.2. Graphite’s evaporation rate in $\text{kg/m}^3\text{s}$ .....	75
Figure 5.3. Graphite’s evaporation rate in $\text{mm/month}$ .....	75
Figure 5.4 Graphite’s evaporation for different commercial graphites.....	76
Figure 5.5. Set up for testing the “Delay Window” .....	77
Figure 5.6. A sketch of the up for testing the “Delay Window” .....	77
Figure 5.7. The Delay Window equipped of heating wires before the assembling of the test bench. ....	79
Figure 5.8. The pressure detector ready to be tested.....	79
Figure 5.9. The liquid lead jet flowing from the Delay Window at the beginning of the measurement (left) and after 5 minutes (right). ....	81
Figure 5.10. Visual inspection of the delay window, after the disassembling of the set up.....	81
Figure 5.11. Visual inspection of the flange in front to the Delay Window, after the disassembling of the set up. ....	82
Figure 5.12. A sketch of the set-up for the long term tests of the Delay Window. ....	83
Figure 5.13. A picture of the set-up for the long term experiment of the Delay Window. ....	84
Figure 5.14 – View of the test bench. ....	85
Figure 5.15. Picture of the test bench at the Legnaro National Laboratories.....	86
Figure 5.16. Bearing WSP15312RT4K4297. LEFT: mechanical drawing, RIGHT: photograph of the bearings installed on the test set-up. ....	87
Figure 5.17 - Bearing W6001RT4K4298. LEFT: mechanical drawing design, RIGHT: photograph of the bearings installed on the test set-up.....	88

---

Figure 5.18. - Detail of W6002RT4K4296 bearing. LEFT: mechanical drawing. CENTER: photography of the shaft ending with the conic gear corresponding to the mechanical drawing. RIGHT: photography of the conic gear connected to the electrical motor. ....	88
Figure 5.19. An example of the display of the data of the test bench observed during the 90 days-experiment. Graphs in function of time: 1) temperature, 2) rotation frequency, 3) motor current, and 4) pressure in vacuum chamber; and indicators of the instant value of the main parameters are also shown. ....	89
Figure 5.20 - <i>Results of 90 days experiment; motor current, rotation frequency and shaft temperature are reported in function of time (days).</i> ....	90
Figure 5.21. Vibration base-level with only vacuum pump turned ON. Measurement duration 30 minutes. Results are shown as peaks and RMS of the acceleration in $m/s^2$ in function of time. Red: peak signal, Blue: RMS signal. ....	91
Figure 5.22. An example of vibration analysis of the test bench for 90 days experiment. Results are shown as peaks and RMS of the acceleration in $m/s^2$ in function of time. Duration of measurement: 2 hours. Red: peaks signal, Blue: RMS signal. ....	91
Figure 5.23. Variation of current and frequency at $T \sim 320^\circ C$ . The experiments starts the 93th day of operation. ....	92
Figure 5.24. An example of vibration analysis of the last three weeks experiments. Results are shown as peaks and RMS of the acceleration in $m/s^2$ in function of time. Duration of measurement: 2 hours. Red: peaks signal, Blue: RMS signal. ....	93

---

## Summary of Tables

Table 2.1. Geometrical and thermo-mechanical parameters for the 50 kW neutron converter. ....	7
Table 2.2. Geometrical and thermo-mechanical parameters for the 200 kW neutron converter.....	8
Table 2.3. Main physical, thermal and mechanical properties of the POCO graphite. ....	8
Table 2.4. Main parameters of the delay window. ....	13
Table 2.5. Main thermal parameters of the delay window.....	14
Table 2.7. Composition of the PbSn alloy. ....	15
Table 3.1. Maximum converter temperatures for irradiated and unirradiated ETP-10 graphite converter. Data of Tanabe, steady-state analysis. ....	25
Table 3.2. Maximum converter temperatures for irradiated and unirradiated MPG-6 graphite converter. Data of VNIITF for $4 \cdot 10^{21}$ n/cm <sup>2</sup> fluence; steady-state analysis. ....	28
Table 3.3. Radiation damage induced on the converter assembly. ....	29
Table 3.4. Calculation results for the model system [1]. ....	36
Table 3.5. Heat resistant characteristics of the Russian dispersion-hardening steels.....	40
Table 3.6. Composition of heat resistant Russian steels (in mass %) in accordance with GOST 5632-72 GOST 5632-72. Corrosion-resistant, heat-resistant and creep resisting high-alloy steel and alloys. ....	41
Table 3.7. Composition (in mass %) of German, Japanese and USA analogues of a the Russian heat resistant steel. ...	41
Table 4.1. 50 kW Gauss Beam Distribution. Number of Particles and Power .....	44
Table 4.2. Summary of Maximum Values for Temperature and Stress for 50 kW Neutron Converter.....	48
Table 4.3. 200 kW Gauss Beam Distribution. Number of Particles and Power .....	50
Table 4.4. Summary of Maximum Values for Temperature and Stress for 200 kW Neutron Converter.....	54
Table 4.5. Water Parameters for Cooling Pannels .....	65
Table 4.6. Lead Parameters for Delay Window .....	69
Table 5.1. Main parameters of graphites used for the measurements .....	73
Table 5.2. Measured QCM frequency shift, the received graphite mass on the detector.....	73
Table 5.3. Measured QCM frequency shift, the received graphite mass on the detector surface and the graphite evaporation rate for the POCO AFS (ZFX-5Q) in function of the temperature .....	74
Table 5.4. Measured QCM frequency shift, the received graphite mass on the detector surface and the graphite evaporation rate for the 1116PT Carbone Lorraine graphite, in function of the sample temperature.....	74
Table 5.5. Main design parameter of the delay window .....	80
Table 5.6. Main results of the experiment on the Delay Window prototype .....	80
Table 5.7 - <i>Ball bearing characteristics.</i> .....	87
Table 5.8. Setting of the parameters for the 90 days experiment. ....	89
Table 5.9. Setting of parameters for the additional experiments. ....	92

---

## CHAPTER 1. INTRODUCTION

The SPIRAL2 project aims at delivering high intensities of rare isotopes beams by adopting the suitable method for each desired radioactive beam. The RIB's will be produced by the ISOL "Isotope Separation On-Line" method via a converter (i.e. neutron converter) or by direct irradiation. The combination of both methods (i.e. via fission induced by fast neutrons in a Uranium Carbide target or by direct bombardment of the fissile material) will allow covering broad areas of the nuclear chart. Moreover, it will give an opportunity to carry out promptly significant experiments and activities in both fundamental and applied Nuclear Physics (medicine, biology, solid state, etc)

Among the different variants of the neutron converter, the one based on a rotating solid disk seems quite attractive from the safety point of view, simplicity of technological production and relatively low cost. Considering this design several materials have been studied to be used as a converter material. From the preliminary studies arises that dense graphite used as the converter's material allows the production of high intensity neutron flux and, at the same time, the heat removal from the converter by means of radiation cooling.

Thermo-mechanical simulations have been performed in order to determine the basic geometry and physical characteristics of the neutron converter for SPIRAL-2 facility at GANIL (see Figure 2.1 and Figure 2.2), to define the appropriate beam power distribution and to predict the converter behaviour under the deuteron beam of nominal parameters (40 MeV, 5mA, 200 kW). To study the main physical and mechanical properties and serviceability under operating conditions, several kinds of graphite have been analysed and tested.

---

## CHAPTER 2. THE NEUTRON CONVERTER

### 2.1. Requirements and Performances

The neutron converter has to produce an intense flux of fast neutrons, mainly in the forward direction respect to the incoming deuteron beam, enable to induce up to  $10^{14}$  fissions per second in the Uranium Carbide target located upstream the converter. The primary beam is constituted by deuterons with 40 MeV energy and current 5 mA (200 kW) [11]

The neutron converter is conceived as a high speed rotating target (Figure 2.3), which limits the peak surface temperature of converter materials well below 2000 °C. Nuclear graphite made of natural carbon is a very suitable material for neutron converter. In fact,  $^{nat}\text{C}(d,n)$  reaction is very prolific, especially in the forward direction where the neutron yield is comparable to that generated by other light material converters. The thermal properties of graphite (melting point of 3632 °C) allow a compact geometry and the power dissipation from the converter does not demand a sophisticated cooling system but simply the heat is exchanged by radiation with the water cooled panels. The diameter of the wheel is of 120 cm, and the rotation is carried out by an electrical motor by means of a rotary feedthrough and bearings system

The thermal power (200 kW) deposit in the converter material is dissipated only by thermal radiation. Heat removal from production module volume is carried out by water circulating inside cooling panels, fixed to the module's walls.

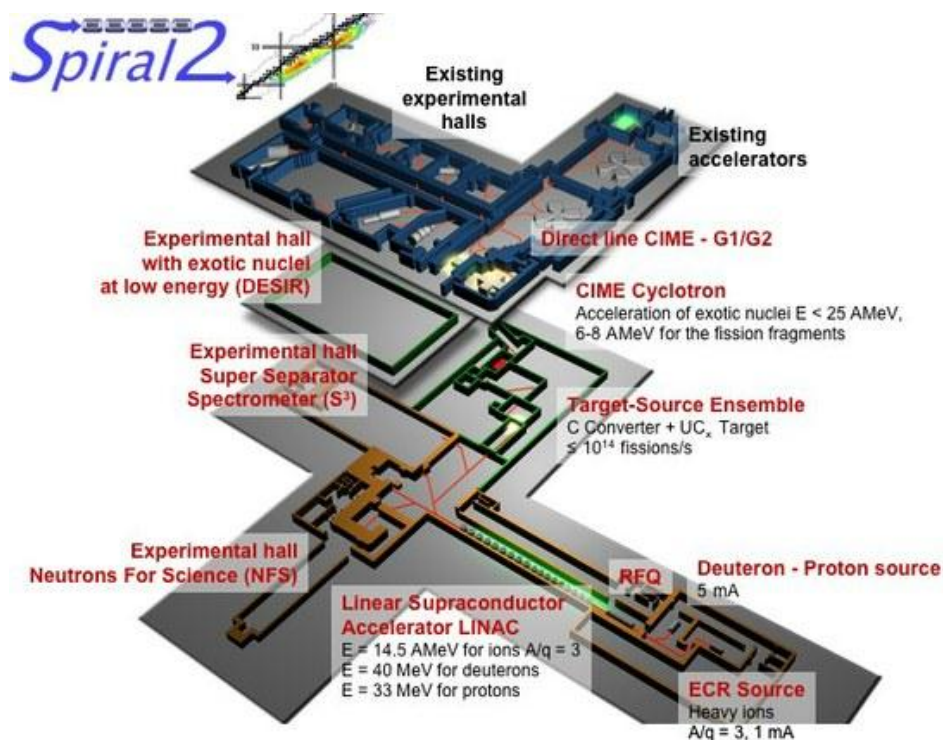
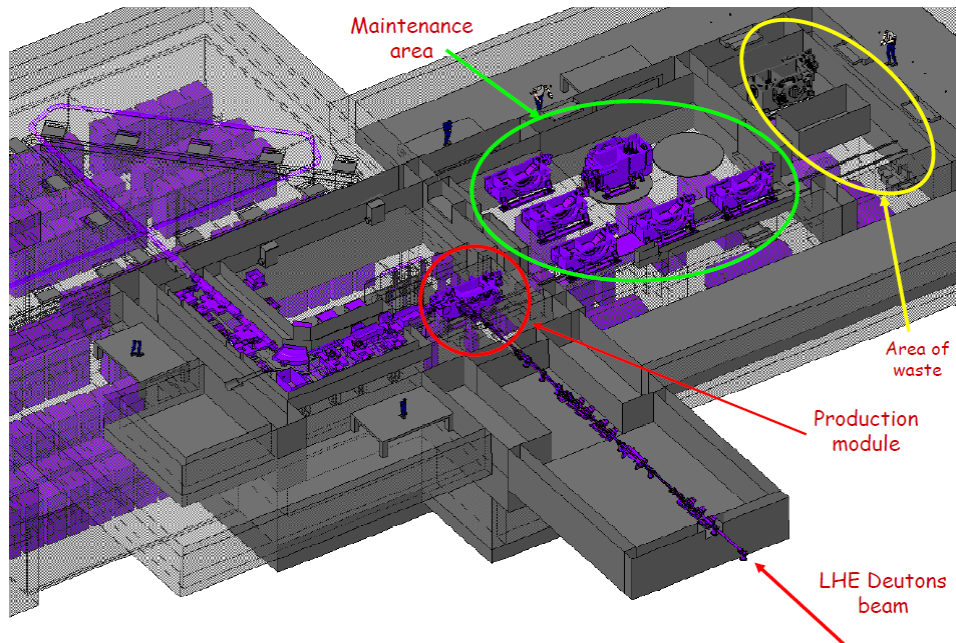
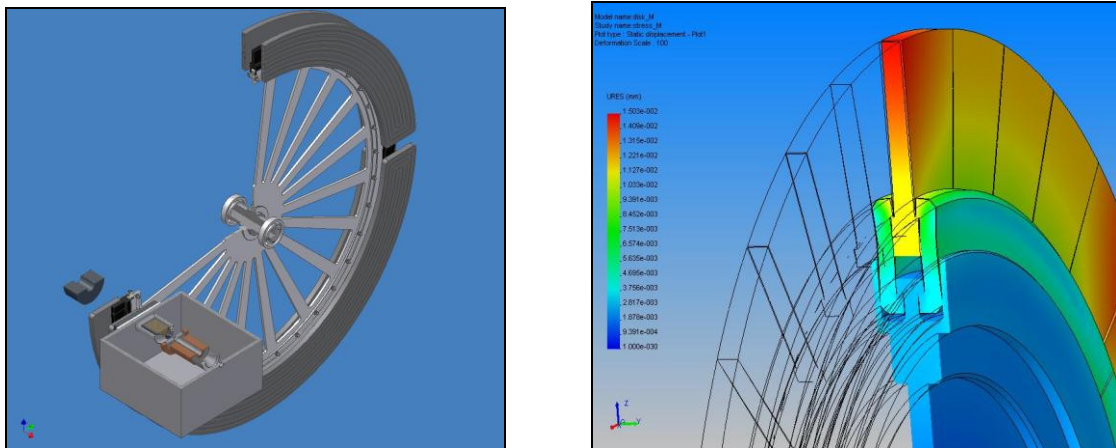


Figure 2.1. Schematic View of SPIRAL-2Faciliy



**Figure 2.2. Detail of the Production Module Location inside SPIRAL-2 Facility**

The facility, at the beginning and for a relatively long period of time necessary to assess its performances, will be operated at reduced power, up to 50 kW. The suitable neutron converter has been studied for this first period of operations and was designed based on the experience of the 70 kW prototype



**Figure 2.3. A conceptual sketch of the neutron production target.**

In the next sections the design of 200 kW converter will be presented as the general set up for the SPIRAL2 facility. The 50 kW version represents a particular case of the general one. The design of the converter module (mechanical frame, cooling system, delay window, remote handling,...) has been conceived to house both the 50 kW or 200 kW versions, depending on the user requirements. In practice, to switch from 50 kW to 200kW has to be changed only the graphite wheel, taking an advantage of the same module.

## 2.2. Product Description

The neutron converter design is based on a high speed rotating wheel which operates within the temperature range of 1650 - 1850 °C. Graphite made of natural carbon has been selected as converter material to be employed with deuteron beam. Actually, two different graphite are considered the best candidates: R6510 from SGL Carbon s.p.a. and AXF-5Q/TM-1 from POCO Graphite inc.

The actual design for the 50 kW converter (Figure 2.4) is based on a solid graphite disk with apertures and separation between the areas of beam position. The disk is clamped to the shaft by six spokes steel made. The converter diameter is 520 mm. The converter material thickness and its active width are 8 mm and 80 mm, respectively; the metal spoke diameter is of 7 mm. Rotation frequency range of 7 – 15 Hz provides the safety value of the temperature gradient per one turn (10°C – 20°C).

The heat power induced by the deuteron beam in the converter material is dissipated only by thermal radiation by means of water cooling panels surrounding the converter. The neutron converter is operated under vacuum and its rotational motion is generated by an electrical motor. The electrical motor has been conceived to operate in vacuum and is located inside the production module. Being the graphite evaporation rate a function of temperature, the limit of the operation temperature was fixed to have a negligible amount of evaporated material. This consideration fixes the sizes of the wheel and the beam spot on the carbon converter.

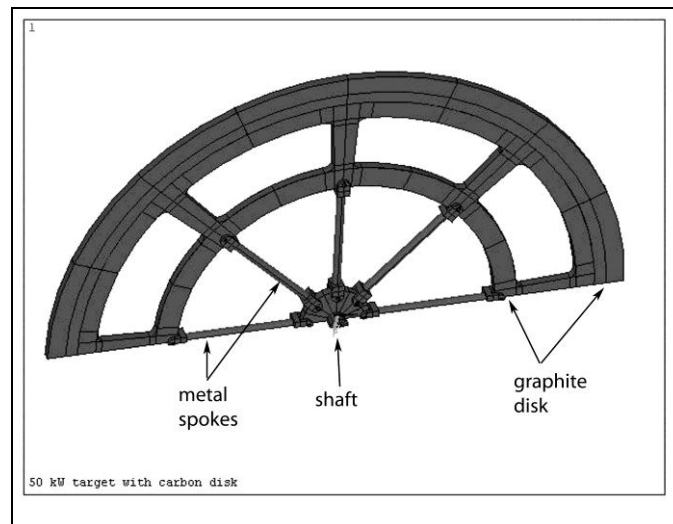


**Figure 2.4. Schematic view of the 50 kW neutron converter.**

The 200 kW converter has an analogous construction but, to keep the temperature below the 1850 °C, its diameter was increased up to 1200 mm, while the thickness and the width of the converter material are of 8 mm and 100 mm, respectively.

The deuteron beam size has been chosen 20,4 mm ( $6\sigma$ ) and 42,6 mm ( $6\sigma$ ) with a Gaussian profile on horizontal and vertical direction, for both 50 kW and 200 kW respectively, according to Ref. [8]. For safety reasons the maximum converter temperature has been limited to 1850 °C.

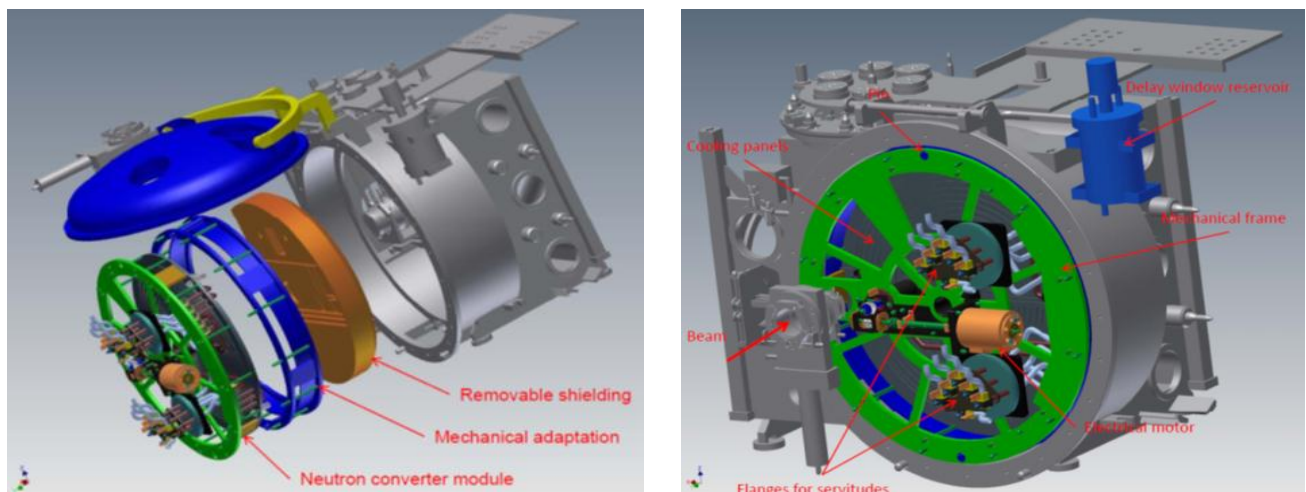
To protect the UCx target from the interaction with the deuteron beam, a Delay Window is located in between the neutron converter and the UCx target and is integrated on the rear cooling panel of the converter assembly. A continuous flow of Liquid Lead at high temperature ( $>320$  °C) is circulating through the Delay Window with a velocity of 1,5 m/s. In case of failure of the neutron converter the deuteron beam impinge directly on the wall of the Delay Window which will be melted in a very short time (5 ms). Then the deuteron beam is dumped in the liquid lead jet. The thickness of the Delay Window is 5mm of lead, enough to stop completely the deuteron beam within a period of 60s, that is the time required to stop the beam operation in case of failures.

The neutron converter, as well as the Uranium Carbide target and the ion source, is placed inside a module named “production module”, which is surrounded by the biological shielding. In practice, the “production module” is a shielded box that contain all the sub-system dedicated to the production of radioactive ions and that became highly radioactive and contaminated. Removal of the “production module” has to be done only by remote handling device..

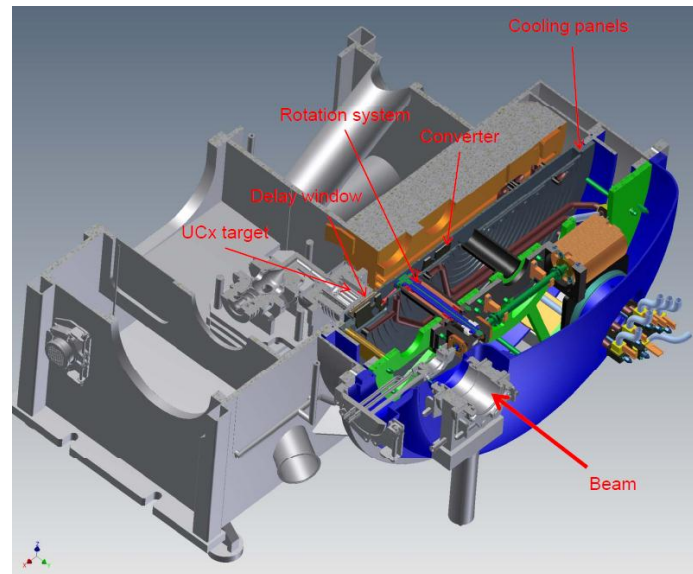
The current design integrating the neutron converter inside the production module is shown in

Figure 2.5; while a transversal cut of the production module is showing more in detail the converter layout (see Figure 2.6). The distance between the converter and the UC target is 43,5 mm.

To be remotely manipulated the converter design has been conceived as a “sub-module” which can be handled independently from the production module. This “sub-module” (NCM) integrates the converter it-self, the rotation system, the cooling panels, the delay window and all the servitudes required to operate the converter.



**Figure 2.5. View of the neutron converter integrated inside the production module**



**Figure 2.6. Transversal cut of the neutron converter layout**

The NCM has been conceived to house both, the 50 kW and 200 kW converter, depending on the requests, just replacing the graphite wheel of the corresponding size. The cooling panels, the delay window, the driving motor and the servitudes remain unchanged and may be re-used several times.

The characteristic of the removable shielding (see

Figure 2.5 left) allows the use of the NCM for different target configurations, by modifying the “mechanical adaptation” ring. Figure 2.7 shows more in detail the internal components of the neutron converter module;

Figure 2.8 shows the virtual model for both neutron converter, while Figure 2.9 shows the internal view of the cooling panels with their respective converters.

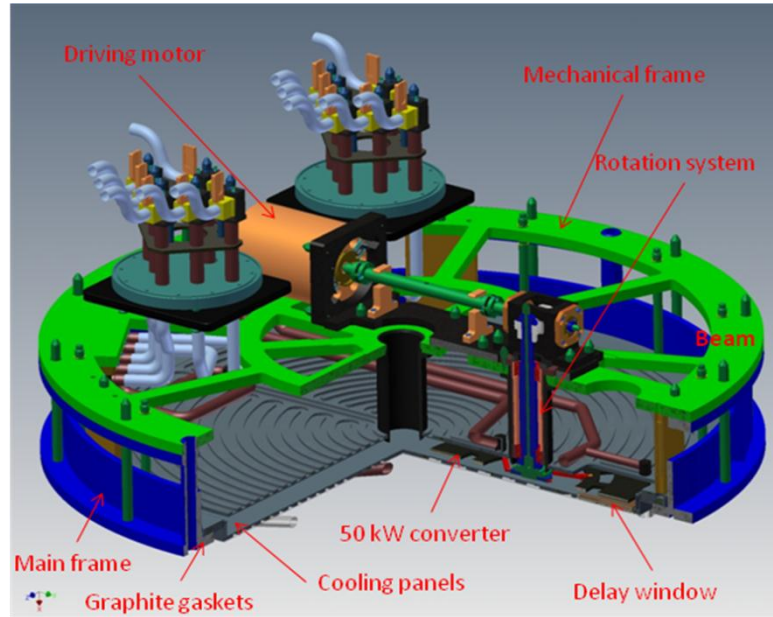


Figure 2.7. A general view of the NCM and its internal components

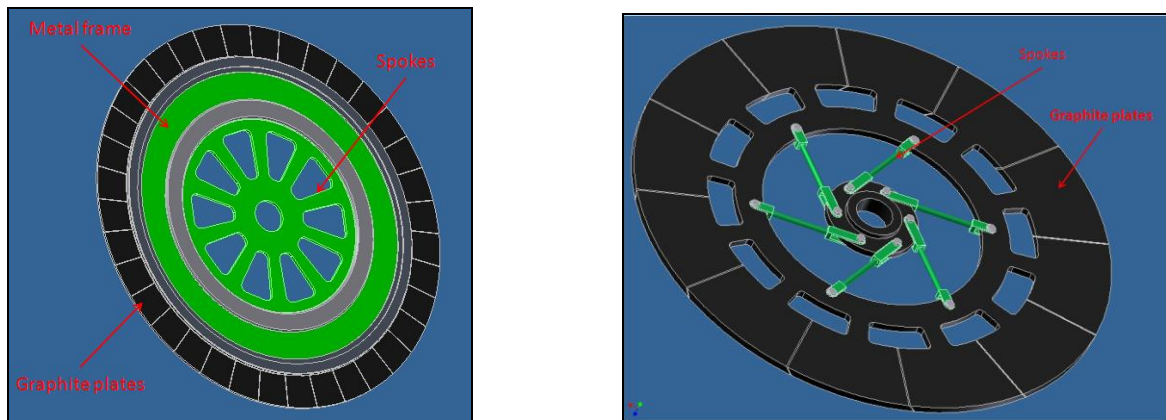


Figure 2.8. A sketch of the 200 kW (left) and 50 kW converter (right)

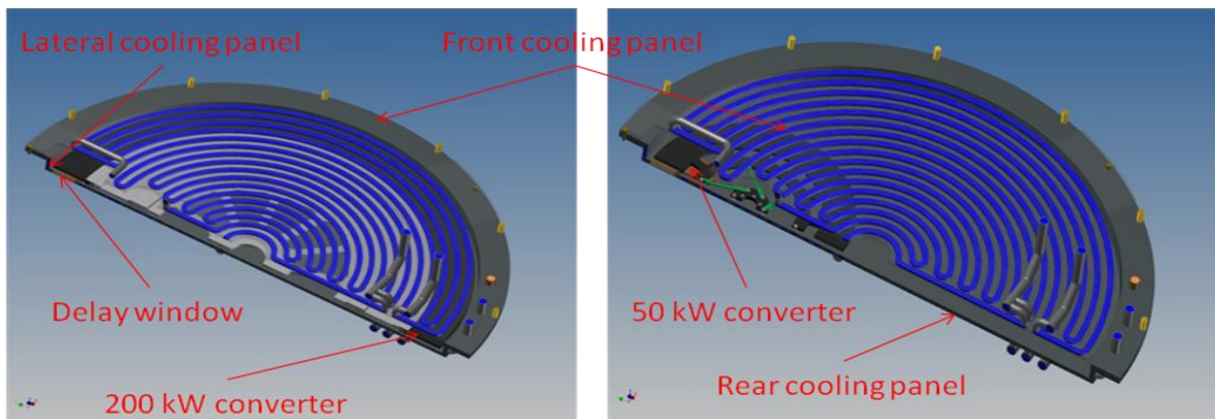


Figure 2.9. A view of the cooling panels.

## 2.3. The Neutron Converter Design

### 2.3.1. The Neutron Converter

The main geometrical and thermo-mechanical parameters of neutron converter are listed in Table 2.1 and Table 2.2, correspondingly.

**Table 2.1. Geometrical and thermo-mechanical parameters for the 50 kW neutron converter.**

Max. converter temp. [ $^{\circ}$ C]	Target diameter [cm]	Max. metal temp. [ $^{\circ}$ C]	Max. t-m stress in graphite [Pa]	Max. t-m stress in metal [Pa]	Max. inertial stress (10 Hz) [Pa]
1740	52	405.5	$2.62 \times 10^7$	$5 \times 10^6$	$3.5 \times 10^6$
Material	Max. t/m stress von Mises [Pa]	Max. t/m stress X-component [Pa]	Max. t/m stress Y-component [Pa]	Max. t/m stress Z-component [Pa]	Max. deformation [mm]
Graphite	$2.9 \times 10^7$	$2.87 \times 10^7$	$1.26 \times 10^7$	$4.12 \times 10^6$	0.7
Metal	$3.85 \times 10^7$	$2.71 \times 10^7$	$3.72 \times 10^7$	$3.84 \times 10^7$	1.09

The main physical, thermal and mechanical properties of the POCO graphite TM-1 (50 kW) and AXF-5Q (200 kW) are shown in Table 2.3

Both kinds of graphite are purified POCO grade and have less than 5ppm total impurities. The only elements present in trace are: Si, S, V, Ca, B, Al, Mg, Fe, Mo, P.

To compensate the thermal dilatation of the graphite the converter is divided into sectors (12 and 36 sectors for the 50 kW and the 200 kW converters, respectively). The gap between the sectors is 1.5mm produced by laser cut with an angle of  $45^{\circ}$ . This latter has been chosen in order to avoid beam leakage through the converter gaps during the operations.

**Table 2.2. Geometrical and thermo-mechanical parameters for the 200 kW neutron converter.**

Max. converter temp. [ $^{\circ}$ C]	Target diameter [cm]	Max. metal temp. [ $^{\circ}$ C]	Max. t-m stress in graphite [Pa]	Max. t-m stress in metal [Pa]	Max. inertial stress (10 Hz) [Pa]
1790	120	570	$3.3 \times 10^7$	$2 \times 10^8$	$5 \times 10^7$

Material	Max. t/m stress von Mises [Pa]	Max. t/m stress X-component [Pa]	Max. t/m stress Y-component [Pa]	Max. t/m stress Z-component [Pa]	Max. deformation [mm]
Graphite	$3.16 \times 10^7$	$3.25 \times 10^7$	$2.03 \times 10^7$	$2.85 \times 10^6$	0.75
Metal	$3.8 \times 10^8$	$10^8$	$1.3 \times 10^8$	$1.45 \times 10^8$	1.7

**Table 2.3. Main physical, thermal and mechanical properties of the POCO graphite.**

Properties	TM-1	AXF-5Q	Unit
Density	1,82	1,78	g/cc
Porosity	20	20	%
Particle Size	10	5	$\mu$ m
Ultimate Tensile Strength	40	60	MPa
Modulus of Elasticity	10	11	GPa
Flexural Strength	60	99	MPa
Compressive Yield Strength	110	145	MPa
Electrical Resistivity	0,0012	0,00147	ohm-cm
CTE, linear	8,20	7,90	$\mu$ m/m- $^{\circ}$ C
Thermal Conductivity	105	95	W/m-K

The 50 kW converter is obtained by laser cut directly from a TM-1 graphite plate of  $600 \times 600 \times 8 \text{ mm}^3$ . The active part of the graphite's plate has a radial length of 80mm. The spokes are made of Stainless Steel 316LN with tubular shape ( $\phi_{\text{ext}} = 7 \text{ mm}$ ;  $\phi_{\text{int}} = 4 \text{ mm}$ ) and provide the mechanical coupling between the graphite sectors and the rotating shaft. The mechanical contacts have one degree of freedom, so the spokes may have a minimum angular displacement to absorb the thermal dilatation of the graphite, minimizing the heat transfer from the graphite to the shaft.

The 200 kW converter is obtained by laser cut from AXF-5Q1 graphite plates of  $600 \times 300 \times 8 \text{ mm}^3$ . The active part of the sectors has a radial length of 100 mm. To minimize the heat transfer from the graphite to the shaft, a combination of a metal frame and spokes is used. Mechanically, the sectors, the metal frame and the spokes are connected to each other by graphite's rings specially shaped. To absorb the thermal dilatation of graphite, the sectors are weakly clamped to the metal frame so they can move azimuthally. The mechanical frame and the spokes are in INCONEL 600.

The converter lifetime has been estimated on the base of laboratory tests on graphite sample to be around 10000 hours [10].

The converter wheel is driven by an electrical asynchronous motor, under vacuum, inside the production module and is clamped to the mechanical frame of the NCM. The movement is transmitted to the converter through a transmission's shaft which length will vary on function of the converter's diameter. Both shafts are in AISI 440C Stainless Steel . The two shafts are orthogonally to each other and coupled by a 45° helical gear. The helical gear is treated on the surface by implanting boron nitrite to increase the hardeners and provide the lubrication required to operate in vacuum.

The rotation system is equipped with two different kind of ball bearings specially developed to operate in vacuum, without lubricant and at high temperature (up to 300 °C) and tested for this application [4]; ADR-W6002-RT4K4296 for the electrical motor and the transmission's shaft, and ADR-WSP15312-RT4K4297 for the shaft of the converter. Being the bearings subject to wear and tear, the rotation system is conceived to allow a quick replacement of the bearings without disassembling the whole NCM (Figure 2.10). The replacement of the bearings is foreseen at the end of every operation period of three months.

The converter rotation system is controlled by monitoring three main parameters, each one independent to the others: voltage, current absorbed and shafts rotation (by inductive pickups located one on the motor shaft and the other on the converter shaft). In addition, a pair of thermocouples are monitoring the motor driver and the converter shaft temperatures

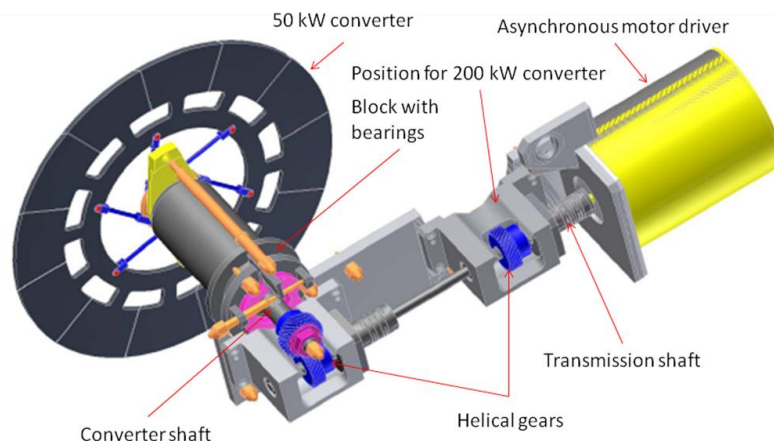


**Figure 2.10. Rotation system for the 50 kW converter. For the 200 kW converter the rotation systems demand a shorter shaft. The system has been conceived to replace the block with bearings keeping the converter in place.**

### 2.3.2. Cooling System

The power dissipation from the converter does not demand a sophisticated cooling system; the heat is exchanged by radiation with the water cooled panels. Heat removal from the production

module volume is carried out by water circulating inside cooling panels, fixed to the module's walls by the mechanical adaptation ring.

The cooling panels consist essentially of a set of two Stainless Steel 316 LN plates with circular geometry which have the cooling channels excavated inside. The set of panels is defined as the front panel and the rear panel, respect the incoming direction of the deuteron beam. The rear panel is covering also the lateral side of the converter. The panel surfaces are blackened with a chemical process to enhance their cooling efficiency (thermal absorption coefficient = 0.95).

The cooling panels are clamped to the mechanical adaptation ring by 12 hexagonal-headed bolts and fit the frontal edge of the production module. The head of the bolts has been designed to be easily managed by a telemanipulators inside the hot cell. The cooling water channels are excavated in the plates, they have 10 mm thickness and consist of several concentric rings with a cross-section of  $15 \times 6 \text{ mm}^2$ . The panels are terminated by cover plates of 4mm thickness laser welded by along the perimeter and spot welded along the channels. For minimizing the distance between the converter and the UCx target, the delay window is conceived as an integral part of the rear panel.

To house the Delay Window, the panel is excavated and a thin tantalum plate of 2mm is applied by laser welding to assure the physical separation between the converter and the target volumes. The tantalum dilatation due to the high temperature induced by the UCx oven (up to  $1300 \text{ }^\circ\text{C}$ ) is compensated by a special mechanical solution adopted in the welding region. In the region covered by the delay window the liquid lead has also the function of coolant. The maximum power deposited in the liquid lead is about 15 kW (200 kW beam) which will be released in the heat exchanger.

The water circuit consists of 5 input/output independent tubes ( $\frac{3}{4}$ " diameter), integrated with the cooling panels (laser welding) providing more mechanical rigidity of these latter. Three tubes are connected to the rear panel and two tubes to the front one. The connections to the panels are assured by AISI 316L Stainless Steel flexible tubes. In one side the tubes are welded on the servitude flanges, while in the other side are attached to the cooling panels by the cone/sphere connectors, specially modified for being telemanipulated. The use of the connectors is imposed by the necessity of the panels to be assembled and disassembled. A sketch of the working principle of the special connectors for water cooling is shown in Figure 2.11 and Figure 2.12.

---

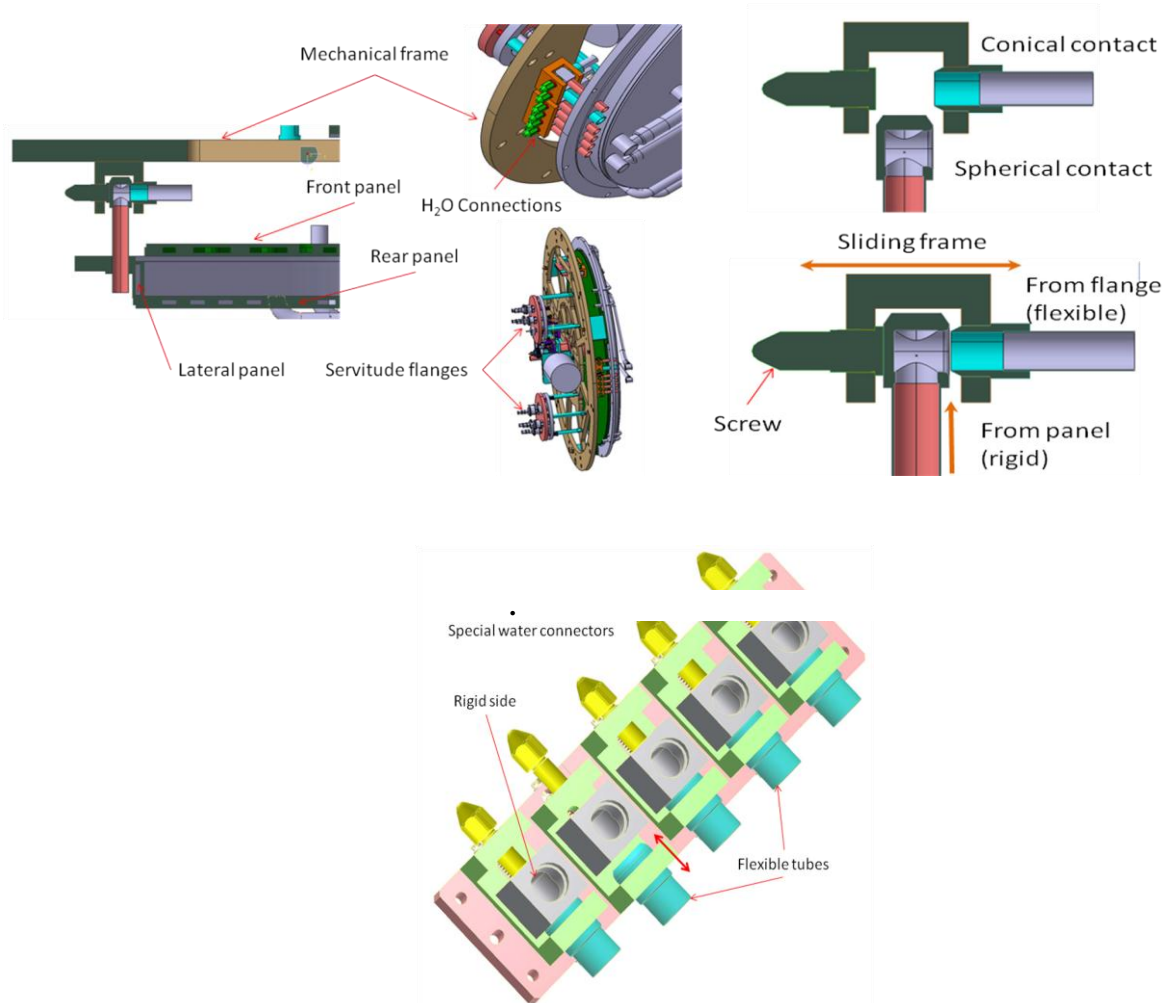


**Figure 2.11.** A sketch of the working principle of the special connectors for water cooling and liquid lead system

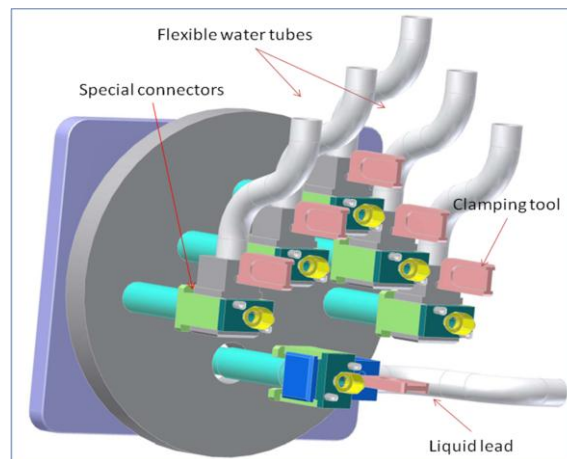


**Figure 2.12.** Connecting solution for the water cooling system and delay window on the servitude flange.

A sliding mechanical frame made of Stainless Steel keeps fixed the flexible tube, the ending part is a conical connector and it is screw-fixed, designed as well to be telemanipulated, The same kind of connectors are also used for the liquid lead system of the delay window.

For a fast and easy connection/disconnection the same kind of connectors are installed also on the servitudes flanges, outside of the production module.

To guarantee the correct working of the cooling system, the water flow, pressure and in/out temperatures are permanently measured. A set of height thermocouples gives the temperatures of different regions of the cooling panels.

### 2.3.3. The Delay Window

The “delay window” is designed to protect the UCx target; in case of failure of the neutron converter the deuteron beam interact directly with the Delay Window which will *delay* the eventual interaction of the deuteron beam with the UCx Target. This *delaying time* has to be long enough to allow the interlock to react and safely stop the beam operation. The Delay Window is made of INCONEL 600 with blackened surfaces to enhance their cooling efficiency because the liquid lead is replacing the water as coolant in the region where there are no cooling channels.

The position of the Delay Window is shown in Figure 2.13. It presents an L’s shape with an active length of about 200 mm. A lead thickness of 1.8 mm is enough to stop the 40 MeV deuteron beam; for safety reasons the active part of the Delay Window has been chosen to be 5 mm thick and 60mm wide. The front wall of the Delay Window is 2mm thick and is melt in 5ms by the 200 kW deuteron beam. The rear wall is 7mm thick, including the lead heating system too. The main parameters characterizing the Delay Window are listed in Table 2.4 and Table 2.5

The Delay Window is clamped on its central part to the rear cooling panel and is free to expand by heat along the longitudinal direction. In fact, because of its working temperature the Delay Window will expand about 0,8 mm each side. Special feedthrough have been designed for the liquid lead tubes that cross the cooling panel; the holes have an elliptical shape and are bigger than the feedthroughs itself.

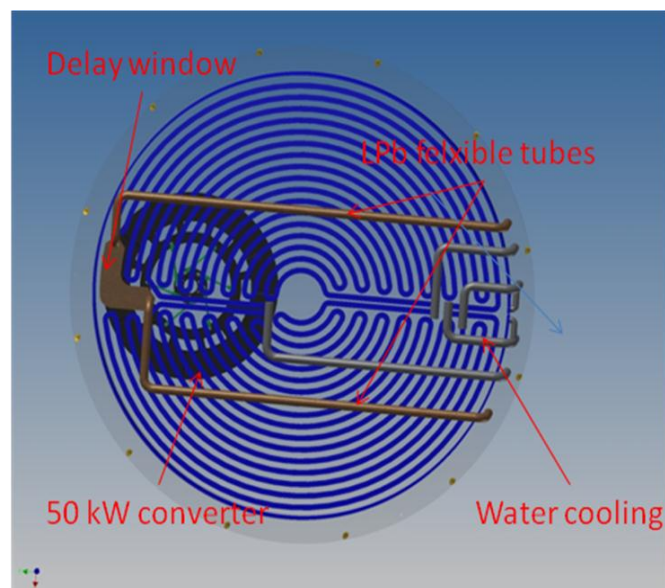


**Figure 2.13** The delay window set up for the 50 kW converter. The Delay Window is integrated in the rear cooling panel and the liquid lead play also the role of coolant.

**Table 2.4.** Main parameters of the delay window.

Parameter	Value	Measure unit
Thickness of liquid lead jet (70 MeV deuteron)	5	mm
Width of the delay window	60	mm
Thickness of the wall (Stainless Steel )	2	mm
Velocity of the liquid lead alloy	1,5	m/s
Temperature of liquid lead alloy	< 350	°C
Time of melting first wall	< 10	ms
Evacuation rate of liquid lead in case of failure (200 kW)	~ 0,5	l/s
Active protection time in case of failure (200 kW)	~ 60	s

**Table 2.5.** Main thermal parameters of the delay window.

Lead parameters	Mesure unit	Converter	
		50 kW	200 kW
Lead temperature inlet	°C	350	350
Maximum lead temperature	°C	363	368
Pressure drop over the lead	Pa	1,06 e+05	1,06 e+05
Lead consumption channel	l/s	0,067	0,067
Lead velocity at the inlet, average value	m/s	1,5	1,5
Lead velocity at the outlet, average value	m/s	1,47	1,47

The sealing is guaranteed by graphite gaskets which allow the feedthroughs to slide on the surface of the cooling panel to compensate the heat expansion. The liquid lead is flowing inside two AISI 316L Stainless Steel flexible tubes from *RAFIX Company* and the heat expansion (about 6mm) is compensated by their flexibility. In general, all the connections of the liquid lead circuit are made by laser welding.

A Stainless Steel tank ( $\phi$ . 350mm, 500 mm high) contains 30 liters of liquid lead (340 kg) and the pump for its circulation. The pump is driven by an electrical asynchronous motor analogous to that used for driving the converter wheel. The liquid lead tank is mechanically connected to the production module, together with the heat exchanger, which is made of AISI 316L Stainless Steel box (350x500x150mm<sup>3</sup>).

The liquid lead flows from the tank to the delay window and then passes through the heat exchanger for removing heat by means of an external and independent nitrogen/water-cooling circuit. The connections from the tank/heat exchanger and the Delay Window are provided by flexible AISI 316L Stainless Steel tubes connected to the servitude flanges by the cone/sphere connectors (RAFIX) modified for operating with telemanipulators.

The Delay Window has to operate at constant temperature  $> 320$  °C (the melting temperature of the Pb-Sn alloy is 293 °C)

Before removing the production module to the maintenance area, the liquid lead has to be leaded from the Delay Window to the tank. This operation is possible thanks to a hot gas flux (Nitrogen) at a temperature of 350 °C. The pressure of the gas is below 5 bar. The gas heating is provided by 9 kW circulation heater (type FCONA25J5) from Watlow company. Two high temperature ball valves from Flowserve McCanna Company (<http://www.flowserve.com>) are regulating the gas flow.

The same kind of gas heating system of higher power (30 kW) can be used to heat the liquid lead as an alternative to the electrical heaters described previously. The main advantages relies on the absence of electrical components in a high radioactive environment, absence of electrical feedthrough and an easier control system.

The liquid lead consists in a 90%Pb (99,985% purity) and 10% Sn (99,9915% purity) alloy. The impurities contained in the PbSn alloy (percentage) are listed in Table 2.6.

**Table 2.6. Composition of the PbSn alloy.**

Pb	99,985	Sn	99,9915
Bi	6E-3	Bi	1E-3
Fe	1E-3	Fe	1E-3
Cu	1E-3	Cu	1E-3
As	1E-3	As	1E-3
Sn	1E-3	Pb	1E-3
Ag	1E-1	Sb	1E-3
Sb	1E-1	Zn	1E-3
Zn	1E-3	Al	1E-3

		Au	1E-4
		Co	1E-4
		Ni	1E-4
		Ag	1E-4
		In	1E-4

Both, transport and heat exchange parameters, namely, the fluid velocity, the pressure drop over the channel, the temperature distribution along the channel and over the whole device, are calculated.

#### 2.3.4. Beam Collimator

To protect the neutron converter from beam instabilities and define the right shape of the beam a collimator is installed in front to the converter (Figure 2.14).

The collimator consists in 4 sectors, electrically insulated from each other, mechanically mounted on the door of the production module. The collimator itself is made of molybdenum and the sectors are water cooled through tubular conductors connected externally by electrical feedthroughs. The internal diameter of the collimator is 17,4mm and 39,6mm, for the 50 kW and 200 kW respectively.

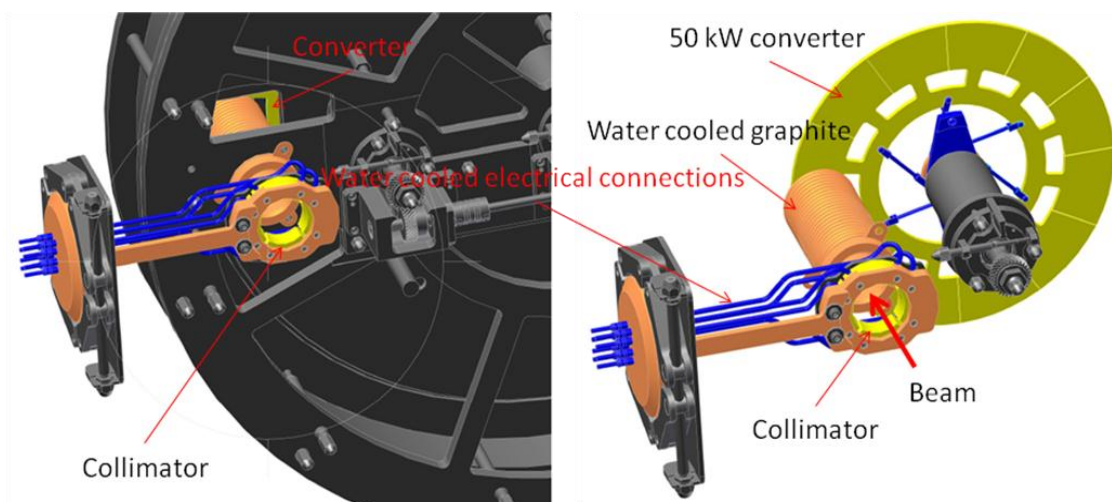


**Figure 2.14. The production module with installed the beam collimator (left) and the set up for the 50 kW converter including the water cooled graphite tube (right) .**

The diameter of the collimator is a little smaller than the beam size (at  $6\sigma$ ) in order to allow a small part of the beam tails are always intercepted by those sectors. The measurement of the current on the sectors gives the beam position and allows the continuous monitoring of the beam.

After the collimator, a water cooled graphite tube is limiting transversally the beam path and is collecting the back scattered electrons from the converter surface. This graphite tube is

positioned as close as possible to the converter for shielding the production module from the heat radiation. The graphite tube is an integral part of the NPM and is installed on the mechanical frame.

### *2.3.5. Electrical Structure*

The electrical equipment associated to the neutron converter is essentially consisting on the power supply for the two asynchronous motors, the heating system for the liquid lead and the evacuation system for the liquid lead.

The driving motor for the neutron converter absorbs about 1kW and is controlled by an Altivar 312 variable speed driver from Schneider Electric ([www.schneider-electric.com](http://www.schneider-electric.com)).

The driving motor for the liquid lead system absorbs 5kW and is also controlled by an Altivar 312 variable speed driver. The liquid lead heating system, consisting of heaters produced by Watlow company, absorbs totally about 30kW. The control system consists of 8 thermocouples connected to 8 thermo regulators. The gas heater has to provide 100 l/m gas flow at 350 °C and is absorbing 9 kW power; in addition, it requires a gas compressor that can be installed outside of the red-zone.

Both, the Altivar 312 variable speed drivers and the 8 thermo regulators are installed outside of the red-zone, as well as all the control system.

In case of liquid lead heating by hot gas, a dedicated circulator heater of 50 kW power is required, associated to an adequate gas compressor and related control system

### *2.3.6. Protection and Prevention*

The neutron converter, as well as the Uranium Carbide target and the ion source, is placed inside a module, i.e. the production module which is surrounded by the biological shielding. In practice, the production module is a shielded box that contains all the sub-system required for production of radioactive ions and that became highly radioactive and contaminated. Removal of the production module has to be done only by remote handling device. The disassembling of the production module, spare parts replacement, or conditioning of elements have to be carried out inside the hot-cell to ensure that the radioactivity is confined.

To be remotely manipulated the converter design has been conceived as a “sub-module” which can be handled independently from the production module. This “sub-module” (NCM) integrates the converter it-self, the rotation system, the cooling panels, the delay window and all the servitudes required to operate the converter. The NCM has been conceived to house both the 50 kW and 200 kW converter, depending of the requests, just by replacing the converter (wheel)

---

of the corresponding dimensions. The cooling panels, the delay window, the driving motors and the servitudes remain unchanged and may be re-used several times.

### *2.3.7. Maintenance and Waste Management*

The continuous working period of the SPIRAL-2 Facility is up to 90 days; at the end of this period some maintenance is required. Both, the ball bearings sets for the driving motor/transmission shaft (type ADR W6002-RT4K4296) and the converter (type ADR WSP15312-RT4K4297) have to be mandatory replaced. This operation can be done without disassembling the NCM from the production module. The driving block is removed and there are full access to the converter bearings block. Is mandatory to consider:

- The visual inspection of the converter, of the water cooling/liquid lead connectors, of the delay window and of the electrical components is suggested at the end of each working period, at least during the first year of operation. This action requires a full disassembling of the NCM.
- The neutron converter has about 10000 hours lifetime, that means more than 4 times the working periods, after which the wheel has to be replaced.
- The motors drivers are submitted to an integral dose of about  $10^6$  Gy every working period and they have to be replaced every year.
- The graphite gaskets have to be replaced at every disassembling of the NCM.
- The cooling panels, delay window and other mechanical components are submitted to a relatively low radiation rate and the accumulated damage is in the order of 1 dpa per 10000 hours of operation. The replacement may be planned after reaching the 5 dpa of damage.

## *2.4. Additional Specifications*

### *2.4.1. Driver And Primary Beams*

- The driver must deliver deuterons up to an energy of 40 MeV with a beam current up to 5 mA and heavy ions with beam currents up to 1 mA.
  - For each beam profile one temperature distribution over the target is generated and the target diameter is matched so as to keep the converter temperature within the range of 1850 and 2000°C
  - The beam energy will be adjustable between the maximal energy and as low as the RFQ output energy. The layout of the facility takes into account the possible future increase in energy up to 100 MeV/u.
-

- A fast chopper is required for some physics experiments to select one bunch out of a few hundred to a few thousand.

#### 2.4.2. *Production Hall*

- The production rate of the radioactive beams produced by neutron-induced fission of an uranium target from a deuteron beam bombarding a carbon converter, must be higher than  $10^{13}$  fissions/s. The use of high-density targets could allow us to reach an upper limit of  $2 \cdot 10^{14}$  fissions/s. However, the fission rate is limited to a maximum of  $10^{14}$  fissions/s and this value has been used for all safety and radiation-protection-related calculations.
- The converter has to withstand a maximum beam power of 200 kW.
- Without the use of a converter, the primary beam will consist of deuterons or other species (such as  ${}^3_2\text{He}$ ,  ${}^{12,13}_6\text{C}$ ) and the maximum power is limited by the most restricting condition, namely that the induced activity must remain below the activity induced by  $10^{14}$  fissions/s obtained with the converter method and the maximum power that the target can withstand (presently estimated to about 6 kW for a  $\text{UC}_x$  target).
- Different thick targets will replace the uranium target for fusion evaporation reactions with stable ion beams.
- Different types of ion sources will be studied in order to get the best efficiency for the selected ion specie.
- A mass separator must deliver simultaneously at least two independent beams, with a mass resolution of about 250.
- An identification station is essential for the control of the desired specie output.
- The isotopes will be bred to higher charge states by means of an ECR charge breeder prior to post-acceleration.

#### 2.4.3. *Experimental Area*

- Without post-acceleration, the secondary beams will be transported to the low-energy experimental hall (LIRAT).
  - After post-acceleration in the existing CIME cyclotron, the secondary beams will be transported to the existing experimental area at GANIL.
  - New direct beam transfer lines will allow the direct delivery of beams out of CIME to the existing caves G1/G2.
  - For the study of fusion evaporation reactions with the in-flight method, the high-intensity stable ion beams from the linac will be transported to a new experimental hall.
-

### *Use of Neutrons For Other Applications*

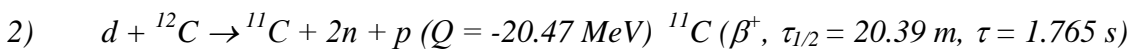
- The possibility of material irradiation studies, using a large neutron flux, especially for the study of the behaviour of materials considered for future fusion machines (ITER, DEMO), has to be investigated.
  - Room must be left for possible installation of a pulsed neutron beam facility, including an experimental hall and a ~10 m long neutron line to be used for neutron-TOF like experiments.
-

## CHAPTER 3. FUNDAMENTAL CONCEPTS: MATERIAL ACTIVATION

Calculation concerning the activation of the NCM materials have been performed by MCNP and PRIZMA codes: Activation Cross Section Library ACTL (LLLDOS) for MCNP, EXFOR experimental data library and NEA Data Bank have been used [25]. The main source of radiation are represented by the activation of the graphite and liquid lead of the delay window. Calculations are performed for the 200 kW beam power and 10.000 hours of operations.

### 3.1. Converter Activation

The activation of the graphite is mainly induced by the deuteron beam (the neutron activation is negligible). The activation is generated by the production of  $^{11}\text{C}$  and  $^{13}\text{C}$  nuclei. Two main reactions are considered:



The yield of gamma's from the graphite converter has been estimated. An accurate estimation is not possible due to insufficient data on the interaction of deuterons with carbon nuclei. Nevertheless, the analysis showed that the influence of the gamma's coming directly from the converter could be neglected. The main source of gamma's is due to the annihilation of the positrons ( $\beta$  decay of  $^{13}\text{N}$  and  $^{11}\text{C}$ ) and to the neutron capture in the materials surrounding the converter.

At the equilibrium the production of the most active isotopes is:

$$N({}^{13}\text{N}) = 6.7 \cdot 10^{16} \text{ nuclides,}$$

$$N({}^{11}\text{C}) = 4.4 \cdot 10^{15} \text{ nuclides.}$$

The contribution of  $^{14}\text{C}$  was not considered.

After irradiation, the cooling time is relatively short. The total activity at the converter level decrease of 5 order of magnitude (from  $10^3$  to  $10^{-2}$  Ci) in about 300 minutes (see Figure 3.1).

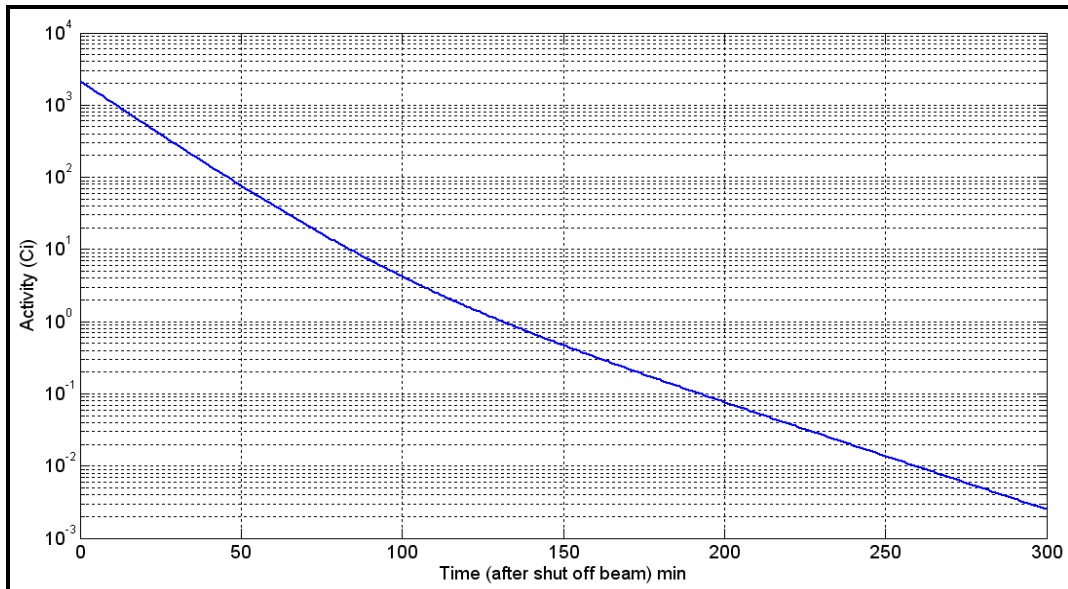


**Figure 3.1. - Decay time of the activity at the converter level.**

The decay of the isotopes results in two gammas of energy 511 keV produced by the annihilation of the positron. Because the production of  $^{11}\text{C}$  and  $^{13}\text{N}$  have different spatial distributions (distribution across the target depth) the spatial distribution of gamma-source is a function of time, i.e. at the beginning it corresponds to the spatial distribution of  $^{13}\text{N}$ , but in approximately 2 hours it will correspond to the distribution of  $^{11}\text{C}$ . Therefore as the time is progressing the intensity of the gamma-source decreases but the relative intensity in the layers which are closer to the irradiated surface increases.

### **3.2. Delay Window Activation**

An important source of radiation is represented by the activation of the liquid lead circulating inside the delay window. The delay window is located just behind of the neutron converter, on the beam axis, and the liquid lead is continuously irradiated by the neutrons flux. The amount of liquid lead circulating in the delay window is about 30 liters, corresponding to about 340 kg. The composition of the liquid lead alloy (90% Pb and 10% Sn) is shown in Chapter 2

The calculations were performed taking into account the liquid lead alloy composition (impurities included) and  $10^4$  hours (about 400 days) of operation. The equilibrium is reached at around 10 Ci of activity. A cooling period of about 2.000 days reduces the radioactivity of about 3 order of magnitude (see Figure 3.2).

The long-lived isotopes are the main responsible of the long time activation of the liquid lead alloy. The most important long-lived radionuclide are  $^{119}\text{Sn}^m$ ,  $^{123}\text{Sn}$ ,  $^{121}\text{Sn}^m$  and  $^{125}\text{Sb}$ , as shown in Figure 3.3

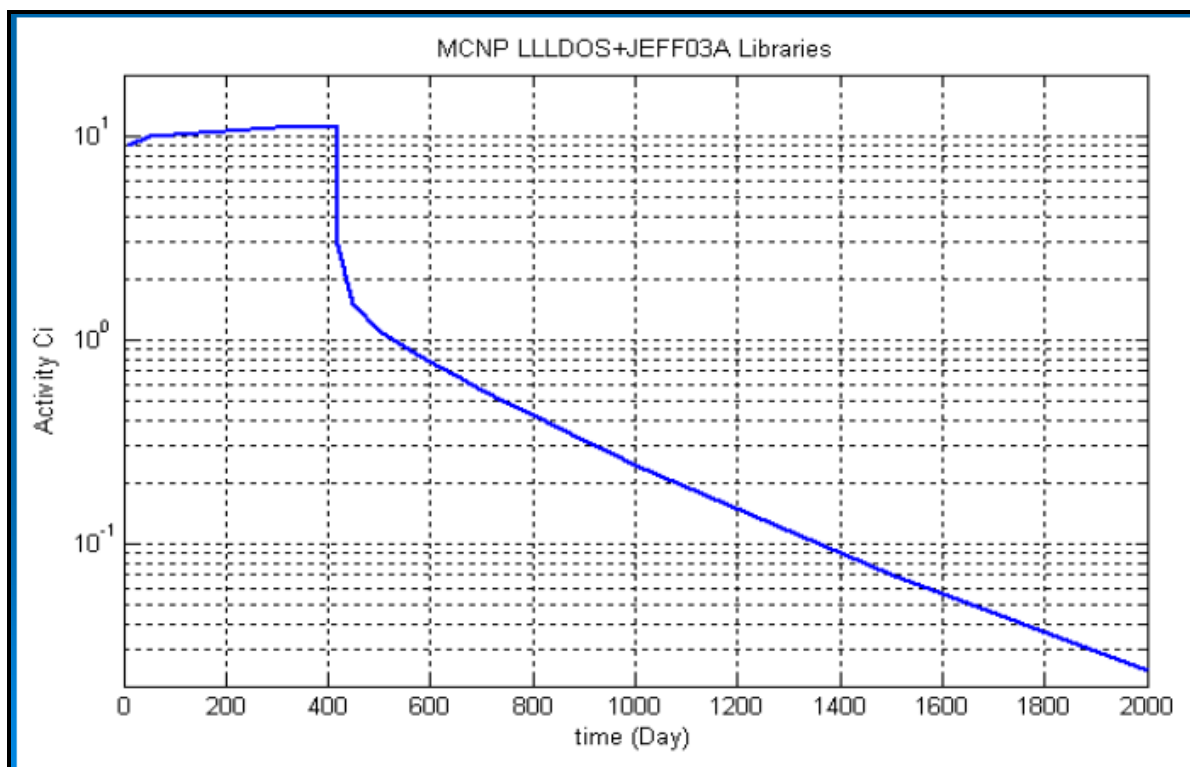


Figure 3.2. - Total activity evolution of the radionuclide produced in the liquid lead alloy of the delay window

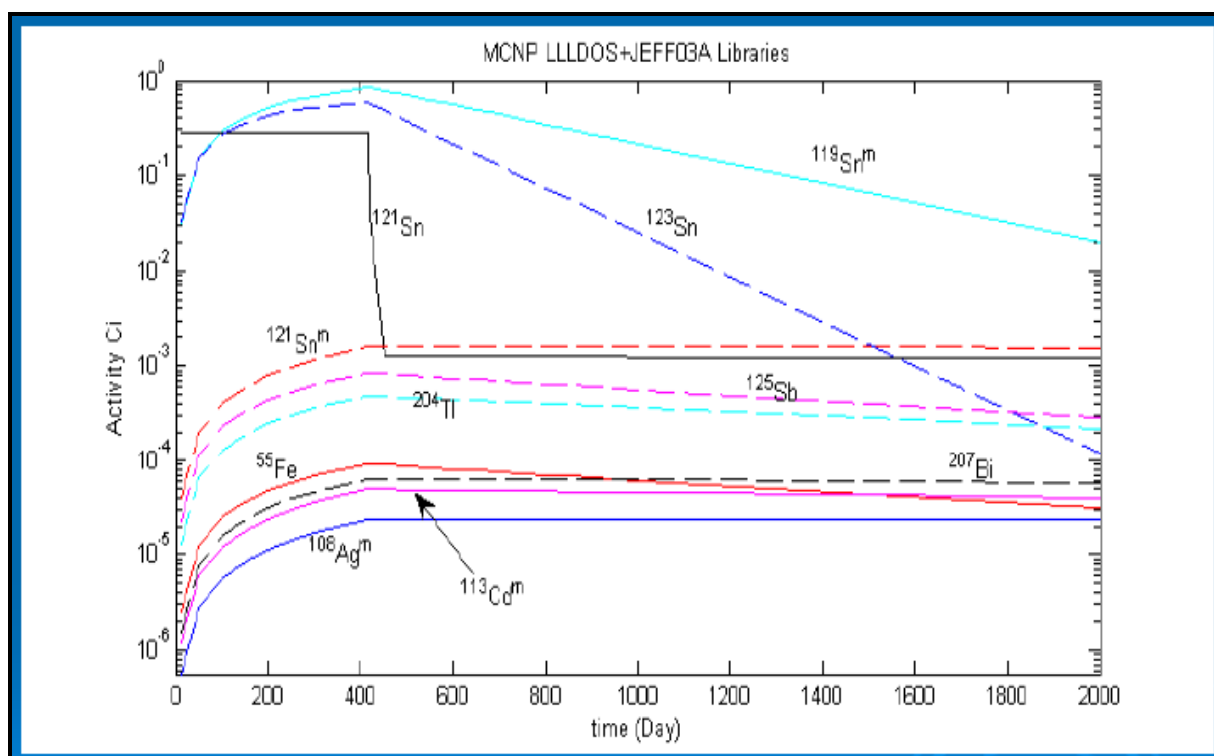


Figure 3.3.- Activity evolution of long-lived radionuclide produced in the liquid lead alloy.

The maximum production of each of them is:

$^{119}\text{Sn}^m$ (maximum)	$\sim 1 \text{ Ci}$
$^{123}\text{Sn}$ (maximum)	$\sim 0,5 \text{ Ci}$
$^{121}\text{Sn}^m$ (maximum)	$\sim 3 \times 10^{-3} \text{ Ci}$
$^{121}\text{Sn}$ (result of decay $^{121}\text{Sn}^m$ )	$\sim 10^{-3} \text{ Ci}$

Such radionuclide are not considered particularly hazardous for health. After exploitation the lead can be decontaminated and subsequently re-used in the same installation.

### 3.3. *Radiation Damage*

At present there are no reliable experimental methods to determine the number of atomic displacements caused by a radiation. All existing methods are based on the indirect measurement of particular material characteristics [17]. On the other hand, the number of displaced atoms is generally assumed to be one of the basic characteristics defining the effect of radiations on material properties (strength, thermal expansion ratio, conductors resistance, etc). This brings up the necessity of evaluating by numerical techniques the number of displacements or some quantities which define it, for example, the defect generation rate, or the rate of annealing.

In the SPIRAL-2 case, the radiation load will be mainly applied to the carbon target designed for the high-energy neutrons generation. Many defects generated in the target come from the atomic cascades initiated by deuterons with initial energy of 40 MeV. The effect of neutrons on defect generation will be insignificant because the coefficient of the  $D \rightarrow n$  transformation is  $\sim 4\%$ , and the probability that a secondary neutron undergoes a reaction and transfers sufficient energy to C nuclei in the target is very small, while deuterium in moderating and cascading causes  $\sim 200$  atomic displacements. Also thermalized deuterons will generate regions in the carbon target with higher concentrations of D and  $D_2$  (possibly methane and other C-H(D) structures) [18,19].

The published Monte Carlo techniques MARLOW [20, 21] and TRIM-91 [22], as well as ATOCAS and TRCR2 [23] developed at RFNC-VNIITF, predict defect generation from particles of relatively low energies where it is not very important to consider energy fluctuations in the ionization moderation of initiating particles. In the case of 40 MeV deuterons on the graphite converter the correct evaluations [24] suggest that the contribution of the energy loss fluctuations may change the peak of pda density by a factor of 100. This is why it has been decided that the fluctuations of ionization and excitation losses need to be taken into account in problems where ionization loss is important and the pda density gradients need to be described exactly.

---

### 3.3.1. Effect of Irradiation on Thermal and Mechanical Properties of Graphite

The effect of changing the properties (in particular, thermal conductivity) of graphite being continuously exposed to the primary beam of protons/deuterons is observed by a number of researchers [3, 4] and is related to the radiation damage of matter. Study of this effect is very important since it determines the lifetime of a neutron production target and may bring some corrections to its operation modes. In this section we will show how the temperature and stress distribution change in time for unirradiated and irradiated converter made of graphite.

The model geometry comprises the graphite ring with 22 cm internal radius, 26 cm external radius and 7 mm thickness. The 40 MeV 50 kW deuteron beam has the width 1 cm ( $4\sigma$  level). Thermo-cycle consists of 400 s heating up from room temperature and subsequent 800 s cooling down by radiation. Temperature field and stress distribution have been calculated at time 0.5 s, 2 s, 5 s, 10 s, 50 s, 100 s, 200 s, 400 s, 700 s, 1000 s, 1200 s. The transient analysis has been performed for 2 different representations of thermal conductivity curves given by Tanabe [5] and VNIITF team (V.V. Plokhov et. al., [6]).

Tanabe gives [5] the thermal conductivity curves vs. temperature for a number of graphite materials (Figure 3.4-, left). It has been considered the unirradiated graphite as well as the one irradiated up to 0.02 dpa and 0.25 dpa. Table 3.1 and Figure 3.4-right, show the result of a steady state thermal analysis. This figure shows the temperature and stress field at different time.

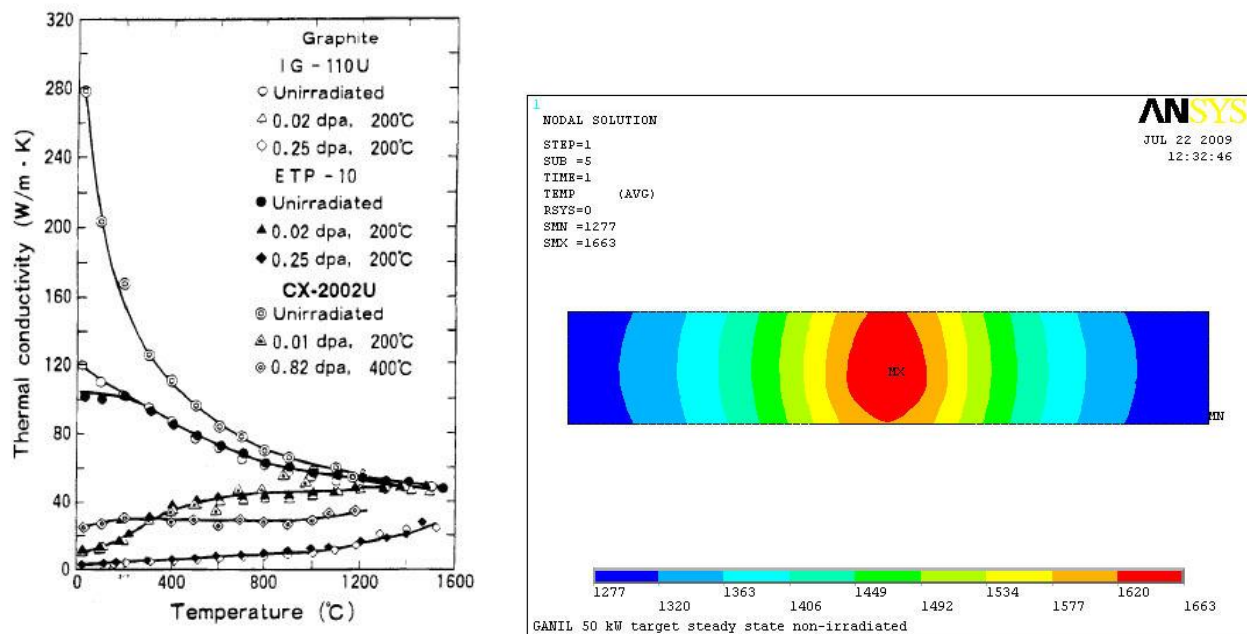
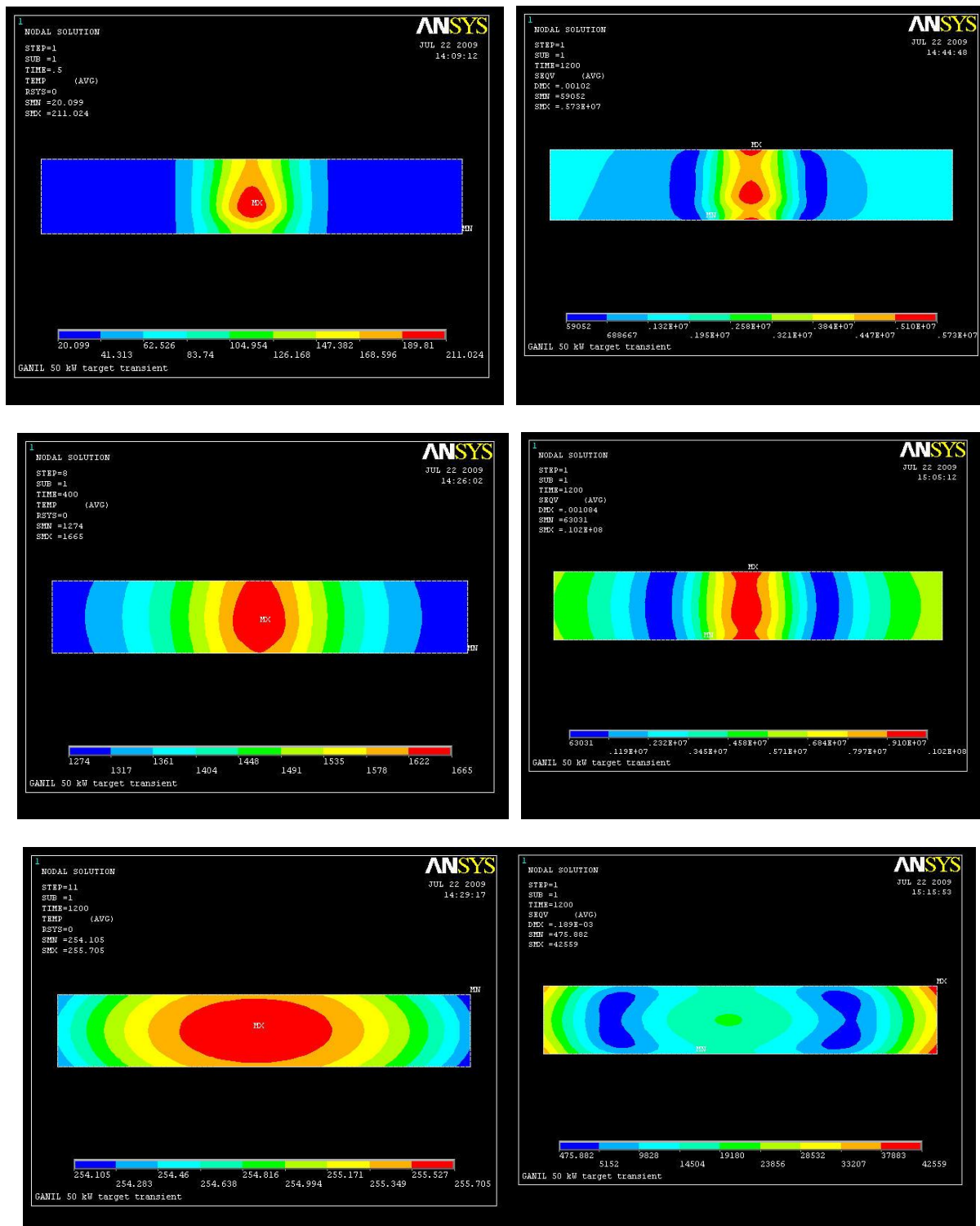


Figure 3.4: Left- thermal conductivity vs. temperature for different graphite materials (data of Tanabe), right – steady-state temperature field over unirradiated converter made of ETP-10 graphite.

**Table 3.1. Maximum converter temperatures for irradiated and unirradiated ETP-10 graphite converter. Data of Tanabe, steady-state analysis.**

	unirradiated	irrad. 0.02 dpa	irrad. 0.25 dpa
Max. converter temp., °C	1663	1666	1777



**Figure 3.5. Transient analysis of ETP-10 graphite irradiated to 0.02 dpa. Left column– temperature (°C), right column – stress distribution (Pa). Data taken at 0.5 s (top row), 400 s (middle row), and 1200 s (bottom row)**

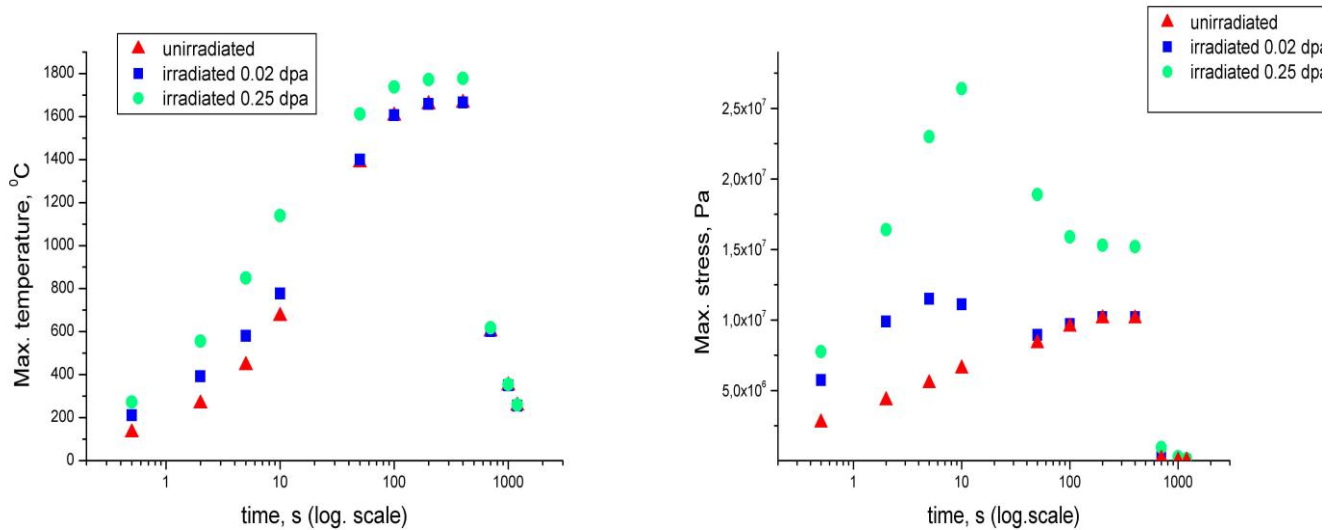


**Figure 3.6: Left – maximum converter temperature vs. time, right – maximum thermo-mechanical stress vs. time for irradiated and unirradiated ETP-10 graphite.**

Figure 3.6 summarizes the data on temperature and stress for irradiated and unirradiated graphite taken at different time during the thermo-cycle. As it is seen, the biggest difference in temperature and thermo-mechanical stress between the irradiated and unirradiated converter is observed at the heating-up initial stage where the temperature is rather low. This is caused by the big difference in thermal conductivity behavior within the low temperature region. Irradiation does not affect much at converter's operational temperature around 1650 - 1750 °C, which is referred to the annealing of radiation defects at high temperature. Cooling process is not accompanied by the essential thermo-mechanical stress.

Data for next analysis is taken from VNIITF report [6] (Federal State Unitary Institution Russian Federal Nuclear Center Zababakhin Russian Research Institution of Technical Physics – Snezhink – Russian Federation) (see Figure 3.7) Thermal conductivity dependence on temperature for unirradiated MPG-6 graphite is obtained by means of extrapolating the data so that to make the curve similar to the existing (standard) dependence used at the majority of calculations. Then, according to Figure 3.7-left, the unirradiated data have been divided by a factor of 3.5 in order to obtain the curve for irradiated graphite at fluence  $4 \cdot 10^{21}$  n/cm<sup>2</sup> (Figure 3.7, right).

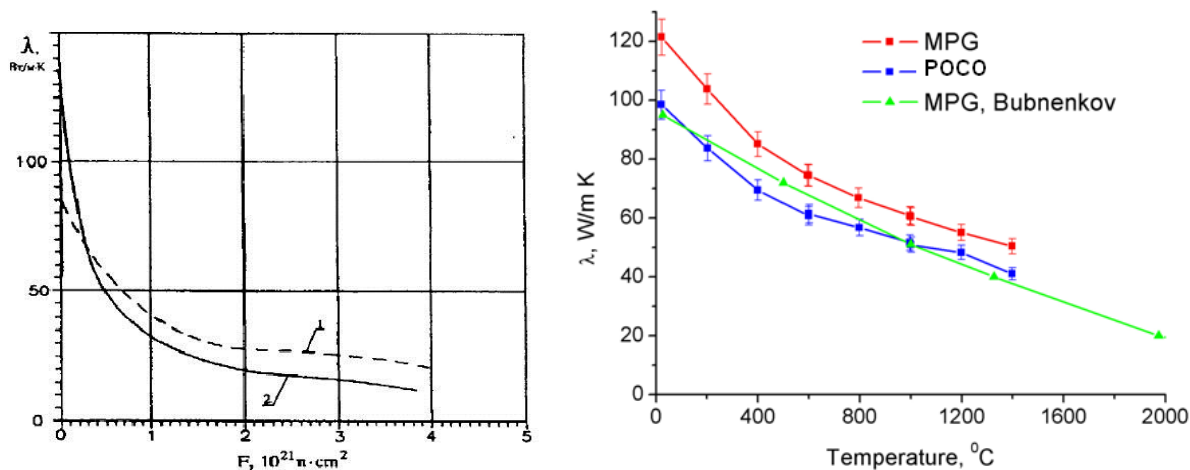
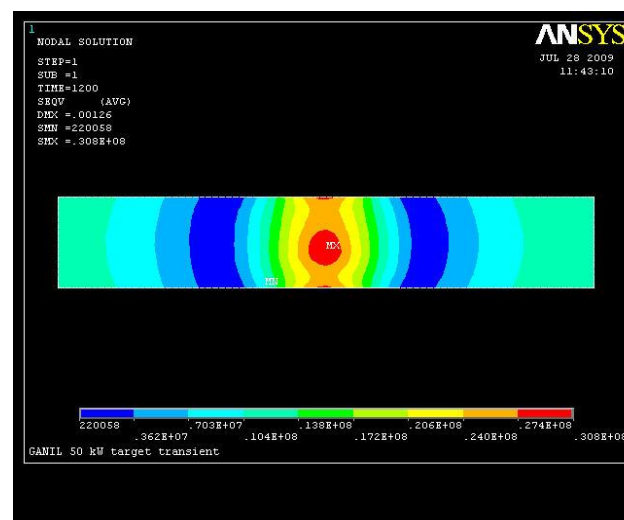
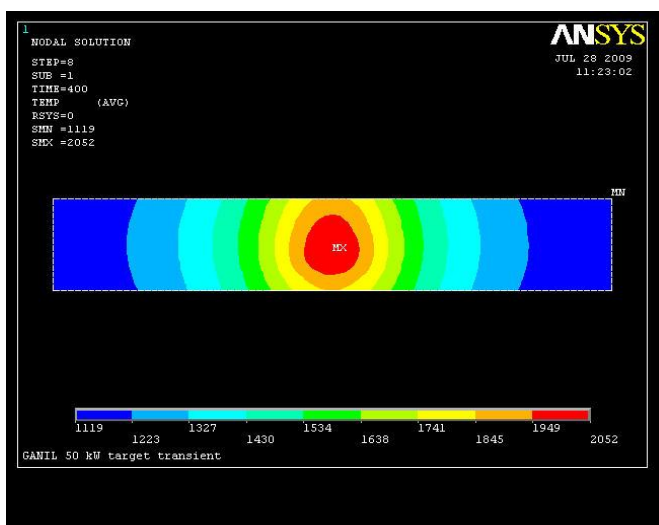
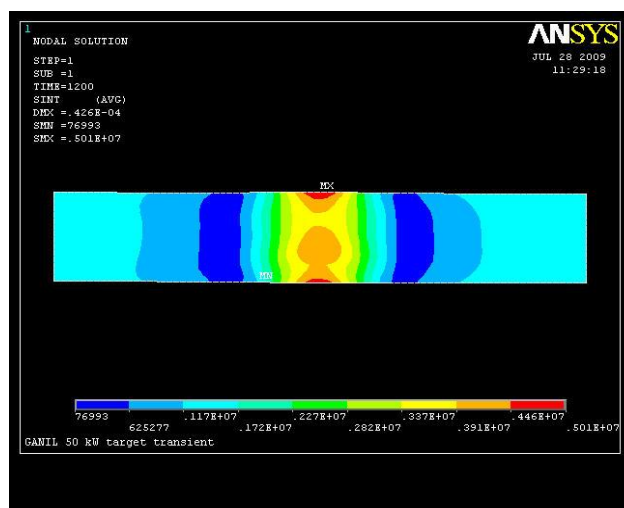
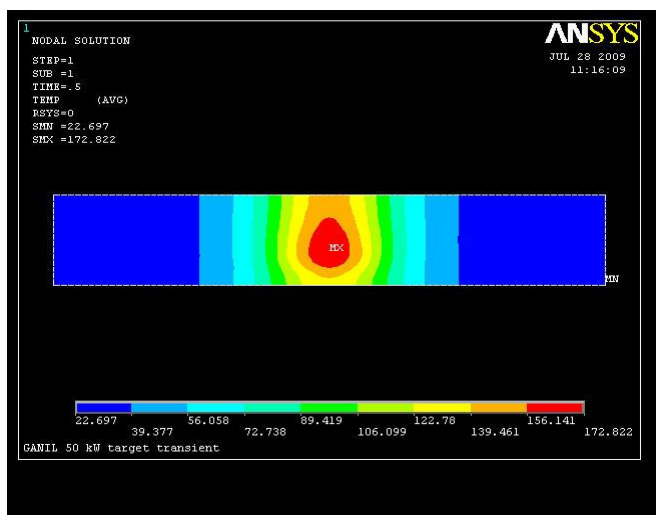


Figure 3.7. Left – MPG-6 graphite heat conductivity vs. neutron fluence at  $T = 950 - 1050^\circ\text{C}$ . 1 –  $T_{\text{measure}} = T_{\text{irrad}}$ ; 2 –  $T_{\text{measure}} = 20^\circ\text{C}$ . Right – thermal conductivity curves used in the analysis.



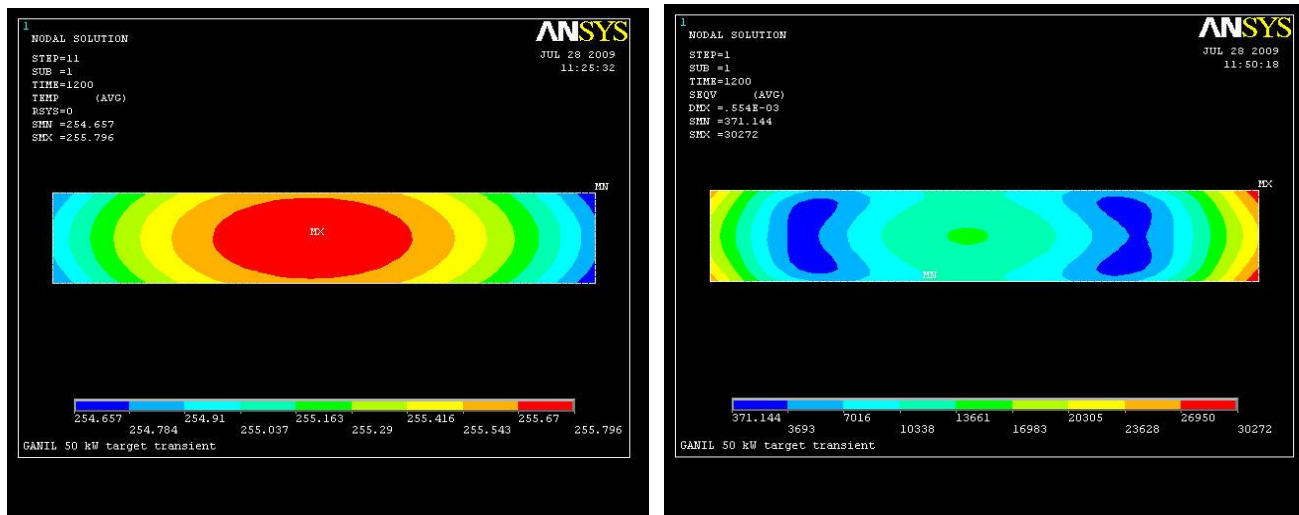


Figure 3.8. Transient analysis of MPG-6 irradiated graphite at fluence  $4 \cdot 10^{21} \text{ n/cm}^2$ . Left column– temperature ( $^{\circ}\text{C}$ ), right column – stress distribution (Pa). Data taken at 0.5 s (top row), 400 s (middle row), and 1200 s (bottom row).

Figure 3.8 shows the temperature and thermo-mechanical stress field for the irradiated converter at different time, while Figure 3.9 presents maximum temperature and stress values for irradiated and unirradiated converter all over the thermo-cycle. Maximum temperature values obtained at steady-state analysis are listed in Tab. 4.2.

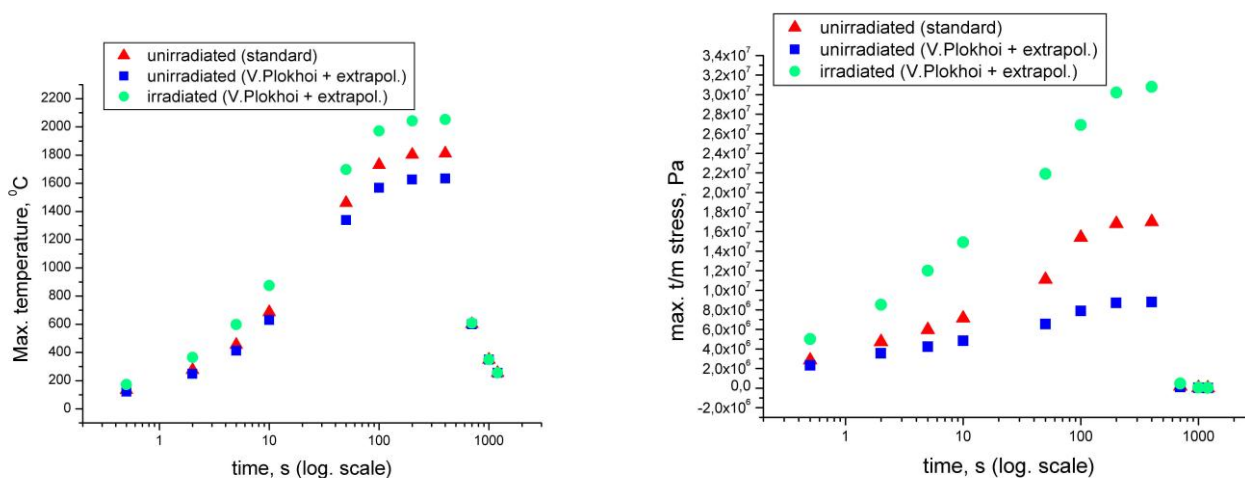


Figure 3.9 Left – maximum converter temperature vs. time, right – maximum thermo-mechanical stress vs. time for irradiated and unirradiated MPG-6 graphite.

Table 3.2. Maximum converter temperatures for irradiated and unirradiated MPG-6 graphite converter. Data of VNIITF for  $4 \cdot 10^{21} \text{ n/cm}^2$  fluence; steady-state analysis.

	unirrad. standard	unirrad. MPG-6	irrad. MPG-6
Max. converter temp., $^{\circ}\text{C}$	1813	1633	2053

The analysis reveals the essential temperature and stress growth during the heating up, which is probably a result of the insufficient modeling of thermal conductivity curve for irradiated graphite. Building this dependence one has to take into account the annealing effects, so the measurements for Figure 3.7, should be done also at the operating temperature of 1850 °C.

The deuterons are most responsible of radiation damage in the graphite of the converter. In fact, the 40 MeV, 5 mA deuteron beam is stopped inside the graphite, its path is 5,6 mm and produces an high amount of damage in a region close to the Bragg peak [25] Calculations show that at zero temperature and without considering the annealing process, the amount of damage in graphite reach 50 dpa. The annealing at high temperature is playing a fundamental role in recovering such a damage. This is especially important when radiation load to material is non-uniform because of target rotation (irradiation during ~0.01 s is followed by ~0.99 s of annealing).

The effect of annealing has been evaluated by molecular dynamic calculations. The diffusivity of defects in function of the temperature has been studied and a diffusivity coefficient of  $10^{-10} \text{ m}^2/\text{s}$  were calculated for a temperature of 1.800°C. The concentration of deuterium nuclei is maximal near the region where the impact of radiation on material (graphite) is maximal and amounts  $\sim 2.3 \cdot 10^{-8} \text{ deuterons/atoms}\cdot\text{s}$ . The maximal displacement rate in graphite is  $\sim 1.3 \cdot 10^{-6} \text{ displacements/atoms}\cdot\text{s}$  and the maximal dose rate is 0.55 MGy/s. An experimental campaign is in progress to measure the effective radiation damage induced by deuterons at high temperature ( $> 300 \text{ }^\circ\text{C}$ ).

Radiation damage induced at the level of delay window and cooling panels is rather negligible. The results of calculations are shown in Table 3.3.

**Table 3.3. Radiation damage induced on the converter assembly.**

<b>Material</b>	<b>Radiation damage [dpa]</b>	<b>Radiation source</b>
Graphite	< 50	Deuteron beam
Delay window (Stainless Steel )	0.85	Neutrons
Wheel body (Stainless Steel )	$10^{-3}$	Neutrons
Cooling panels (Stainless Steel )	$10^{-2}$	Neutrons

Among the peculiarities of the of deuterium ions radiation effect on material it can be mentioned that the most energy is spent on ionization and excitation of surrounding atoms,  $\Delta E_i$ . The process is statistic (random) and leads to not only the spread of thermalized interstitial ions and energy contribution, but also to a spatial dependence of the density of displaced atoms. The dependence of deuteron density on depth is defined not only by average ionization and excitation losses  $\left(\frac{dE}{dx}\right)_i$ , but also by angular spread from elastic collisions and energy loss fluctuations due to statistic moderation.

Less deuterium energy,  $\Delta E_d$ , is spent on defect generation. Ion energy losses due to defect generation are also statistic (random) and form a spatial dependence of deuterium density and, hence, of defect density. When, however, the initial energy of deuteron is rather high (40 MeV in our case), density variations from defect generation (the elastic interaction of deuterium with surrounding nuclei) are small and account for energy fluctuations may be of great importance for the correct evaluation of the spatial dependence of the density of defects and interstitial deuterium nuclei.

In order to evaluate the effect of ionization loss fluctuations on the defect and interstitial atom density distribution, it was modified the ATOCAS code so as to make it capable of predicting energy fluctuations by the Vavilov model and simulating small-angle scattering for high-energy ions in the Gaussian approximation. Besides these modifications, deuterium and displaced carbon nuclei were tracked as proposed by Samarin et al [9]. Elastic scattering was described with the Mollier potential and ionization stopping power which, in its turn, was described with the Biersack model [9] with a correction factor of the Linchard-Sharf formula  $k/k_L=1.25$ .

In this regard, Figure 3.10 to Figure 3.15 show the result of simulation for displacements rate with the next deuteron beam parameters: current 5mA, Gaussian distribution with density

$$f_{xy} = \frac{1}{2\pi \cdot \sigma^2} e^{-\frac{((x-x_0)^2+(y-y_0)^2)}{2\sigma^2}}, \text{ where } (x_0, y_0) \text{ are coordinates of the beam center and } \sigma=1\text{cm.}$$

Deuteron energy is 40MeV.

Beam operation time is 10000h.

The atomic displacement energy was taken from Molecular Dynamics (MD) simulations [10],  $E_d=17$  eV.

From Figures 3.10 to 3.15 the dose peak occurs somehow earlier than the displaced atoms peak, which, in turn, occurs a little earlier than the peak of implanted deuterons. The concentration

---

of deuterium nuclei is maximal near the region where the impact of radiation on material (graphite) is maximal and amounts  $\sim 2.3 \cdot 10^{-8}$  *deuterons/atoms·s*.

The maximal displacement rate in graphite is  $\sim 1.3 \cdot 10^{-6}$  *displacements/atoms·s*. The maximal dose rate is 0.55 MGy/s

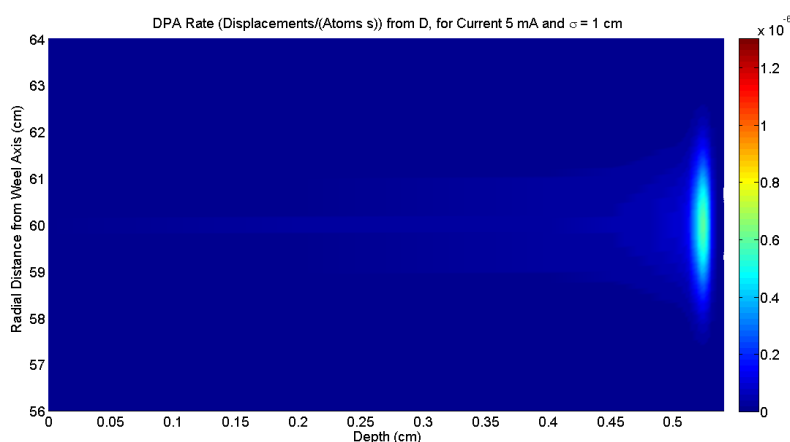


**Figure 3.10. The spatial distribution of displacement rate from deuterium nuclei; the average number of displaced nuclei per one deuterium nuclei is 74.**

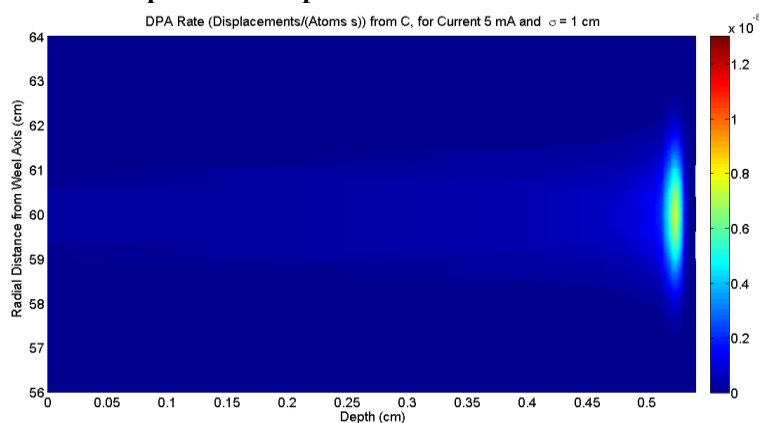


**Figure 3.11. The spatial distribution of displacement rate from carbon nuclei; the average number of displaced nuclei per one deuterium nuclei is 114.**

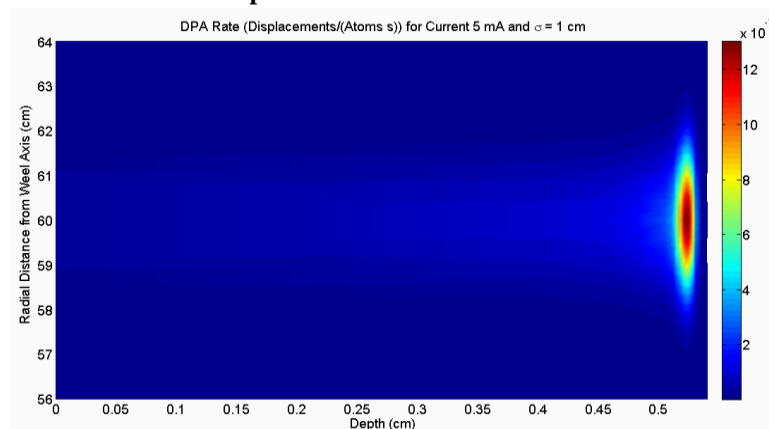


**Figure 3.12. The spatial distribution of nuclear displacement rate; the average number of displaced nuclei per one deuterium nuclei is 188 (52 replacements).**

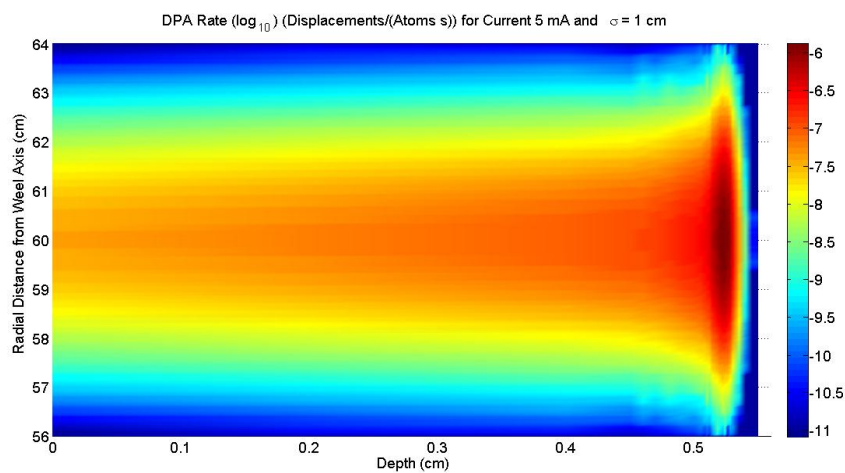


**Figure 3.13. The spatial distribution of nuclear displacement rate**

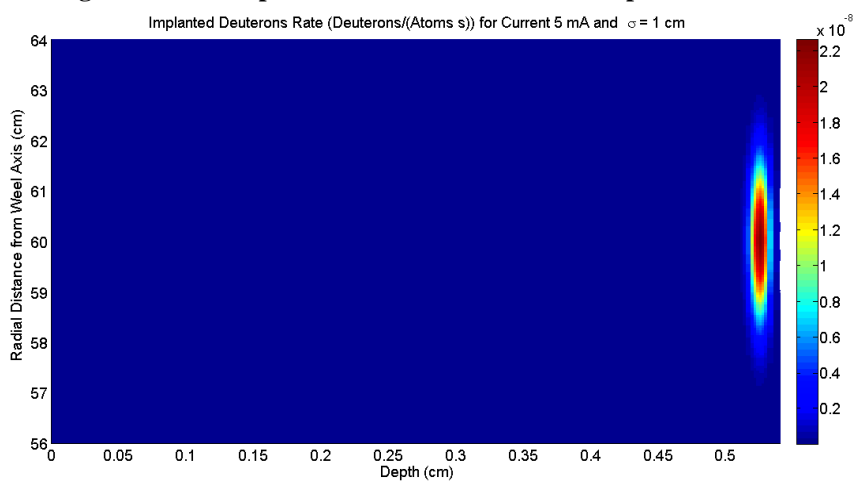


**Figure 3.14. Spatial distribution of implanted deuteron rate**

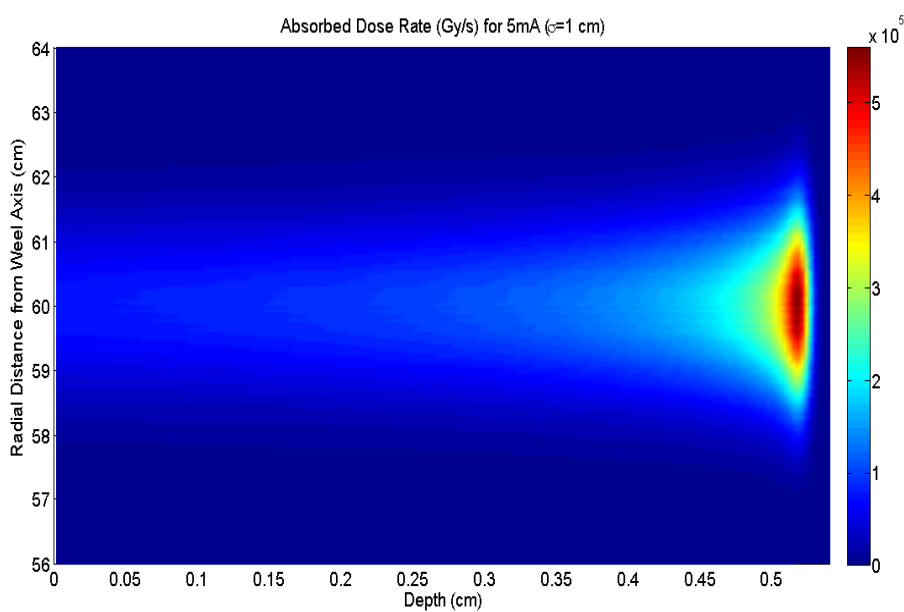


**Figure 3.15. Spatial distribution of absorbed dose in the graphite target**

### 3.3.2. Graphite Lattice Defects

According to [17], defects in graphite can be classified into two types, i.e., defects caused by interlayer structure faults and bond defects in carbon networks. The former defects are stacking faults characterized by disordered packing of parallel layers of hexagonal networks. The latter type of graphite structure distortions is caused by defects in carbon network bonds. Among them are vacancies and their groups, impurity atoms embedded into the hexagonal layer, isomeric bond defects (when  $sp^3$  hybridization is characteristic of some atoms), and edge defects.

The main types of bond defects are as follows.

- Edge defects when the C-C bond cannot be formed, e.g., if one molecule is not in the plane of its nearest neighbors.
- 2. "Claw" or "split" defects, i.e., voids or discontinuities in the hexagonal network of carbon atoms, caused by bond breaking. Screw dislocations or other distortions in the hexagonal network can arise near claw defects.
- Twinning defects, i.e., alternating rings consisting of four and eight atoms, formed in the twinning line. It should be kept in mind that there are two twinning types. One is intergrowth-type twinning called the basal twinning whose axis is parallel to the «c» axis of the graphite lattice. In this case, crystal formations consisting of two or several parts identical in composition and structure but not identical in shape and size, regularly arranged with respect to each other, are observed. The regularity is that the lattice of one part is superposed with another by rotation about the twin axis.

Another twinning type is non-basal; it is caused by reflection in the twin plane or by combined rotation and reflection. Non-basal twinning implies the existence of the symmetry plane (the mirror reflection plane referred to as the twinning plane) and appears as bending of the system of graphite planes at a certain angle.

For the hexagonal graphite structure with layer packing sequence ABAB, there are only two angles ( $48^{\circ}18'$  and  $35^{\circ}12'$ ) of true twinning. In other cases, symmetry laws are violated, i.e., the layer sequence to the left and right from the interface is not retained even for a symmetric tilt boundary. This suggests that the formation of symmetric and especially asymmetric tilt boundaries of crystals should be accompanied by numerous bond breakings and a rather developed system of edge dislocations.

Moreover, there exist foreign atom inclusions into the carbon network and defects caused by atomic displacements from normal lattice sites.

---

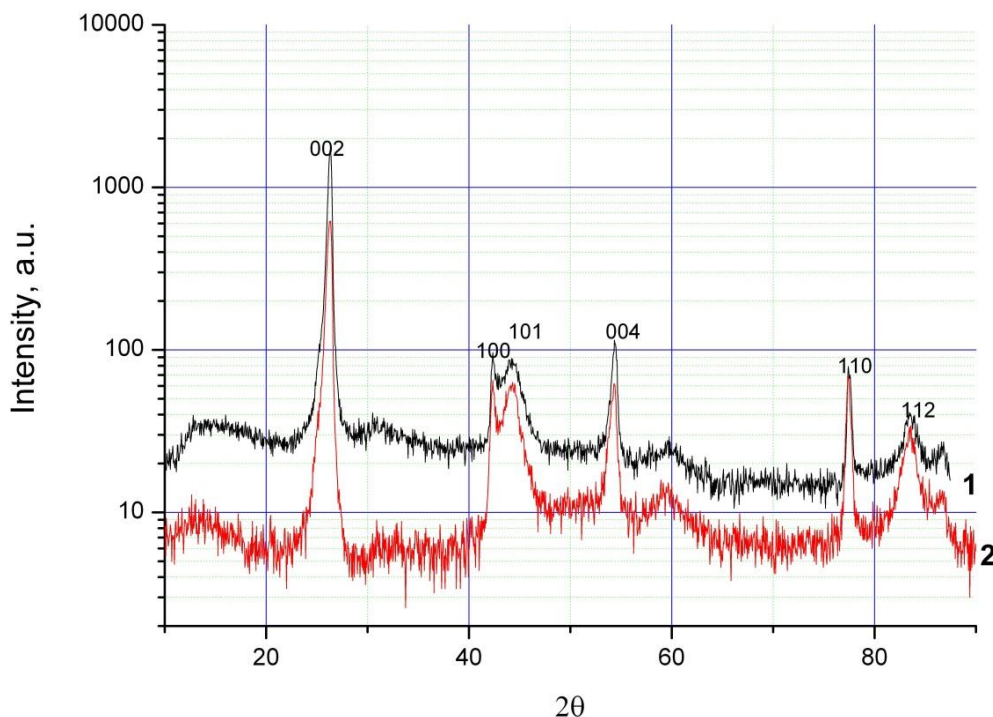


**Figure 3.16. X-ray pattern of fine-grained dense CGD graphite samples in semilogarithmic scale. Curves 1 and 2 correspond to a compact plate and ground sample, respectively. The 002 peak height is appreciably larger in the former case, since the plate is characterized by the texture, i.e., the preferred orientation in the [001] direction. For POCO and MPG-6 graphite samples, x-ray patterns are almost identical to curve 2.**

The lattice parameters of all three samples are identical within estimated errors. The CSR sizes in the graphene layer plane are also rather close. Certain differences are observed in the sample microstructure in the [001] direction. The CSR sizes in the CGD sample are significantly smaller, although the value of microdistortions (variations of interlayer distances) is also smaller.

This indicates the presence of thinner but more ordered of graphite network stacks in this sample in comparison with MPG-6. Here the best ordering means only smaller variations in interlayer distances, rather than the layer stacking defect density which, judging by the peak broadening anisotropy, is identical in both samples. Calculations of the CSR in the [001] direction for CGD samples correlate well with electron microscopy data, since it is obvious that the height of ordered stacks can be appreciably smaller than 30 nm.

It can be considered that the characteristic feature of POCO graphite is the slightly increased interlayer distance at an ordinary value of microdistortions.

### 3.3.3. Estimation of a radiation durability of graphite and steel

Operational resource of the graphite target and structural steel elements will be defined by radiation load caused by exposure to radiation of deuterium ions with energy  $E_d = 40$  MeV and fast neutrons generated in the target.

Exposure to ionizing radiation leads to accumulation of radiation damages in the target structural materials which appear in the following effects: creep of materials, radiation-induced swelling, strengthening accompanied by increase of material solidity and hardness and reduction of its plasticity; heat conductivity reduction etc.

Numerical measure of radiation damage in material is number of atom displacements. This quantity depends on type of radiation, its energy spectrum, duration and intensity of irradiation. Often in the literature neutron radiation effect on materials is characterized by fast neutron ( $E > 0.1$  MeV) fluence. In order to find relation of this quantity to neutron induced atom displacements calculations of radiation transport for a model system using computer codes PRIZMA and ATOCAS were carried out.

With PRIZMA code transport of neutrons from point mono-directional (along normal to layer surface) neutron source with different energy distributions: fission spectrum, neutron spectrum of  $^{12}\text{C}(d,n)^{13}\text{N}$  reaction with  $E_d = 40$  MeV and different outgoing direction angle  $\alpha$  (with respect to deuteron direction of incidence) was simulated in a plane layer of matter (iron,  $\rho_{\text{Fe}} = 7.85$  g/cm<sup>3</sup> or graphite,  $\rho_{\text{C}} = 1.85$  g/cm<sup>3</sup>) 1 cm thick. After that total number of displacements was defined using ATOCAS code taking into account spectrum of initially knocked-out atoms. Here minimum energy value needed to displace an atom was calculated using molecular dynamics method with MOLOH code and was assumed to be equal to  $E_{\text{chaFe}} = 9.25$  eV for iron,  $E_{\text{chaC}} = 17$  eV for graphite. Calculation results are listed in Table 2.4, where

$$\Phi_V = \int_V d\vec{r} \Phi -$$

integrated over layer volume  $V$  neutron fluence,  $N_{\text{IKA}}$  – number of initially knocked-out atoms per one source neutron,  $N_{\text{disp}}$  – number of displacements per IKA,  $N_{\text{dpa}\Phi}$  – number of displacements per atom (DPA) of matter per unit neutron fluence,  $\Phi_{\text{dpa}}$  – neutron fluence corresponding to 1 dpa.

---

**Table 3.4. Calculation results for the model system [1].**

Spectrum type	Material	$\Phi_V$ , cm	$N_{IKA}$	$N_{disp}$	$N_{disp}\Phi$ cm <sup>-1</sup>	$N_{dpa\Phi}$ , 10 <sup>-21</sup> cm <sup>2</sup>	$\Phi_{dpa}$ , 10 <sup>20</sup> cm <sup>-2</sup>
fission	graphite	1.2	0.28	$7.34 \cdot 10^2$	172	1.9	5.4
fission	iron	1.25	0.32	$1.70 \cdot 10^3$	435	5.1	1.9
$^{12}\text{C}+d, \alpha=180^0$	iron	1.23	0.29	$3.50 \cdot 10^3$	825	9.8	1.0
$^{12}\text{C}+d, \alpha=90^0$	iron	1.24	0.30	$3.08 \cdot 10^3$	764	9.0	1.1
$^{12}\text{C}+d, \alpha=50^0$	iron	1.21	0.25	$4.19 \cdot 10^3$	866	10.2	0.98
$^{12}\text{C}+d, \alpha=30^0$	iron	1.19	0.21	$5.05 \cdot 10^3$	891	10.5	0.95
$^{12}\text{C}+d, \alpha=0^0$	iron	1.16	0.18	$5.65 \cdot 10^3$	877	10.4	0.96

As it follows from table data harder neutron spectrum of  $^{12}\text{C}(d,n)^{13}\text{N}$  reaction in comparison with fission spectrum causes  $\sim 2$  times more displacements in iron. Ratio of number of displacements in iron to absolute value of neutron fluence of  $^{12}\text{C}(d,n)^{13}\text{N}$  reaction weakly depends upon outcoming angle, and in this case it can be considered that 1 dpa corresponds to neutron fluence equal to 1020 cm<sup>-2</sup>. With fixed neutron fluence of fission spectrum number of atom displacements in graphite is  $\sim 3$  times less than in iron.

Let's consider effect of neutron radiation generated in the target during facility operation on its structural elements. Given current in the deuteron beam equal to  $I_d = 5$  mA and total neutron yield from reaction  $^{12}\text{C}(d,n)^{13}\text{N} \sim 4.35 \cdot 10^{-2}$  n/d, including outcoming in the angle  $< 50^0$  -  $\sim 1.55 \cdot 10^{-2}$  n/d, neutron flux density at the distance of 5..10 cm would be at the level of  $\varphi_n \sim (2...8) \cdot 10^{12}$  cm<sup>-2</sup>s<sup>-1</sup>. If required service life is taken to be  $T \sim 10^4$  h ( $3.6 \cdot 10^7$  s), then total neutron fluence effecting target unit elements is  $\Phi_n \sim (0.7...3) \cdot 10^{20}$  cm<sup>-2</sup>, what corresponds to number of displacements equal to  $\sim 0.7...3$  dpa in steel and not more than 1 dpa in graphite according to table 1 data.

Taking into account the relatively low neutron yield from  $^{12}\text{C}(d,n)^{13}\text{N}$  reaction ( $\sim 4\%$ ) it can be expected that major radiation damages in the target material – graphite would be caused by high energy deuterons of the beam.

Calculation results obtained using ATOCAS code showed that under exposure to deuteron radiation with energy  $E_d = 40\text{MeV}$ , current  $I = 5$  mA and Gaussian distribution of the beam density in the transversal section with specific extent of the spot  $\sigma = 1$  cm, maximum rate of displacement generation in graphite is observed at the end of deuteron path ( $R_d = 0.525 \pm 0.006$  cm) at the depth corresponding to the Bragg peak, and amounts to  $1.3 \cdot 10^{-6}$  dpa/s [1]. Therefore during target

operation time maximum number of displacements in graphite will be at the level of 50 dpa, what is equivalent (see table 1) to neutron effect with fast neutron fluence of  $\sim 2.5 \cdot 10^{22} \text{ cm}^{-2}$ .

Irradiation effect on materials can be characterized by threshold value of some quantity: number of displacements per atom, fluence, absorbed dose etc. If the value of such quantity is lower than the threshold value then irradiation effect can be neglected. If it is higher than the threshold value (an order of magnitude) then it can be easily established and measured [2]. Thus for different types of steel fast neutron fluence threshold can be taken equal to  $10^{21} \text{ cm}^{-2}$  [2], what corresponds to  $\sim 5$  dpa according to table 1.

It is the very level of irradiation at which effects related to reduction of plasticity, brittle-viscous transition temperature, increase of fluidity threshold begin to appear (in addition considerable strengthening and embrittlement appears at the level of irradiation of  $\sim 10$  dpa [3]). These values are much higher than the level of irradiation of steel elements in the target unit structure during its operation, therefore neutron radiation doesn't impose any limits on facility operation mode.

Radiation effect on graphite properties also appears in increase of its mechanical strength (especially under compression), hardness, modulus of elasticity value, reduction of plasticity. Moreover it is typical for graphite that under high temperature its heat conductivity decreases, its dimensions change and become unstable.

Multifold (40..50 times) heat conductivity reduction is observed even at neutron fluence value of the order of  $10^{19} \dots 10^{20} \text{ cm}^{-2}$  [2], but this effect appears at relatively low temperature (not greater than  $200 \text{ }^{\circ}\text{C}$ ). Under higher temperature typical for target operation ( $\sim 1800 \text{ }^{\circ}\text{C}$ ) heat conductivity of irradiated graphite restores due to radiation annealing.

One of the major factors of irradiation effect on graphite is its dimension changes (such as length growth in one direction and its reduction in the other one). Thus under long-term irradiation initial lengthening in the longitudinal direction is changed by shortening, after that under further irradiation increase of dimensions is observed again. However under temperature growth graphite dimensional changes decrease, and under temperatures higher than  $350 \text{ }^{\circ}\text{C}$  most samples even shrink.

In general graphite dimensional change under long-term irradiation depends on many factors: anisotropy degree related to the ways of graphite production, irradiation temperature, type of irradiation (e.g. fast or thermal neutrons), fluence value. Thus according to [2] under exposure to fast neutron flux maximum changes of graphite samples can amount to 2...3% given fluence values of  $1.0 \dots 1.5 \cdot 10^{22} \text{ cm}^{-2}$  ( $\sim 20 \dots 30$  dpa). However under further fluence growth (to the value of  $\sim 2.5 \cdot 10^{22} \text{ cm}^{-2}$ ) tendency to restore initial dimensions of the samples is observed. Moreover long-term annealing of graphite under temperature of  $\sim 2000 \text{ }^{\circ}\text{C}$  (close to graphitization temperature)

---

leads to radiation damage elimination and restoration of properties of strongly irradiated graphite [2].

Thus taking into account the target unit design, namely the way of graphite elements fixing, irradiation conditions (target temperature  $\sim 1800$  °C, irradiation duration  $T \sim 10^4$  hours given average deuteron flux density at the target  $\phi \sim 2 \cdot 10^{13}$  cm<sup>-2</sup>s<sup>-1</sup>), as well as relatively low level of maximum thermo-elastic stress, appearing in the target graphite during irradiation,  $\sim 30$  MPa [4], one can expect that considered above factors related to radiation damage in graphite, wouldn't impose serious limits on target operation during its service life. At the same time major effect on target operation resource can be caused by such effect as evaporation of graphite from target surface under its heating up by high energy deuterons.

According to [5] threshold temperature value for which this effect begins to appear for different types of graphite can be taken to be equal to  $T_e \sim 1850$  °C (graphite evaporation rate for this temperature is  $10^{-3}$  mm/month).

For greater temperature values it can be observed rapid growth of evaporation rate, and for temperature equal to  $2000$  °C the rate value reaches  $0.03$  mm/month and further increases in order of magnitude with temperature growth by every  $\sim 100$  °C.

If maximum allowable temperature of target's surface is taken to be  $T_{\max} = 2000$  °C then during expected service life target thickness decreases approximately by  $\sim 0.5$  mm, what it seems to be quite allowable. Here however it must be considered effect of thermal energy or deformation energy accumulation in graphite crystal lattice caused by radiation defects in the process of irradiation.

Energy accumulated in graphite increases to some critical value (at the level of  $1 \dots 3$  kJ/g), after reaching which it is released in the form of heat, what can lead to rapid growth of graphite temperature [2]. Although under high temperature (higher than  $1000$  °C) this effect decreases (an order of magnitude or more) due to annealing it is desirable to have some target temperature allowance not letting it to exceed the value of  $1850 \dots 1900$  °C during the process of irradiation.

### 3.4. Life Time

According to [7, 8] the predicted lifetime of the neutron target converter based on fine-grained dense graphite can be roughly approximated by the simple Zhurkov's formula based on the representations of the thermal-fluctuation nature of solids fracture:

$$\tau = \tau_0 \exp[(U_0 - \gamma\sigma)/kT]$$

Where  $k$  is the Boltzmann constant,  $\tau_0$  is atomic thermal vibrations period equal to  $\sim 10^{-13}$  s,  $U_0$  is the initial activation energy of the destruction process that is reduced by the applied stress

---

$\sigma$ ;  $\gamma = qVa$ ;  $Va$  is the activation volume in the elementary act of fracture,  $q$  is the local overstress ratio. Because of local defects this coefficient reaches the values of 10–100, and the magnitude  $U_0$  is close to sublimation energy in many cases.

Using the data on MPG-6 sample lifetime temperature dependence presented in [2] and rebuilt in Arrhenius coordinates (Figure 3.17); the predictable lifetime of a neutron target converter was determined to be about  $10^4$  hours at 2200°C operating temperature. Same lifetime prognosis for CGD graphite based converter requires the operating temperature reduction down to 1800°C.

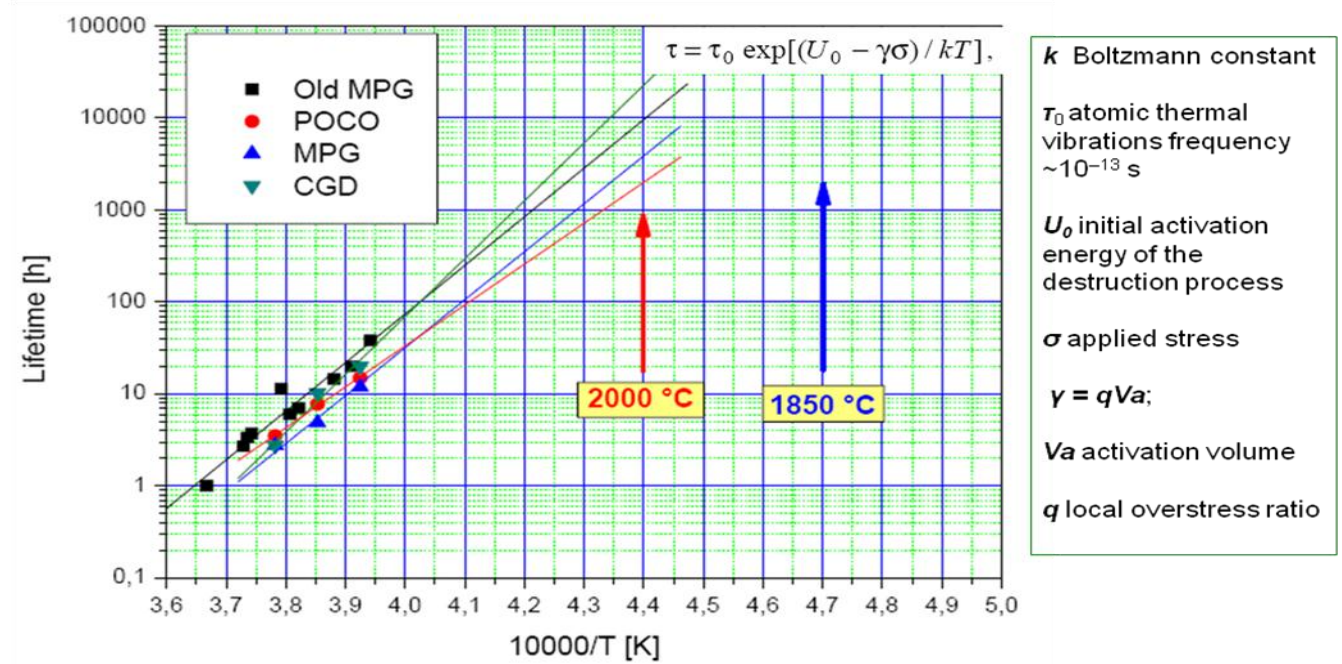


Figure 3.17. Lifetime dependence vs return temperature for MPG samples (at the left) and CGD samples (on the right).

### 3.5. Material Selection

The most suitable materials for the neutron converter are fine-grain (1 - 10  $\mu\text{m}$ ) and relatively low density (1,7 - 1,8  $\text{g/cm}^3$ ) graphites. In particular three kind of graphites were tested, MPG, CGD and TM-1/AXF-5Q. All of them have very similar structures and thermo-mechanical characteristics. For commercial reasons the TM-1/AXF-5Q of POCO-graphite have been selected.

Swelling is the most dangerous process and is mainly due to the hydrogen (deuterium) accumulation in graphite. The graphite of above due to small grains and low density show high radiating resistance concerning the swelling and keep sufficient heat conductivity ( $\sim 25 \text{ W/m}\cdot\text{K}$ ) at neutron fluence up to  $10^{22} \text{ n/cm}^2$ . This fluence correspond to about a radiation damage of 50 dpa ( $10^4$  hours of irradiation with 5 mA deuteron beam). It is well known that the swelling of MPG graphite is 4%, at temperature range of 750 - 1.000 °C and a fluence of  $2 \times 10^{22} \text{ n/cm}^2$ .

The neutron irradiation of the metallic components leads to an accumulation of radiation damages in steel which induces different effects i.e. creep, radiation swelling, hardening accompanied by increase of hardness and durability of a steel and reduction of its plasticity, decrease in heat conductivity, etc.

Neutron fluence of  $10^{21} \text{ cm}^{-2}$  (corresponding to about 5 dpa) is usually taken as a limit above which the steel experience a reduction of plasticity. The strengthening and the embrittlement appears at the level of 10 dpa radiation level.

These radiation limits are much higher than the radiation level experience by the metallic components of the converter.

Calculations show that for the metallic components of the converter is necessary to use heat resistant steel and alloys. Standard AISI 316 Stainless Steel or similar radiation resistant reactor steel can be used.

Several tests on reactor heat resistant steel have been done by the Mechanical Properties Laboratory of the Metal Physics Institute Ural Branch RAS of Snezhinsk. Table 3.5 shows some heat resistant characteristics of the Russian dispersion-hardening steels for nuclear reactors type X12H22T3MP (EI 696M) and X15H35T3B2Yu (EI 787). The main composition of both Stainless Steel s is shown in Table 3.6. The characteristics of analogous steels available in Germany, Japan and United States are shown in Table 3.7.

**Table 3.5. Heat resistant characteristics of the Russian dispersion-hardening steels.**

Steel	Stress [MPa]	Time to destruction [h]	Test temperature [°C]
X12H22T3MP	700	>10.000	500
X12H22T3MP	350	10.000	600
X12H22T3MP	450	1.500	600
X12H22T3MP	300	10.000	650
X12H22T3MP	250	10.000	700
X15H35T3B2Yu	570	10.000	550
X15H35T3B2Yu	450	10.000	600

X15H35T3B2Yu	300	>>10.000	600
X15H35T3B2Yu	240	10.000	700

**Table 3.6. Composition of heat resistant Russian steels (in mass %) in accordance with GOST 5632-72 GOST 5632-72. Corrosion-resistant, heat-resistant and creep resisting high-alloy steel and alloys.**

Steel	C	Si	Mn	Cr	Ni	Ti	Al	W	Mo	Fe
X12H22T3MP	< 0,10	< 0,5	< 0,6	10	21	2,6	< 0,8	-	1,0	Base
				12,5	25	3,2			1,6	
X15H35T3B2Yu	< 0,08	< 0,6	< 0,6	14	33	2,4	0,7	2,8	-	Base
				16	37	3,2		1,4		

**Table 3.7. Composition (in mass %) of German, Japanese and USA analogues of a the Russian heat resistant steel.**

Steel	C	Si	Mn	Cr	Ni	Ti	Al	V	Mo	Fe
DIN 17240 Germany	< 0,08	< 1	< 2	14,5	26	2,1	< 0,8	0,3	1,25	Base
JIS G-4311 Japan	< 0,08	< 1	< 2	13,5	24	1,9	0,35	0,1	-	Base
				16	27	2,3		0,5		
AISI 316 Unite States	0,08	1,0	2,0	16	10	-	-	-	2	Base
				18	14				3	

The structural material selected for the construction of the neutron converter and the delay window is the AISI 316L Stainless Steel for the components working at low temperatures and the Stainless Steel 316LN for the components working at high temperature, as the cooling panels, because of its lower dilatation coefficient.

## CHAPTER 4. THERMOMECHANICAL DESIGN

In order to define the loads acting on the graphite wheel, that means, the energy distribution all over the converter, it has been determined the number of particles per unit of area according to the Gauss beam distribution for both cases, 50 and 200 kW respectively. After experimental measurements it can be obtained the energy distribution in Figure 4.1 and Figure 4.2.

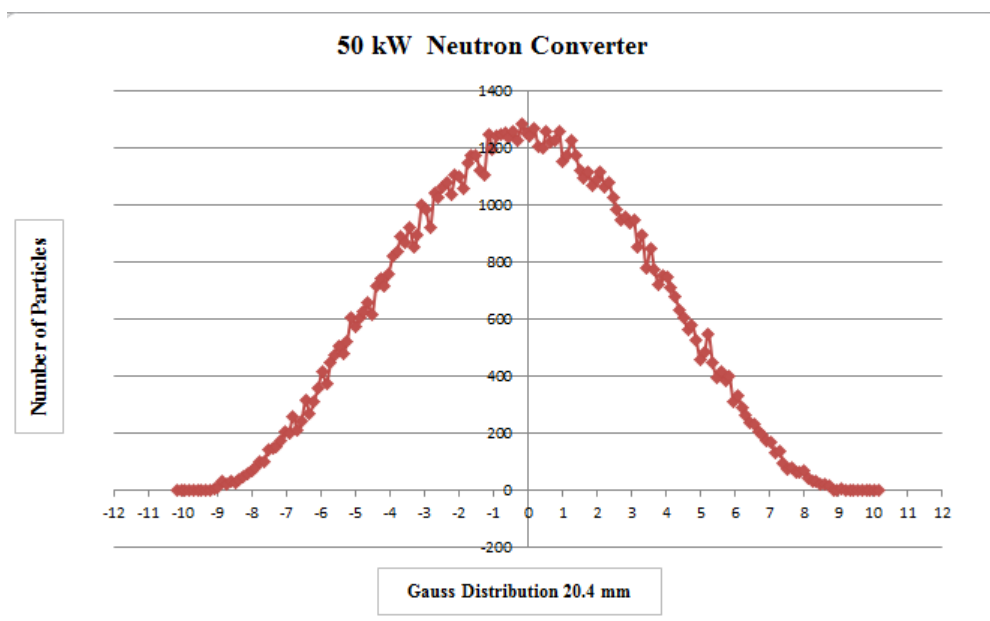


Figure 4.1. Gauss Distribution of Deuteron Primary Beam of 50kW

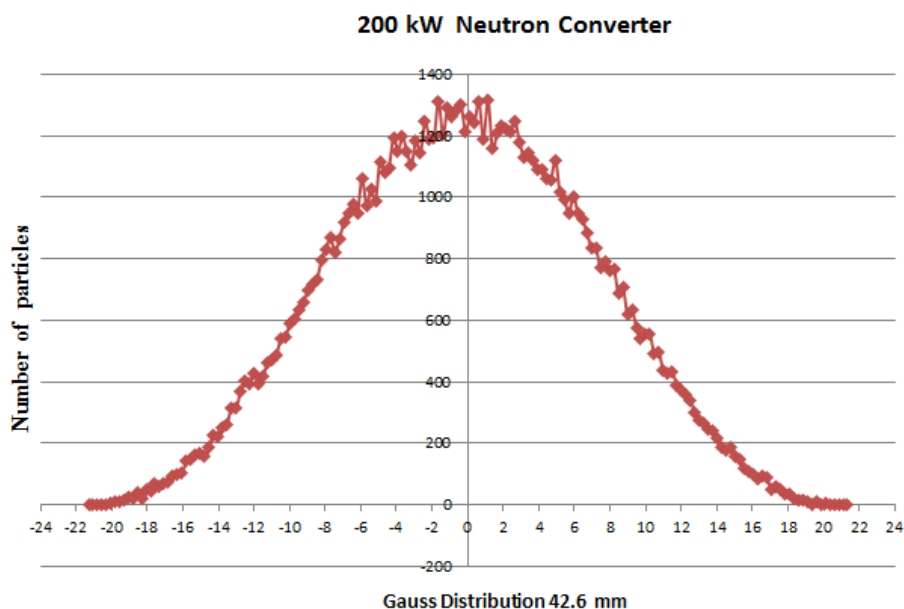


Figure 4.2. Gauss Distribution of Deuteron Primary Beam of 200kW

#### *4.1. Neutron Converter*

Before the experiments with the prototype could start, the simulation of the virtual model was carried out aimed at the estimation of the basic thermal and mechanical parameters of the prototype (temperature distribution, temperature gradient, stress, deformation), at the determination of the most strained parts of the construction, and at the prediction of the prototype behaviour under the beam of nominal power and size. The simulation has been performed using the finite elements method on the basis of ANSYS program complex.

Thermal and structural loads were applied to the target model. Thermal loads include the volume heat generation in the converter (or a surface heat flux in case of 50 kW converter) and the uniform temperature of the shaft, which is actually around 350 °C due to contact with liquid metal. Heat generation was applied in the form of tabular values of heating power volume density distributed over the converter.

Both deuteron beam and calculated beam power losses in the converter are taken into account. Heating power distribution along the converter azimuth is considered as uniform. Structural loads include the inertia forces due to target rotation. In order to prevent the rigid body motion during the calculations, some DOF constraints are applied that fix degrees of freedom at a certain node of the model.

For radiation problem solution, the radiation matrix method is selected. It involves generating a matrix of form factors between radiating surfaces and using this matrix as a superelement in the thermal analysis.

Contact problems usually involve contacting surfaces of two or more bodies that can be deformable under thermal and mechanical loads. In order to solve the thermal problem with contacts, it is necessary to set the values of heat transfer between the contacting surfaces. The actual model uses the values, which were experimentally defined during the test of the target model [4].

Contact problems in structural analysis make a few significant difficulties caused by the diversity of contact surfaces behaviour, presence of friction, etc. In the present simulation we used bonded contact model, which restricts the displacement of one contacting surface relative to the other one.

---

#### 4.1.1. 50 kW Neutron Converter

This variant of converter is designed for its test under the electron beam up to 50 kW total power. A graphite assembly with 8 mm in depth is supported by metal clamps. The virtual model for the graphite wheel is shown in Figure 4.3.

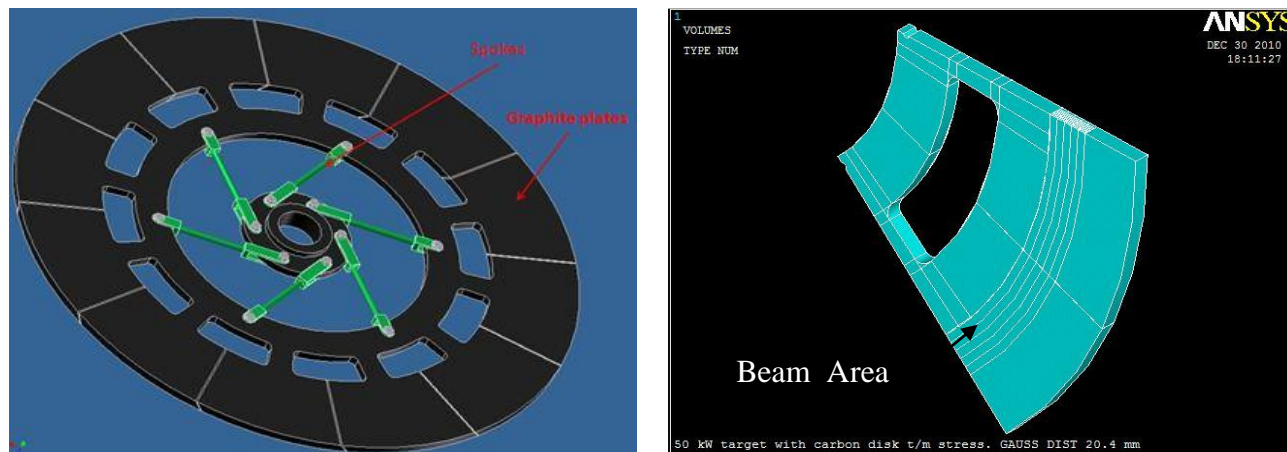


**Figure 4.3. 50 kW Graphite Wheel Model**

The sector where the beam arrives is modelled as small volumes pointed as Beam Area. In this regard, the Gaussian power distribution as a consequence of the number of particles is shown in Table 4.1; the beam distribution column indicates the geometrical partition on the graphite wheel according to the diameter of the beam  $\varphi = 20.4$  mm.

**Table 4.1. 50 kW Gauss Beam Distribution. Number of Particles and Power**

Beam Distribution $\varphi$ (mm)	Particles Number	Power (W)
-10.20	180	98.2
-8.16	2200	1145.8
-6.12	7557	3939.42
-4.08	12552	6540.5
-2.04	17938	9350.6
0.00	18652	9723.19
2.04	17410	9075.7
4.08	11463	5975.6
6.12	6315	3291.9
8.16	1577	822.08
10.20	71	37.01
20.4 mm	95915	50000

The power dissipation resulting of the beam influence through the graphite wheel was obtained after the simulation. Next figures shows a colour map with the distribution of temperatures, stress, and deformation including maximum and minimum values. Figure 4.4 shows the geometry and mesh generated for performing the simulation.

The thermal distribution obtained ( Figure 4.5 ) shows a Gaussian pattern as a result of the primary deuteron beam distribution, as it was expected, with a maximum value of 1742 °C in the centre of the beam; the temperature decreases in the metal clamp direction toward to the shaft.

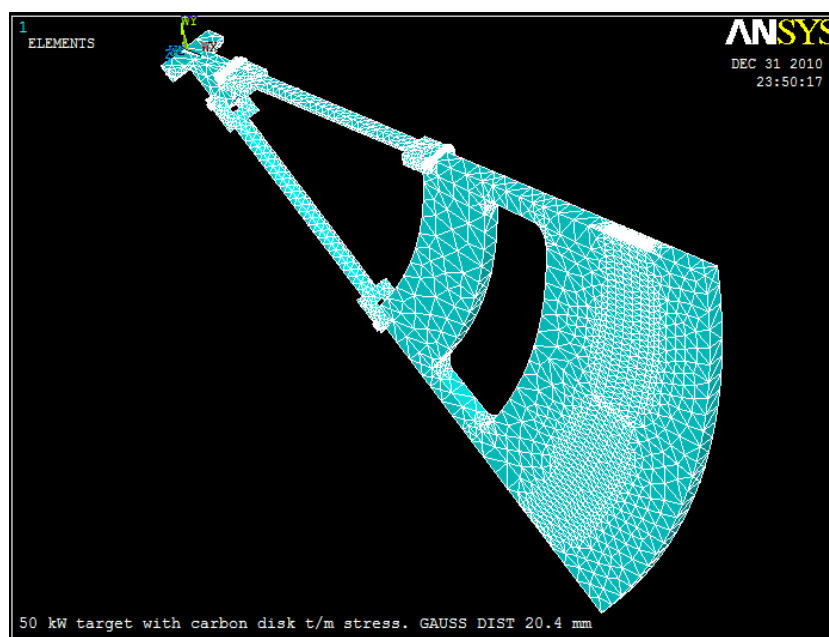


Figure 4.4. 50 kW Graphite Wheel. Geometry and meshing

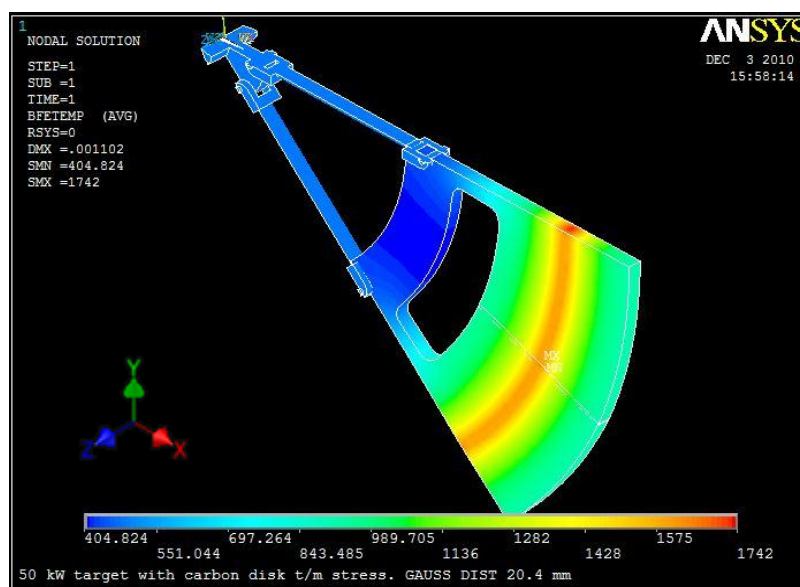


Figure 4.5. 50 kW Graphite Wheel Temperature Distribution.

The results for deformation of the graphite wheel are shown in Figure 4.6 to Figure 4.9. The most important displacements occur in the X direction with a maximum of 1.083 mm, which is the most convenient condition due to the mechanical and geometric characteristics of the neutron converter and the cooling panels. White dash line in Figure 4.9 indicates in more detail the total deformation in the three directions.

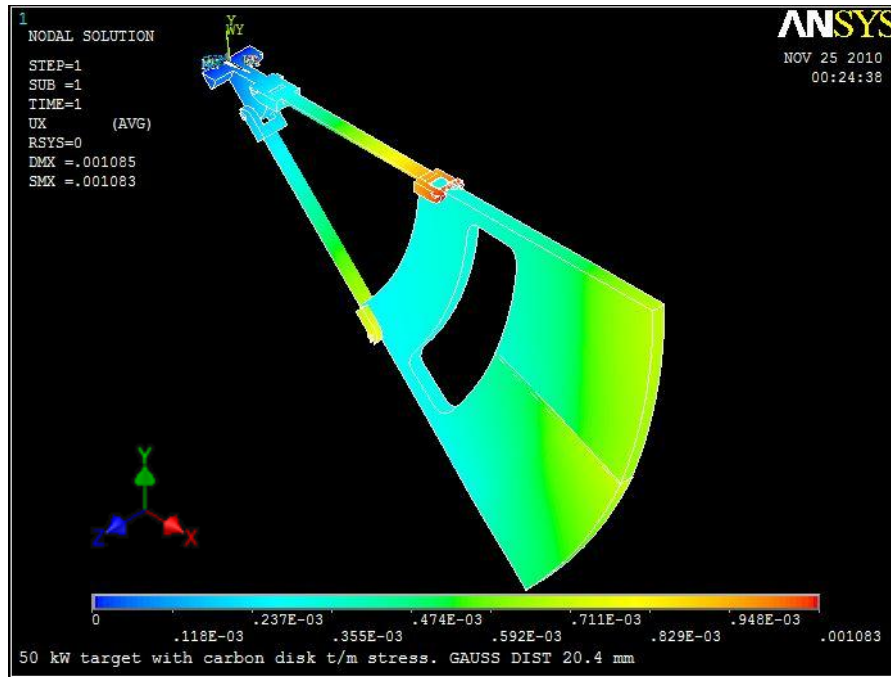


Figure 4.6.. 50 kW Graphite Wheel . Deformation in X direction

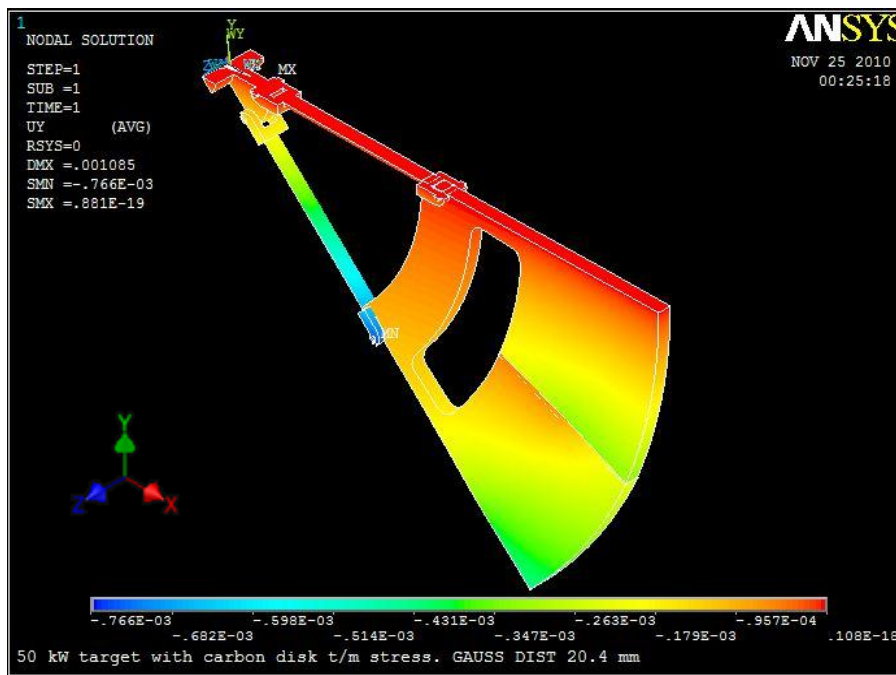


Figure 4.7. 50 kW Graphite Wheel . Deformation in Y direction

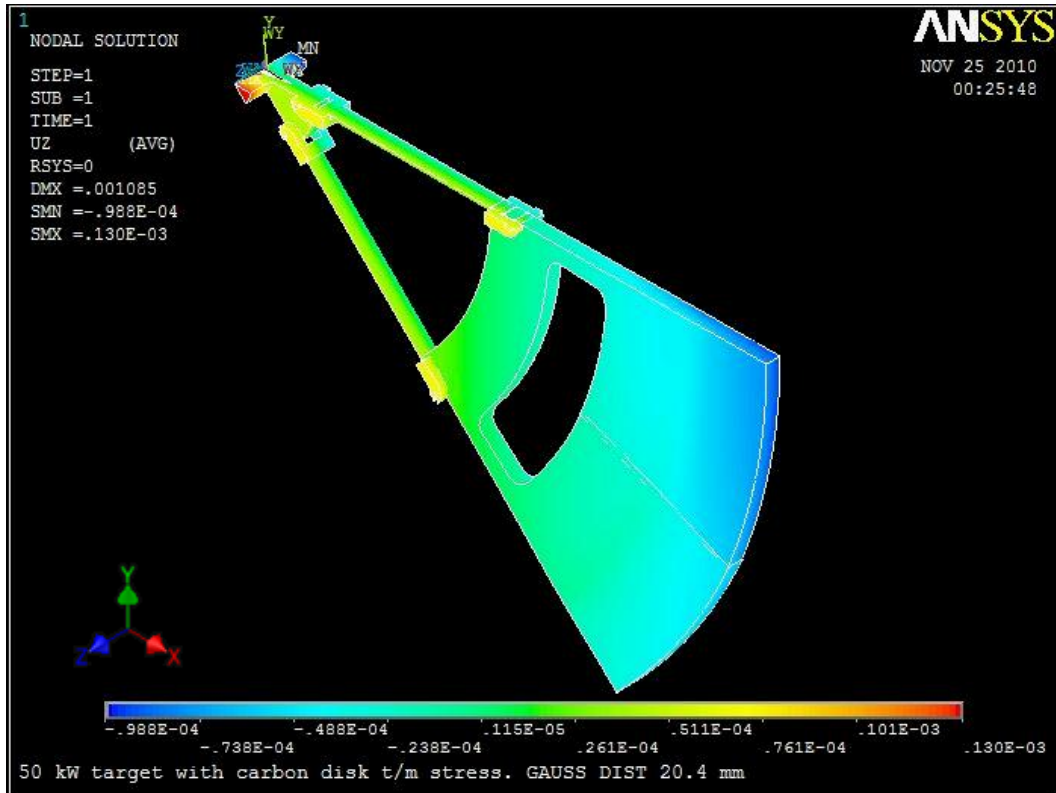


Figure 4.8. 50 kW Graphite Wheel . Deformation in Z direction

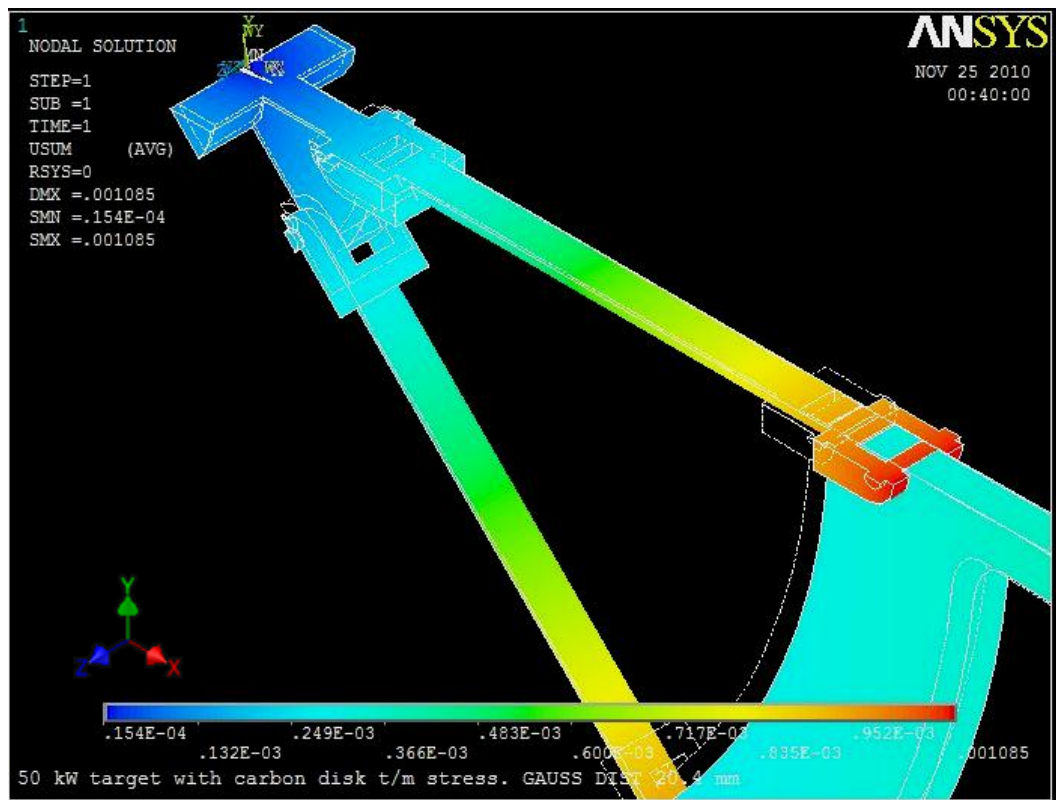


Figure 4.9. 50 kW Graphite Wheel . Total Deformation

Figure 4.10 shows the total equivalent stress for the neutron converter wheel, with a maximum value of 56.8 MPa, located in the zone with the highest concentration of power. Main results for the 50 kW neutron converter are summarized in Table 4.2.

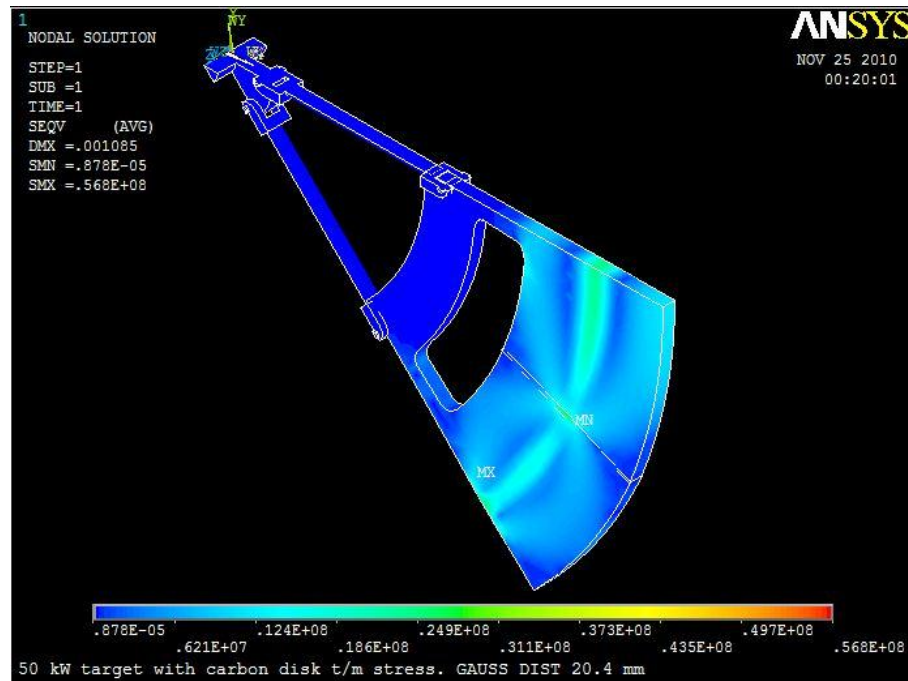


Figure 4.10. Total Stress Von Mises

Table 4.2. Summary of Maximum Values for Temperature and Stress for 50 kW Neutron Converter

Max. converter temp. [°C]	Target diameter [cm]	Max. metal temp. [°C]	Max. t-m stress in graphite [Pa]	Max. t-m stress in metal [Pa]	Max. inertial stress (10 Hz) [Pa]
1740	52	435	$2.62 \times 10^7$	$5 \times 10^6$	$3.5 \times 10^6$
Material	Max. t/m stress von Mises [Pa]	Max. t/m stress X-component [Pa]	Max. t/m stress Y-component [Pa]	Max. t/m stress Z-component [Pa]	Max. deformation [mm]
Graphite	$2.9 \times 10^7$	$2.87 \times 10^7$	$1.26 \times 10^7$	$4.12 \times 10^6$	0.7
Metal	$3.85 \times 10^7$	$2.71 \times 10^7$	$3.72 \times 10^7$	$3.84 \times 10^7$	1.09

#### 4.1.2. 200 kW Neutron Converter

Same measurements and calculations were made for 200 kW Neutron Converter, the virtual model for simulation was built as well, using ANSYS APDL code, as shown in Figure 4.12

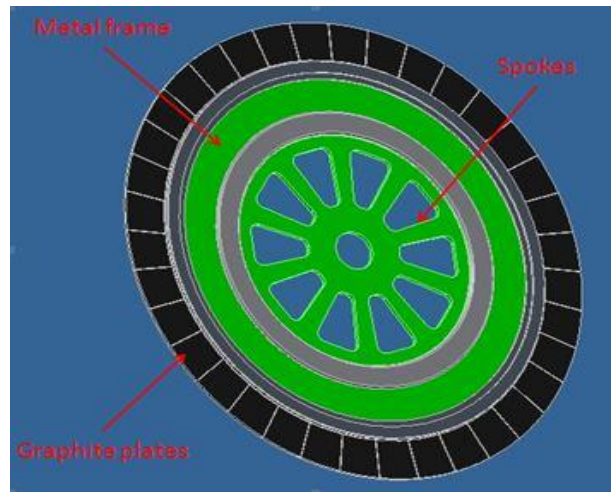


Figure 4.11. 200 kW Graphite Wheel Virtual Model

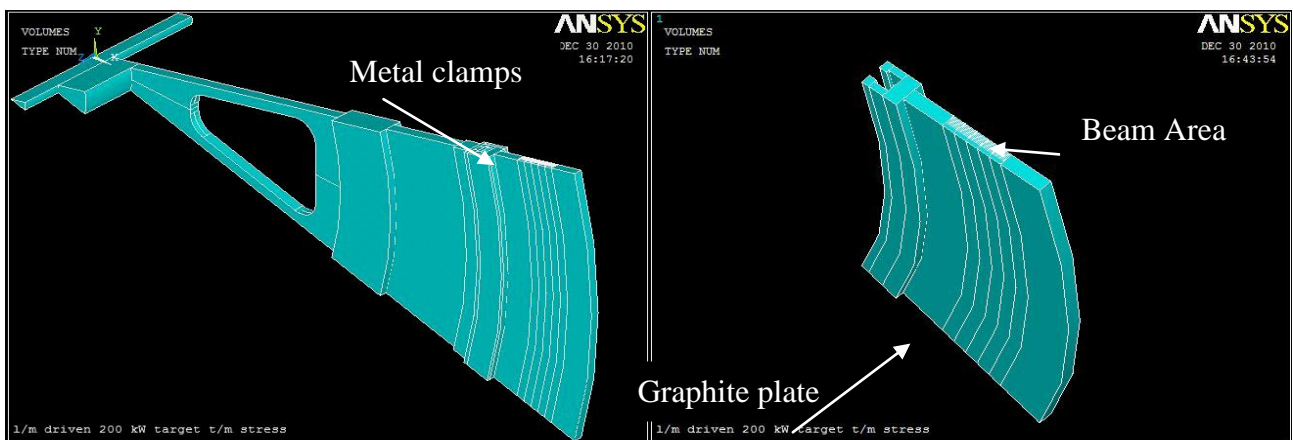


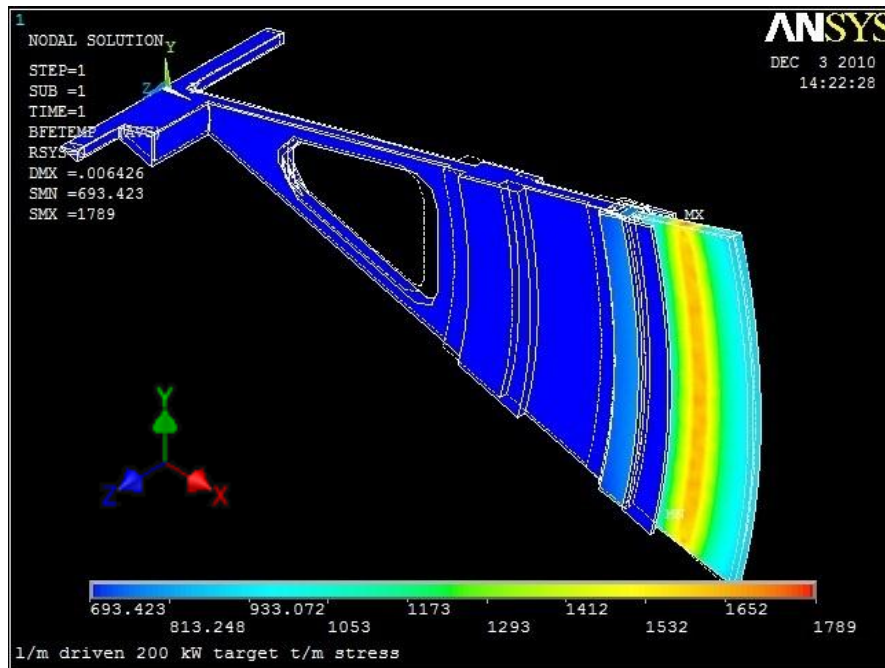
Figure 4.12. 200 kW Graphite Wheel Virtual Model

The power distribution according to the beam position and the number of particles over the graphite target is given in Table 4.3

**Table 4.3. 200 kW Gauss Beam Distribution. Number of Particles and Power**

Beam Position $\varphi$ (mm)	Particles Number	Power (W)
-21.3	385	802.79
-17.04	2367	4935.62
-12.78	7379	15386.54
-8.52	12822	26736.17
-4.26	17064	35581.5
0	20007	41718.18
4.26	16423	34244.9
8.52	11290	23541.68
12.78	6186	12898.92
17.04	1826	3807.57
21.3	166	346.13
42.6 mm	95915	200000

Although the beam power is higher in this case, its distribution is Gaussian as well so the temperature distribution in the graphite wheel is very similar to that obtain in the 50 kW neutron converter. Maximum value arises up to 1789 °C in the centre of the beam.

**Figure 4.13. 200 kW Graphite Wheel Temperature Distribution.**

Form Figure 4.14 to Figure 4.17 it can be observed the deformation results for the wheel and the metal support. As it was expected ,the behaviour of this converter is similar to the 50 kW graphite wheel, the maximum displacement is 0.75 mm through the X direction. The white dash line indicates the total equivalent deformation in the three directions as shown in Figure 4.17.

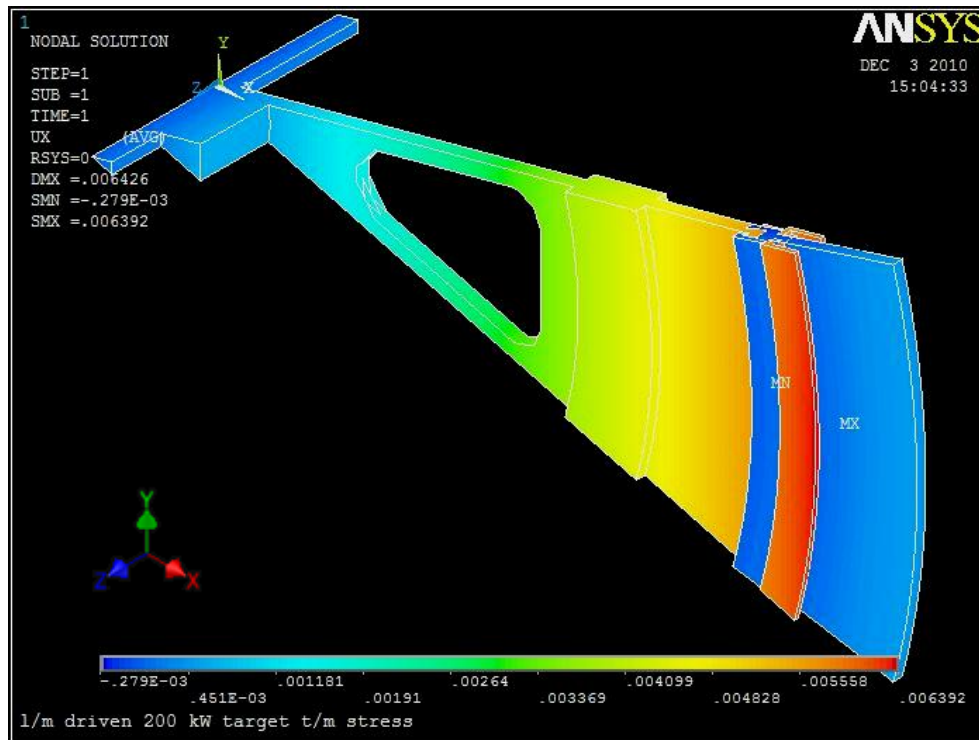


Figure 4.14. 200 kW Graphite Wheel . Deformation in X direction

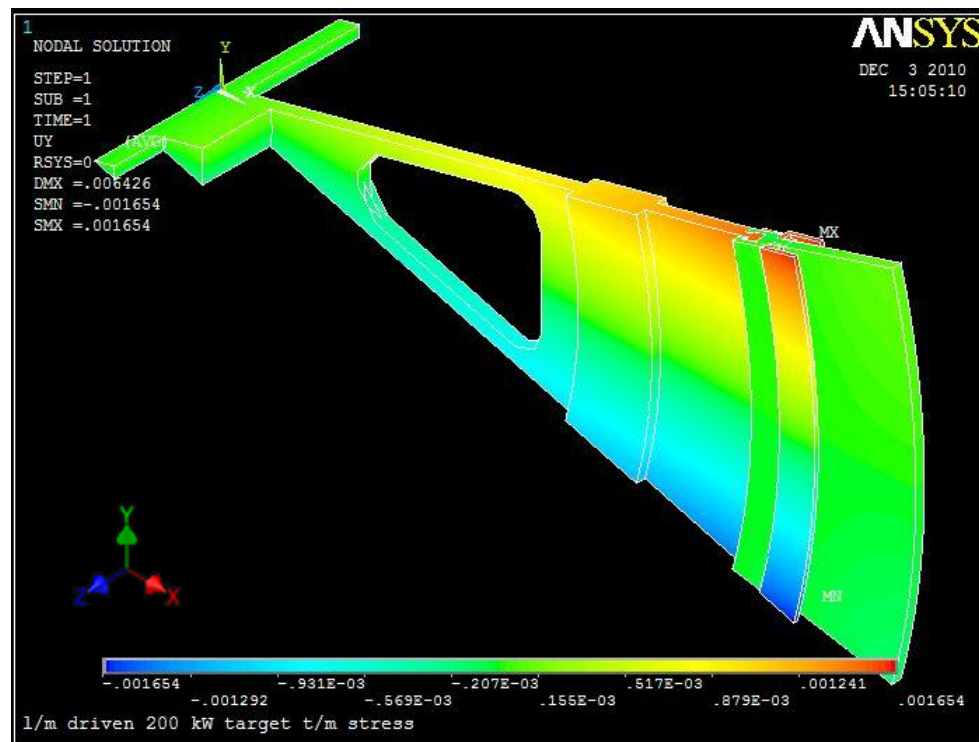


Figure 4.15. 200 kW Graphite Wheel . Deformation in Y direction

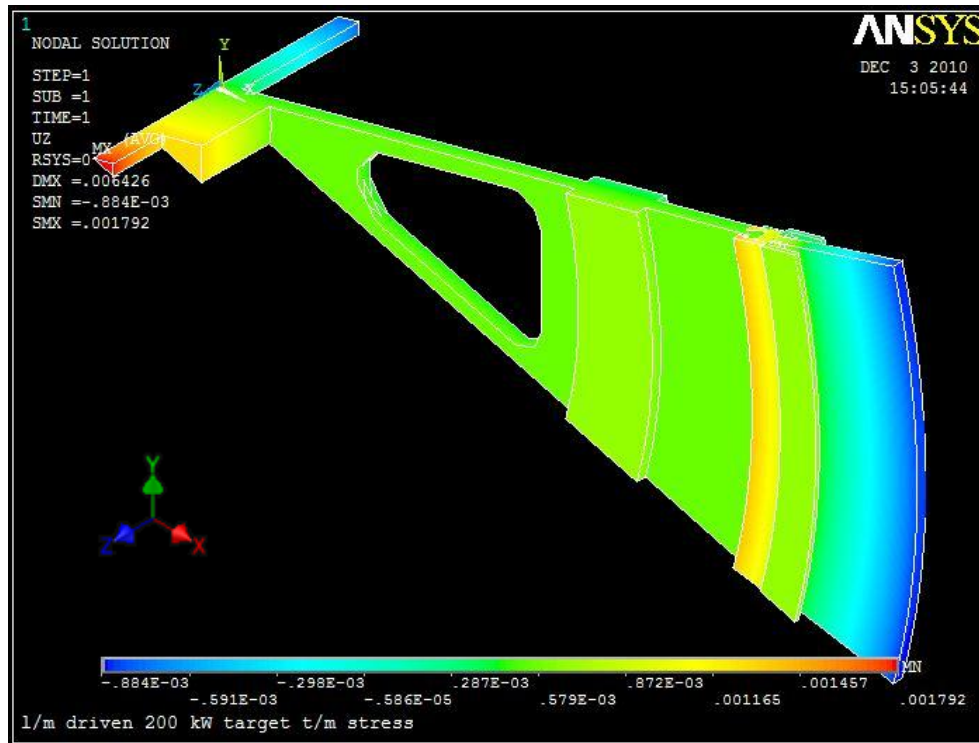


Figure 4.16. 200 kW Graphite Wheel . Deformation in Z direction

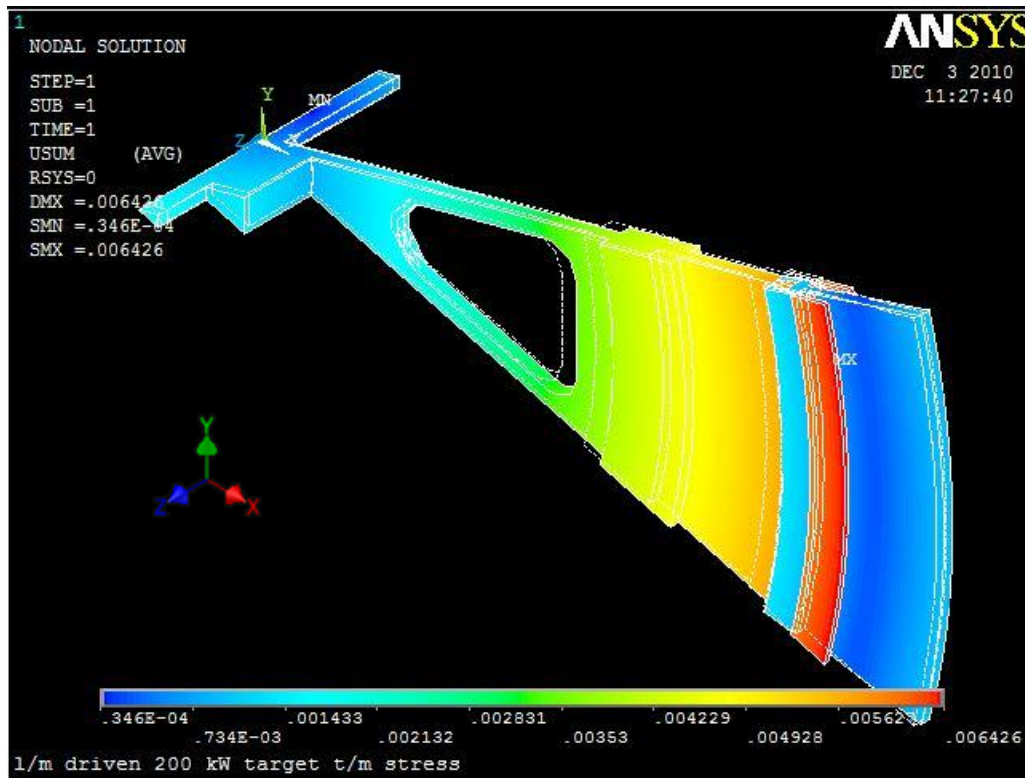


Figure 4.17. 200 kW Graphite Wheel .Total Deformation

Figure 4.18 shows the total equivalent stress for the neutron converter wheel, with a maximum value of 380 MPa, located in the zone with the highest concentration of power. Main results for the 50 kW neutron converter are summarized in Table 4.4.

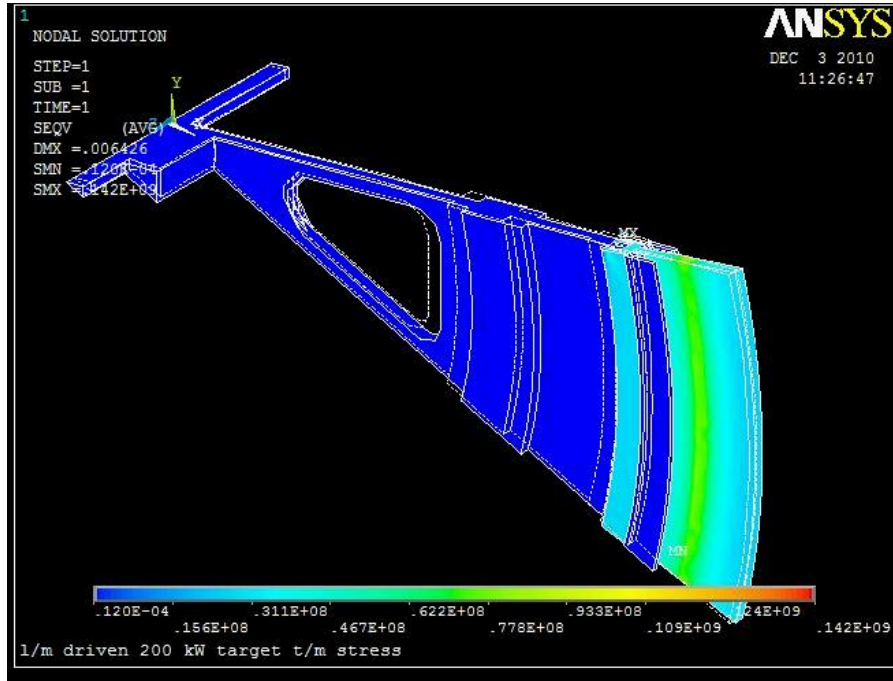


Figure 4.18 Graphite Wheel .Total Stress Von Mises

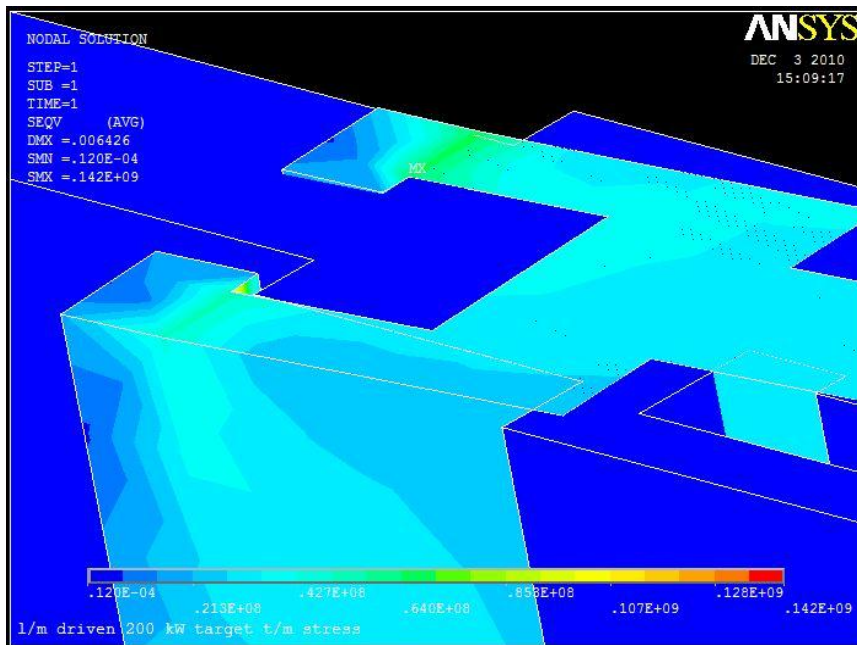


Figure 4.19. Graphite Wheel .Maximum Stress.

**Table 4.4. Summary of Maximum Values for Temperature and Stress for 200 kW Neutron Converter**

<b>Max. converter temp. [°C]</b>	<b>Target diameter [cm]</b>	<b>Max. metal temp. [°C]</b>	<b>Max. t-m stress in graphite [Pa]</b>	<b>Max. t-m stress in metal [Pa]</b>	<b>Max. inertial stress (10 Hz) [Pa]</b>
1790	120	570	$3.3 \times 10^7$	$2 \times 10^8$	$5 \times 10^7$
<b>Material</b>	<b>Max. t/m stress von Mises [Pa]</b>	<b>Max. t/m stress X-component [Pa]</b>	<b>Max. t/m stress Y-component [Pa]</b>	<b>Max. t/m stress Z-component [Pa]</b>	<b>Max. deformation [mm]</b>
Graphite	$3.16 \times 10^7$	$3.25 \times 10^7$	$2.03 \times 10^7$	$2.85 \times 10^6$	0.75
Metal	$3.8 \times 10^8$	$10^8$	$1.3 \times 10^8$	$1.45 \times 10^8$	6.4

### 4.1.3. Cooling Panels

The cooling panels are exactly the same for both cases, 50 and 200 kW Neutron converter; in case of necessity the graphite wheel and its support are replaced according to the power of the converter. Next figures (Figure 4.20 to Figure 4.23) show the assembly of the converter, cooling panel and delay window as well the solution of the simulation.

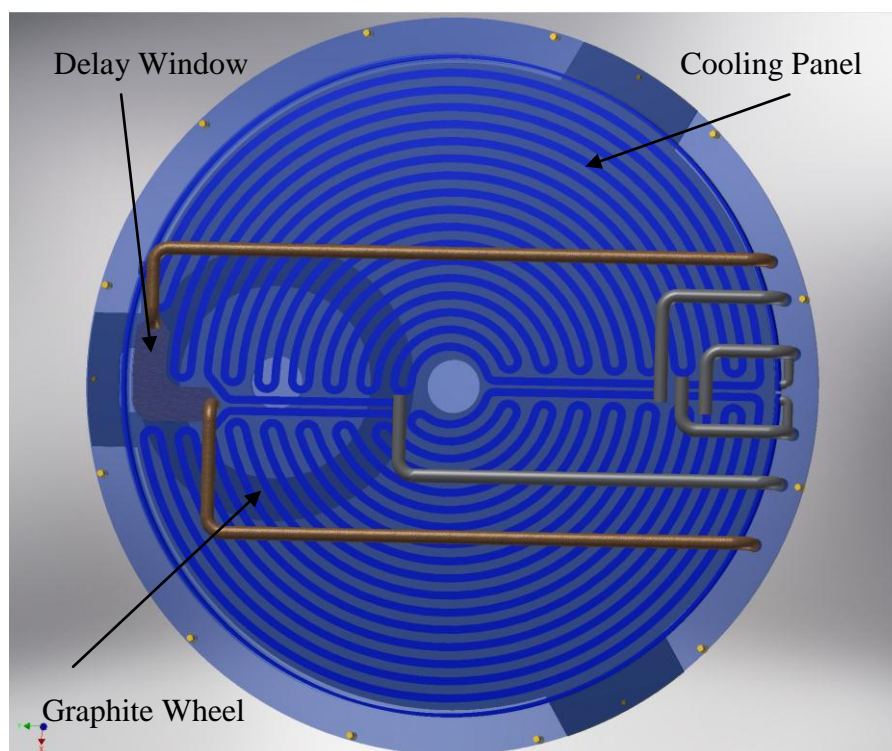


Figure 4.20. 50 kW Assembly Front View

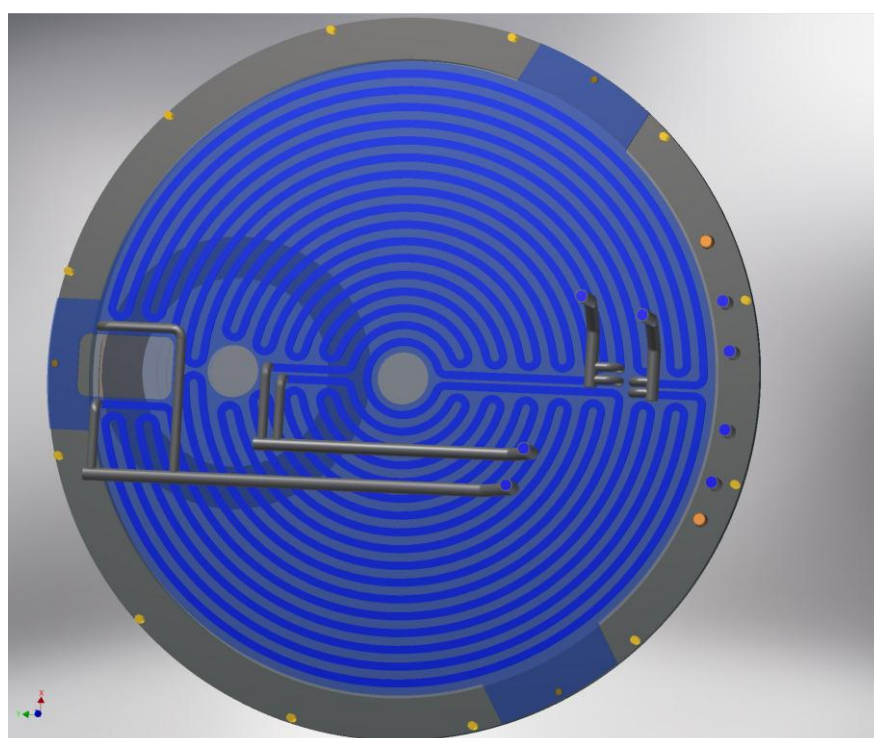
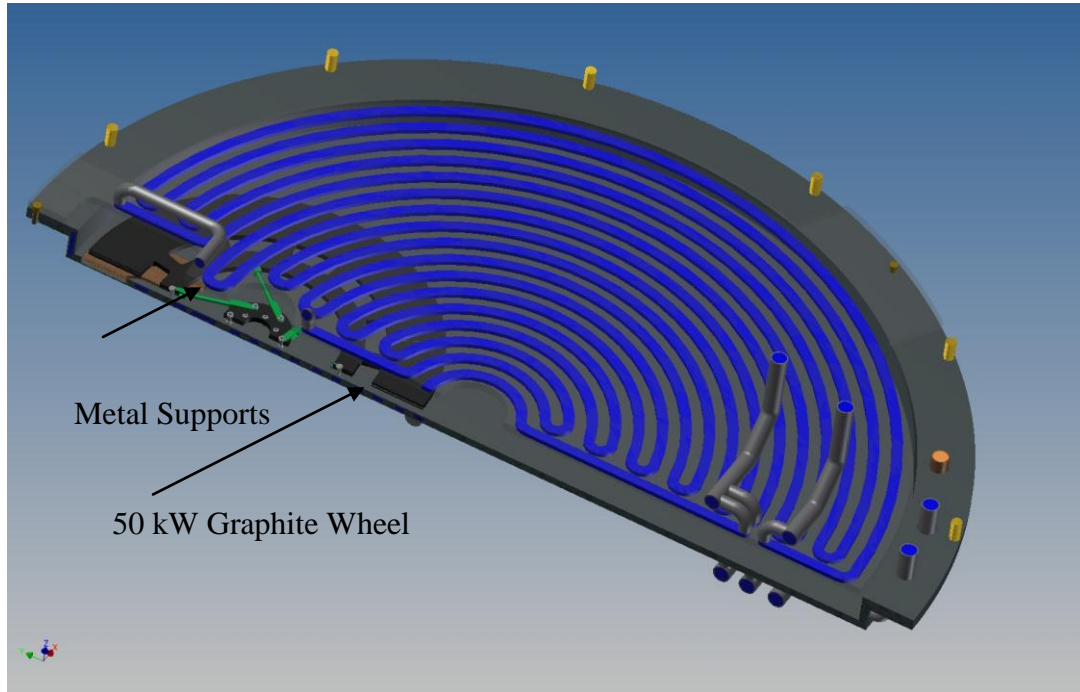
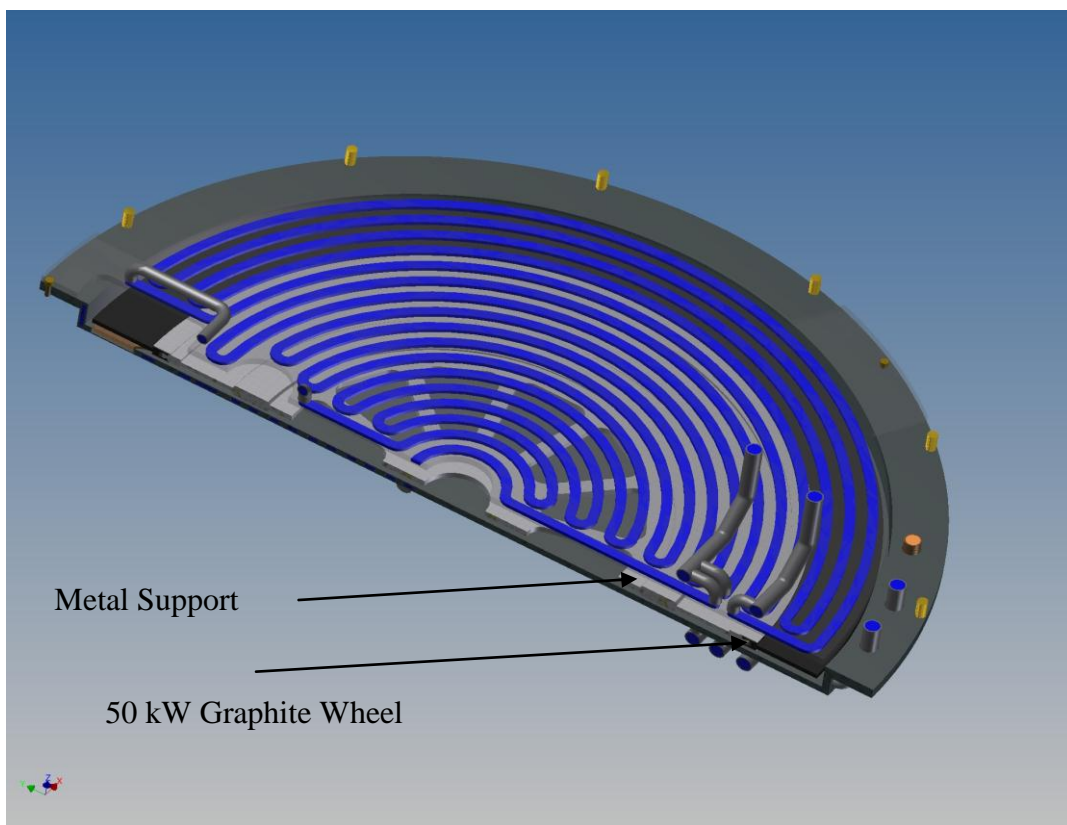


Figure 4.21. 50 kW Assembly Rear View

Figure 4.22 and Figure 4.23 show the half section of the 50 and 200 kW cooling panels assembly with their internal components, the arrangement of the water channels and the feeding water pipes for the heat exchange



**Figure 4.22. 50 kW Assembly Half Section**



**Figure 4.23. 200 kW Assembly Half Section**

#### 4.1.3.1 50 kW Cooling Panel

The temperature distribution was obtained after the CFX simulation; each component was treated separately in order to achieve a more precise range of results. Figure 4.24 shows the temperature in the delay window wall as influence of the liquid lead flowing through it; in the other hand Figure 4.25 shows the temperature distribution in the liquid lead.

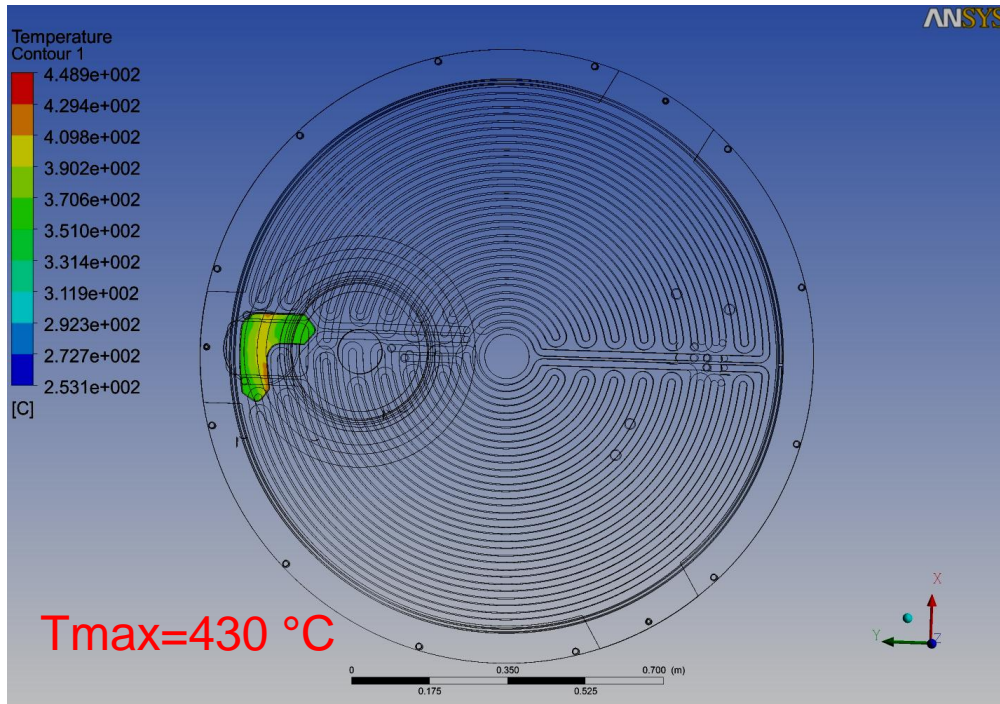


Figure 4.24. 50kW Metal Delay Window Temperature

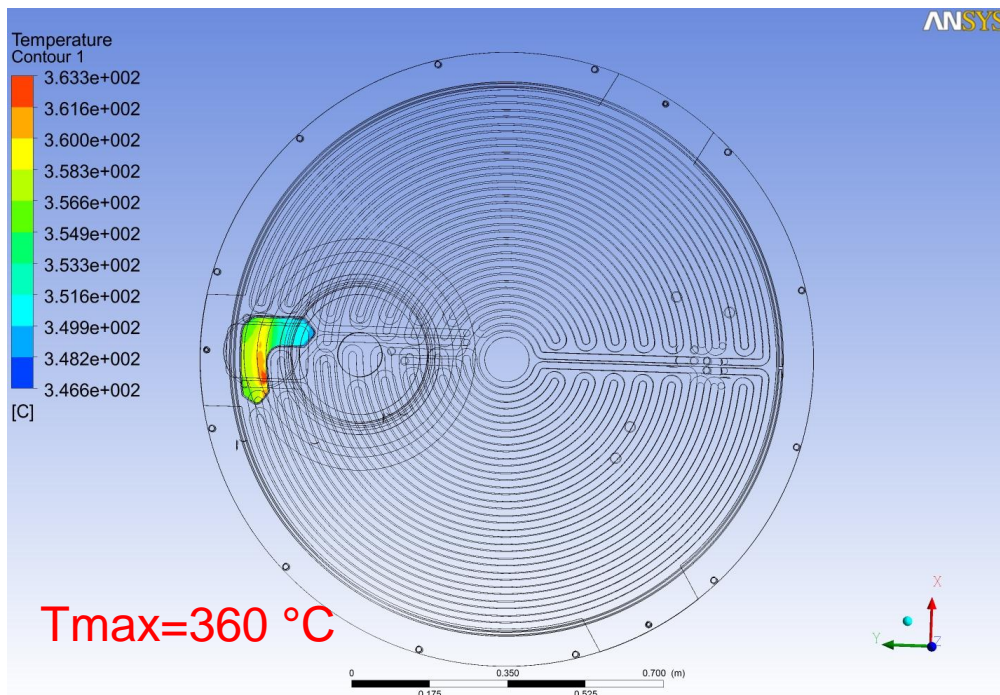


Figure 4.25. 50kW Liquid Lead Temperature

The temperature distribution on the rear part of the cooling panel is shown in Figure 4.26. The frontal plate temperature is indicated in Figure 4.27.

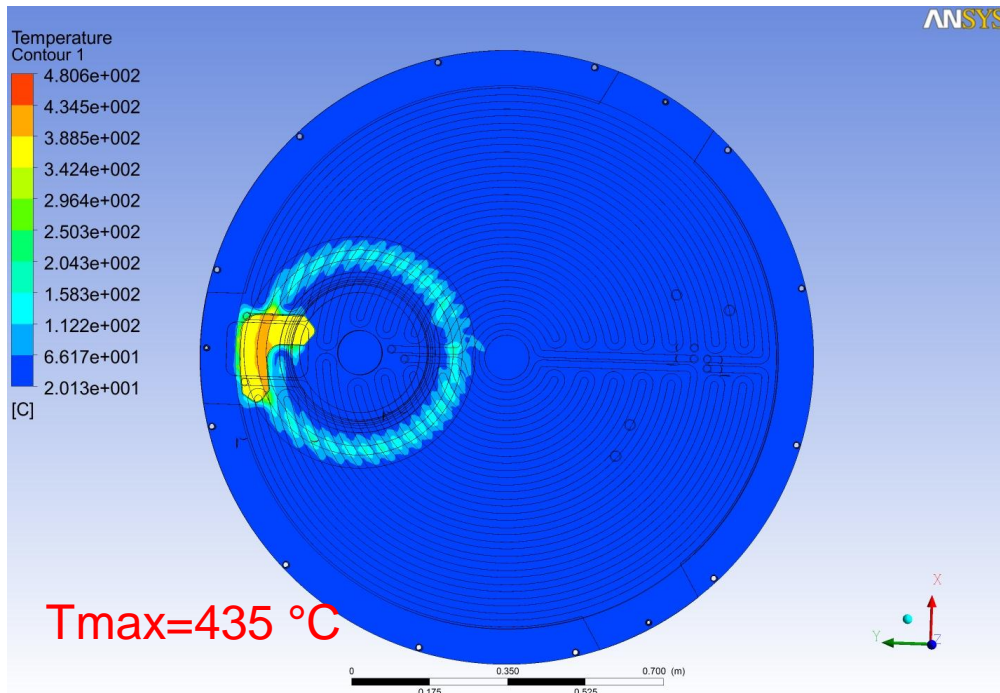


Figure 4.26. 50kW Rear Panel Temperature

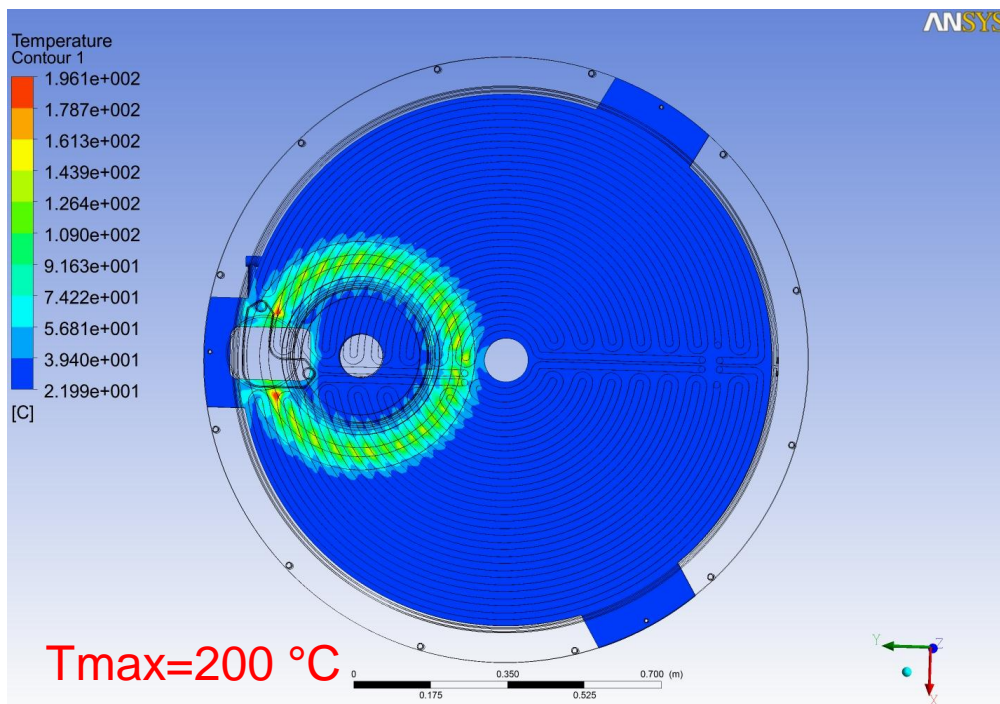


Figure 4.27. 50kW Front Panel Temperature

The CFX simulation for the cooling water gives the temperature solution for both circuits, rear and front, as shown in Figure 4.28 and Figure 4.29. From these results it can be observed that the highest values occur in the front side of the panel.

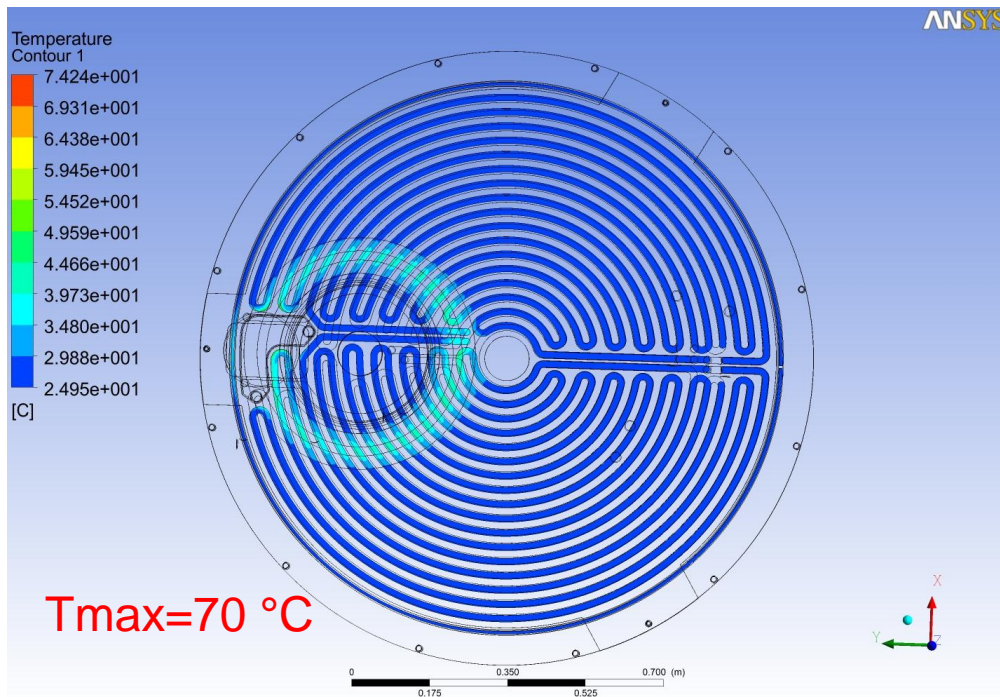


Figure 4.28. 50kW Rear Panel Water Temperature

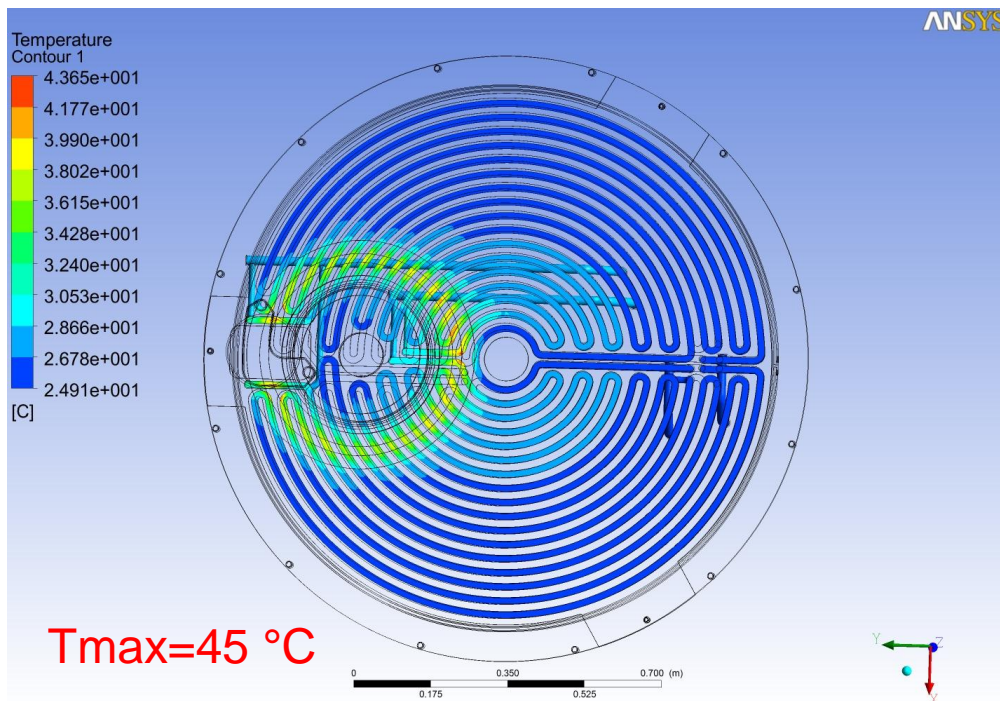


Figure 4.29. 50kW Front Panel Water Temperature

The total equivalent stress as a result of the static structural analysis is shown in Figure 4.30 and Figure 4.31. The maximum value is located in the rear part of the cooling panel and is within the limits of resistance of the steel properties.

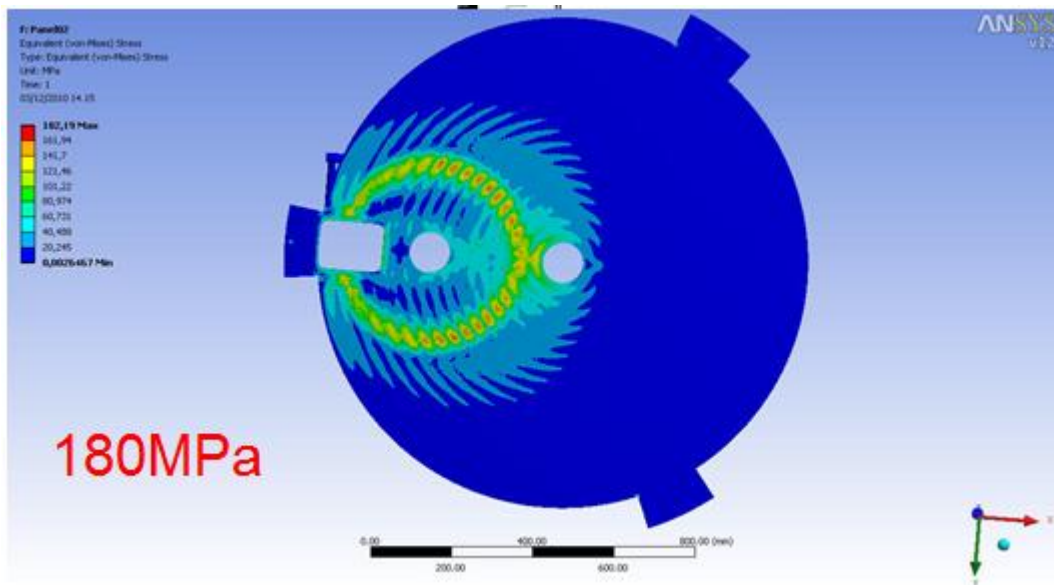


Figure 4.30.. 50kW Front Panel Stress

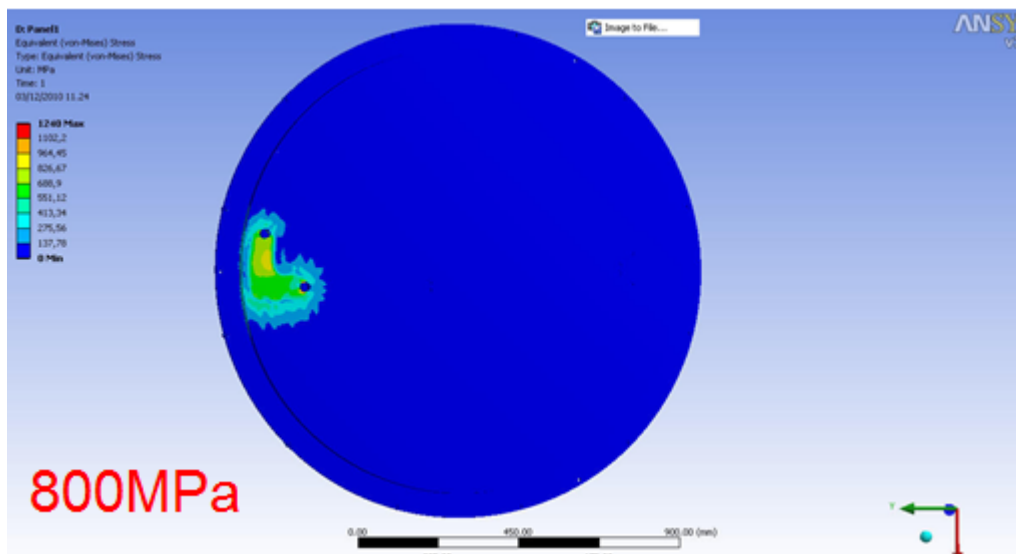


Figure 4.31. 50kW Rear Panel Stress

The total deformation results are given below in Figure 4.32 and Figure 4.33. As indicated, maximum displacements arise up to 0.6 and 1.17 mm in each plate of the cooling panels, in this regard the value is small enough to be considered acceptable according to the geometrical limitations.

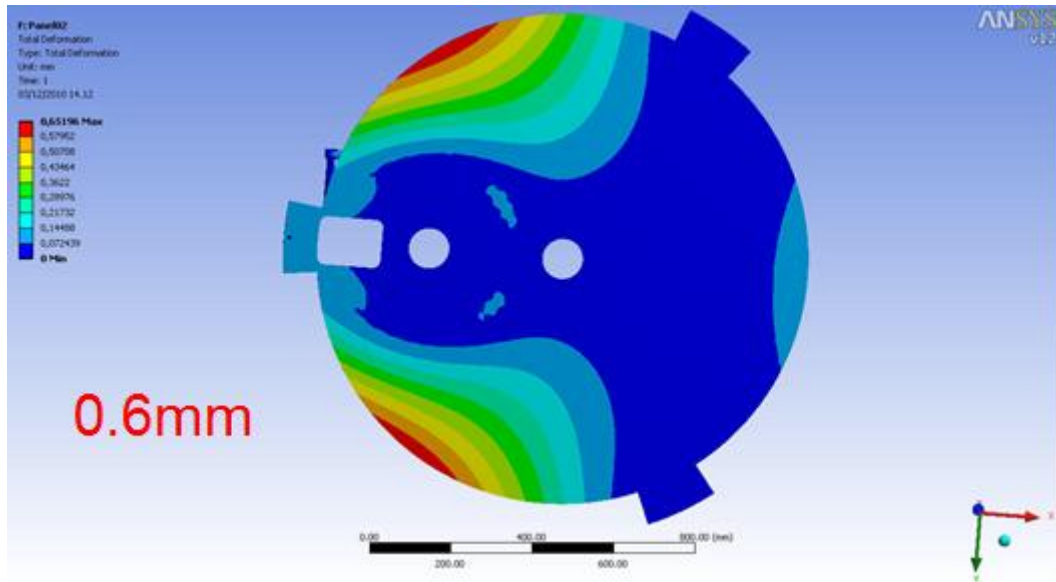


Figure 4.32. 50kW Front Panel Deformation

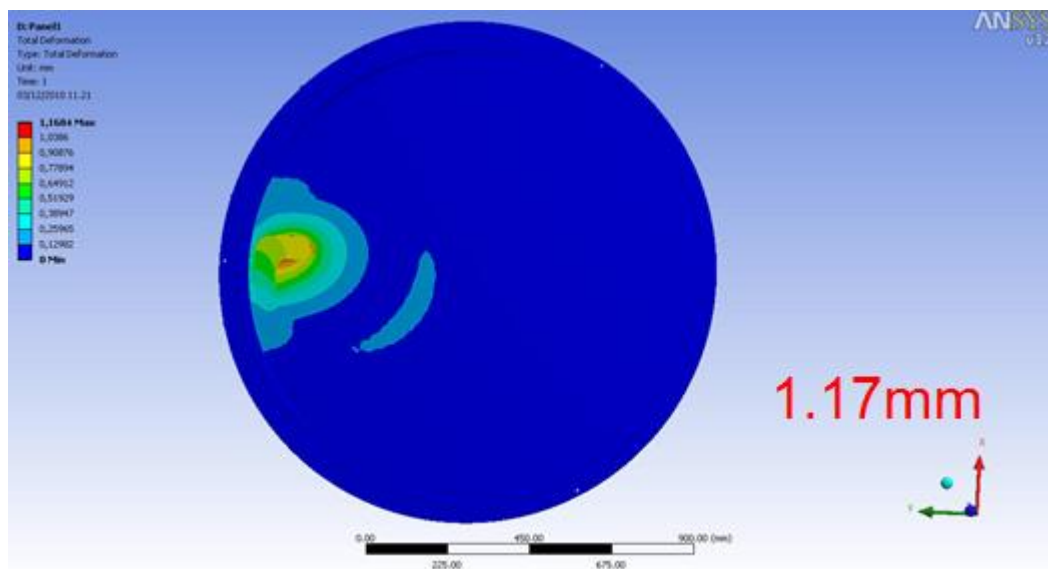


Figure 4.33. 50kW Rear Panel Deformation

#### 4.1.3.2 200 kW Cooling Panel

As in the previous case, the temperature distribution was obtained after the CFX simulation as well, Figure 4.34 shows the metal temperature in the delay window wall and Figure 4.35, the temperature of the liquid lead.

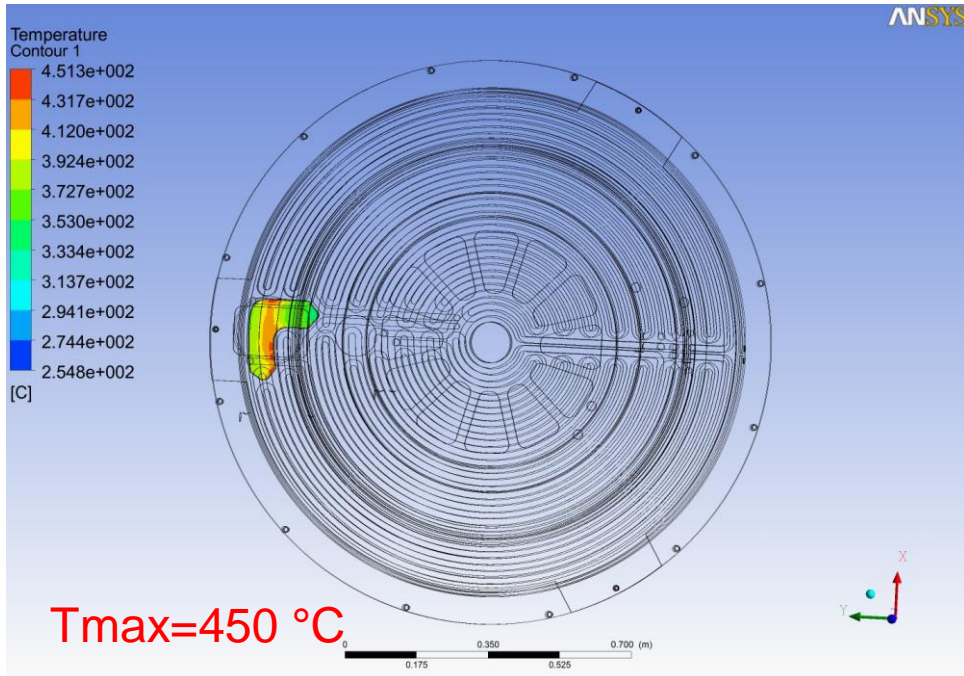


Figure 4.34. 200kW Metal Delay Window Temperature.

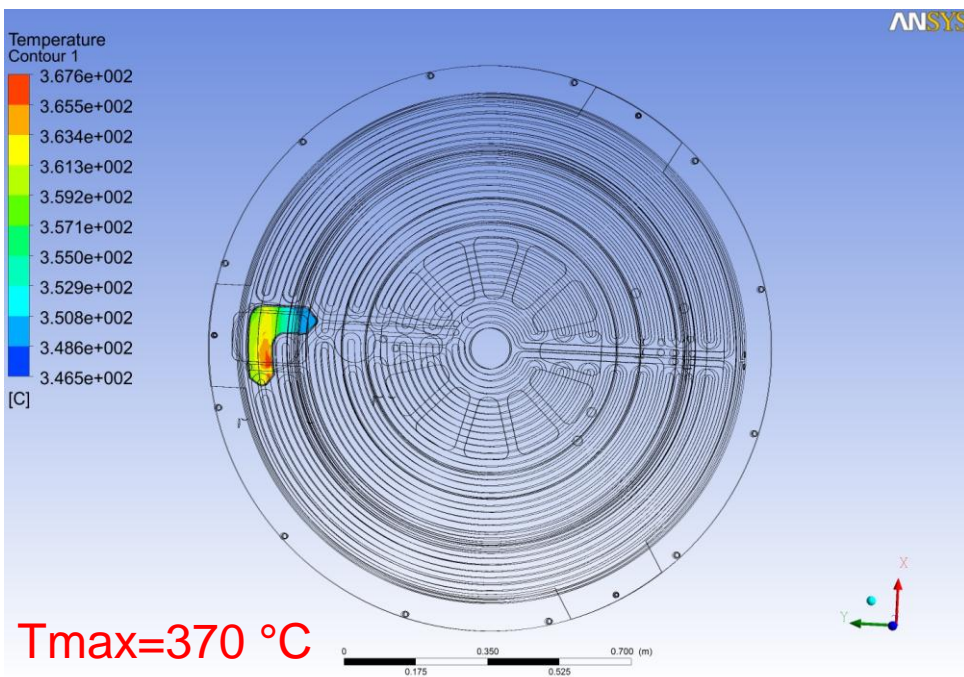


Figure 4.35. 200kW Liquid Lead Temperature.

Figure 4.36 and Figure 4.37 show the metal temperature distribution for the cooling panel, the highest value is located in that zone which is in contact with the delay window wall. The rear plate is colder since it is less close to the heat source.

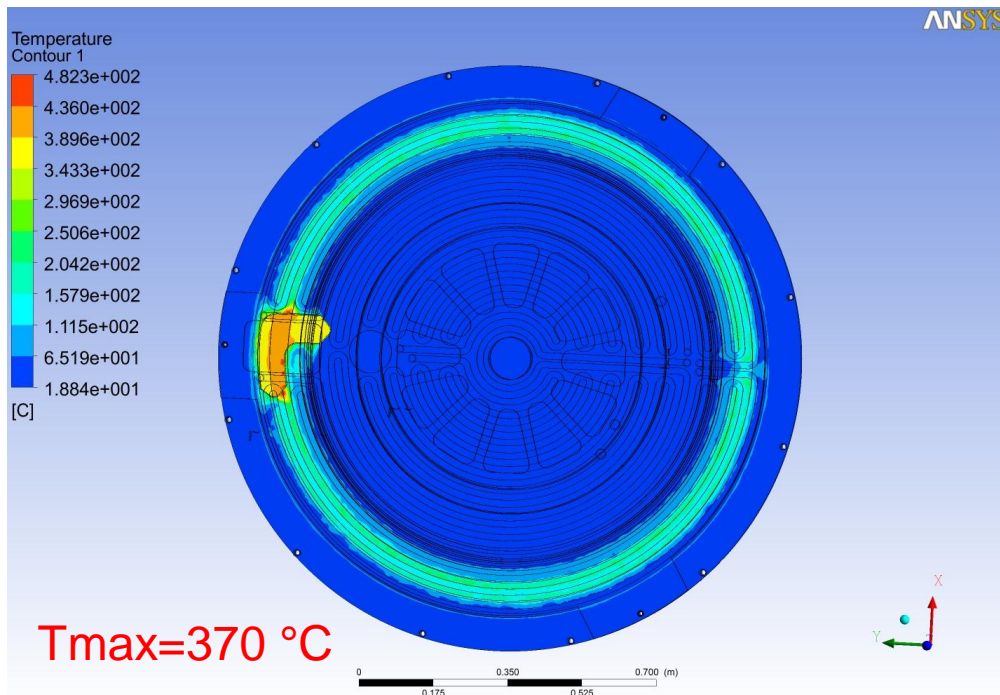


Figure 4.36.. 200kW Rear Panel Temperature

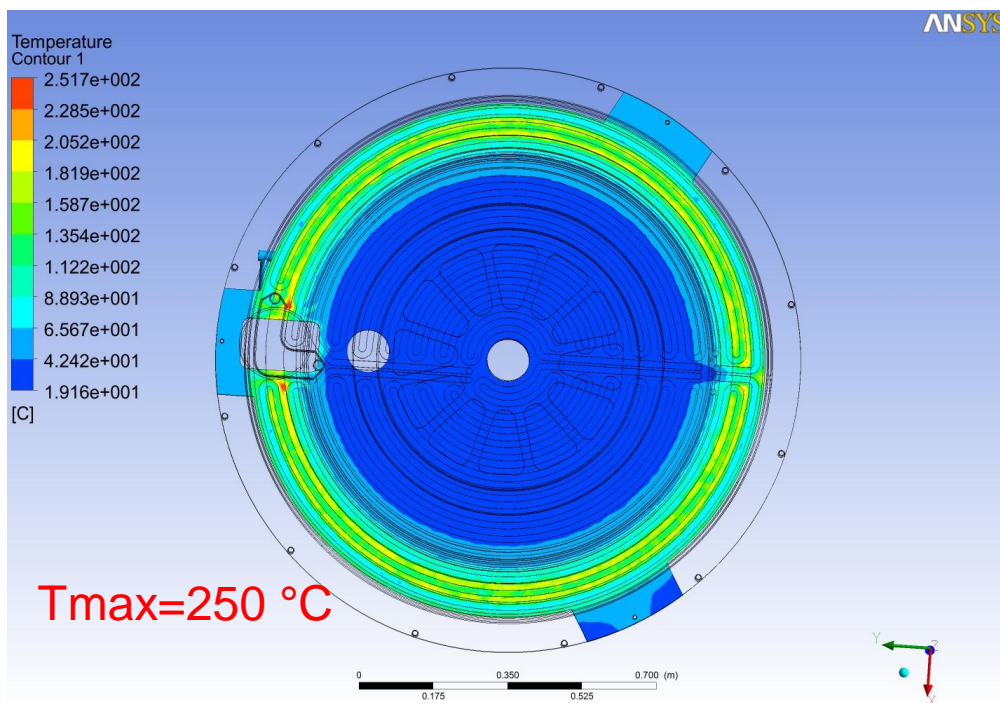


Figure 4.37. 200kW Front Panel Temperature

Figure 4.38 and Figure 4.39 give the temperature solution for the cooling water. The average is around 70°C, in this regard the result is thermodynamically consistent with the pressure parameters for water

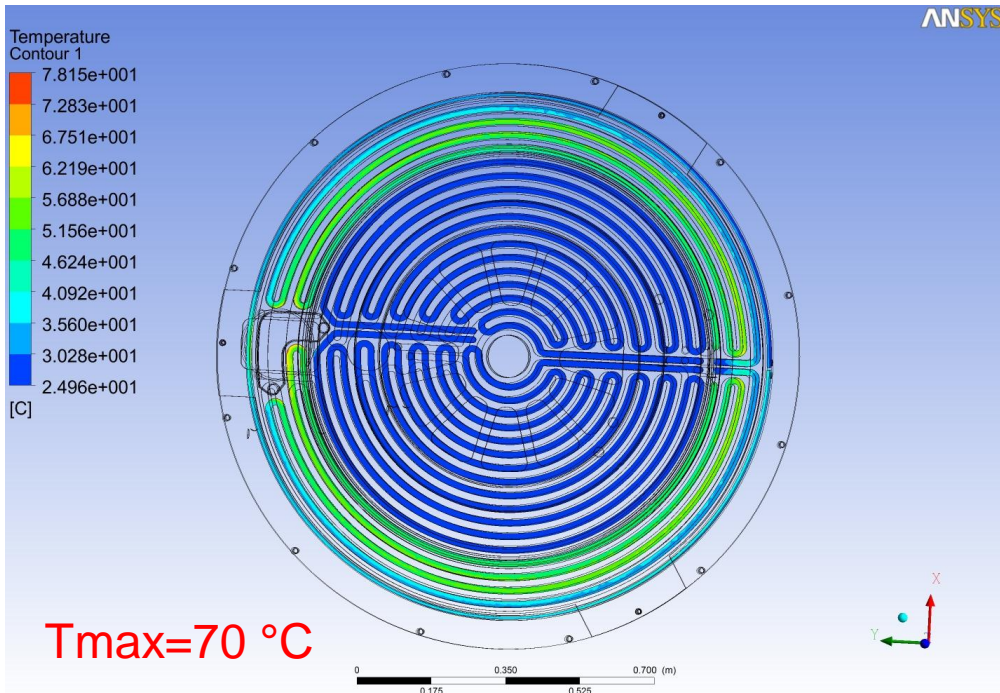


Figure 4.38. 200kW Rear Panel Water Temperature

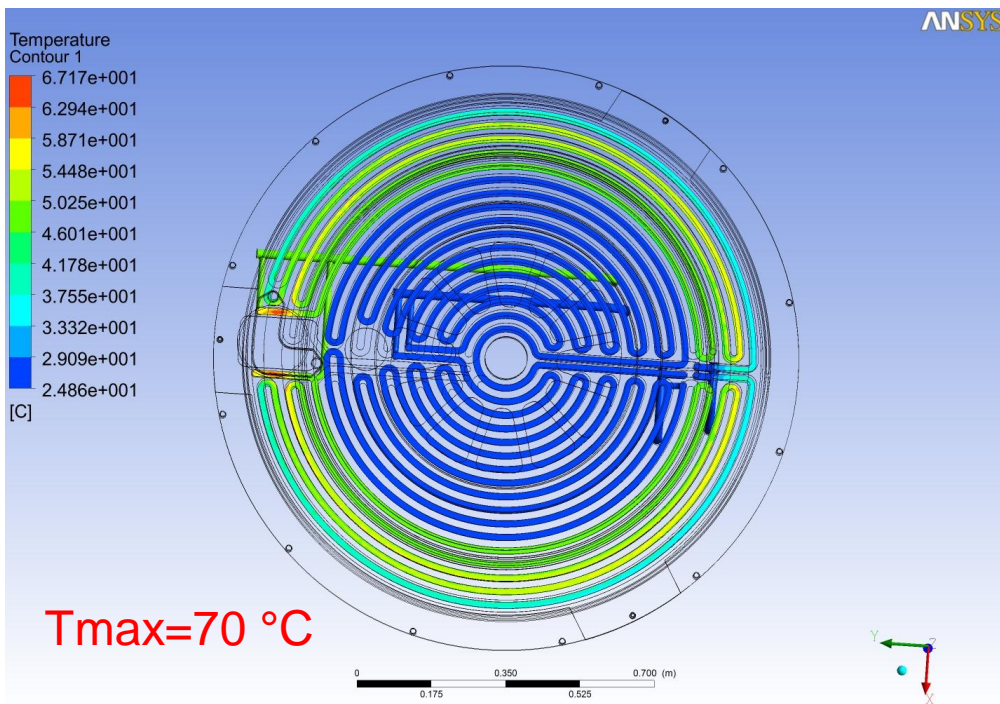


Figure 4.39. 200kW Rear Panel Water Temperature

Table 4.5 summarizes all the water parameters required to remove the necessary heat for the proper operation of the neutron converter: inlet and outlet temperature, pressure drops along the pipes, consumption and velocity of the fluid.

**Table 4.5. Water Parameters for Cooling Pannels**

Water parameters	Graphite Target	
	50 kW	200 kW
Water temperature inlet to all channels, °C	25	25
Maximum water temperature, channel #1, °C	52,1	68,5
channel #2, °C	57,8	76,9
channel #3, °C	43,8	31,4
channel #4, °C	48,1	35,7
channel #5, °C	74,2	78,2
channel #6, °C	41,6	67,2
channel #7, °C	43,6	28,5
Pressure drop over the water, channel #1, Pa	3,21 e+05	3,22 e+05
, channel #2, Pa	3,24 e+05	3,21 e+05
, channel #3, Pa	5,58 e+05	5,55 e+05
, channel #4, Pa	6,15 e+05	6,15 e+05
, channel #5, Pa	4,55 e+04	4,35 e+04
, channel #6, Pa	3,98 e+05	4,00 e+05
, channel #7, Pa	5,15 e+05	5,11 e+05
Water consumption channels l/s	0,53	0,53
Water velocity at the inlet, average value, m/s	3	3
Water velocity at the outlet, channel #1, average value, m/s	2,10	2,10
..... channel #2, average value, m/s	2,26	2,26
..... channel #3, average value, m/s	2,89	2,70
..... channel #4, average value, m/s	2,75	3
..... channel #5, average value, m/s	2,48	2,98
..... channel #6, average value, m/s	1,65	1,65
..... channel #7, average value, m/s	1,65	1,64

As expected, the total equivalent stress in the cooling panel has a similar behaviour to the 50 kW converter, being higher in the rear part of the metal due to the geometrical characteristics. Figure 4.40 and Figure 4.41 show these values about 330 and 800 MPa.

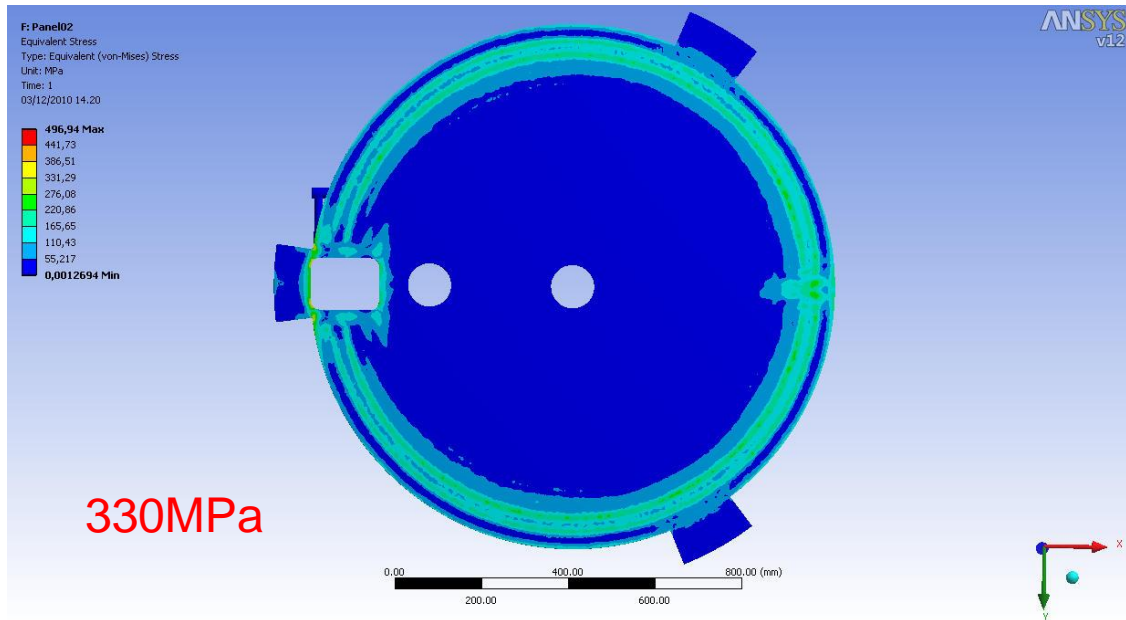


Figure 4.40. 200kW Front Panel Stress

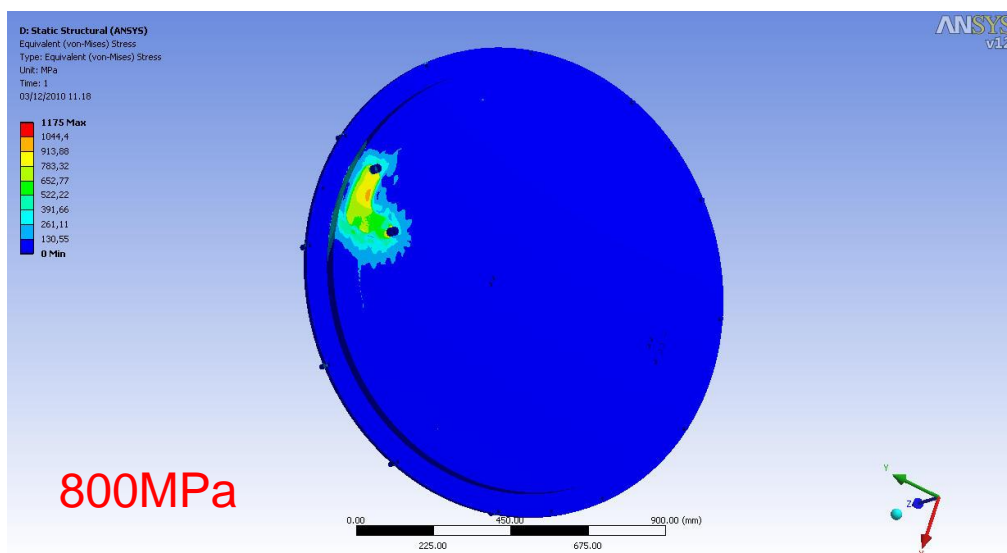


Figure 4.41. 200kW Rear Panel Stress

Figure 4.42 and Figure 4.43 show the total deformation in the metal plates. It can be considered as well, that the displacement is small enough according to the space conditions between the components of the cooling panels

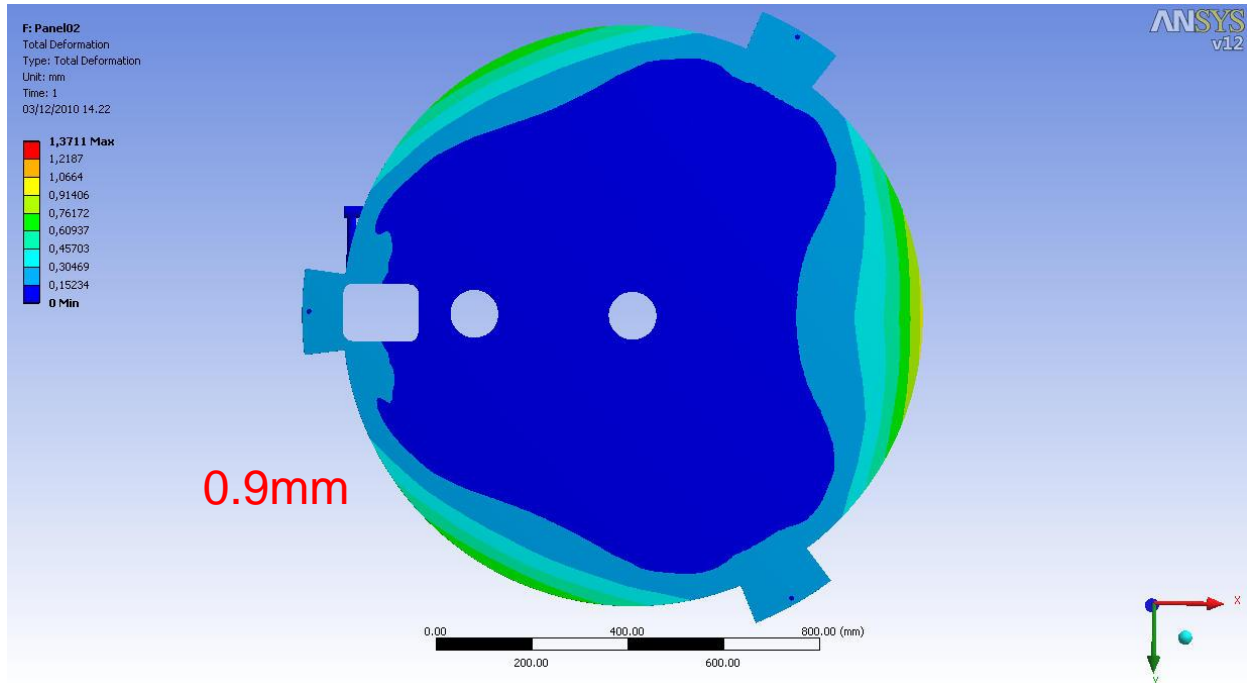


Figure 4.42. 200kW Front Panel Deformation

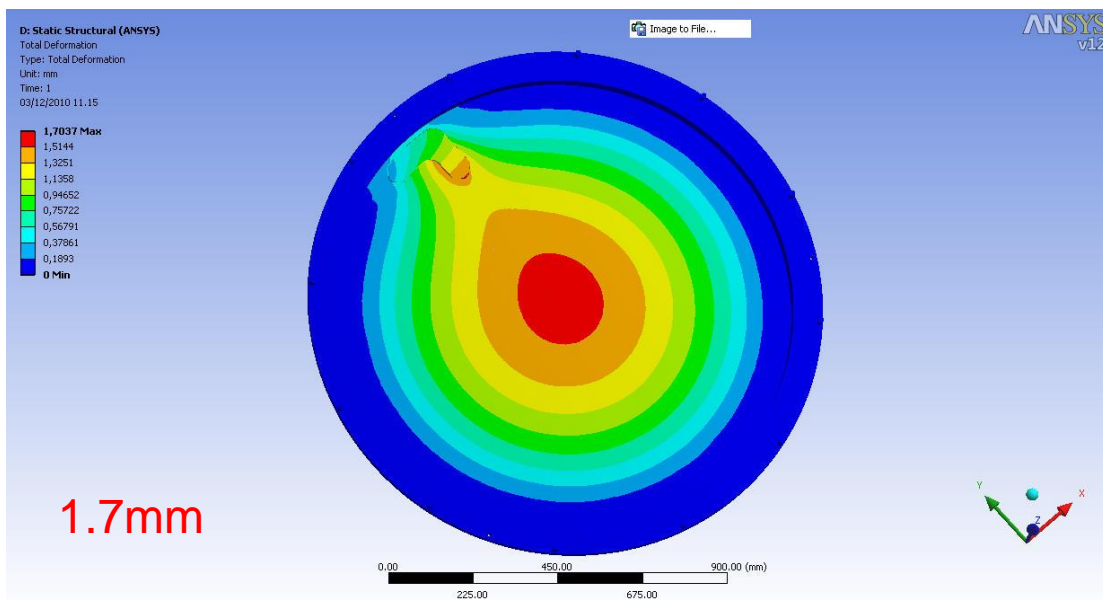


Figure 4.43. 200kW Rear Panel Deformation

#### 4.2. Lead Heating System

A liquid lead based assembly is part of a neutron production target prototype for SPIRAL2 facility. Initial conditions for the lead inside the pipes which feed the delay window are environment temperature @ 20°C. Rising up the lead temperature requires a warming system to reach its melting point. In this regard a pipe structure was designed according to the Figure 4.44.

The lead pipe is embraced with a second pipe with hot nitrogen flowing inside. The simulation is made on the basis of the ANSYS Workbench CFX platform.



Figure 4.44. Delay Window Arrangement

The lead initially at 20°C is warmed up by the nitrogen flow at 400°C, then flows through the pipe and inside the delay window. Cross section of the delay window is shown in Figure 4.45.

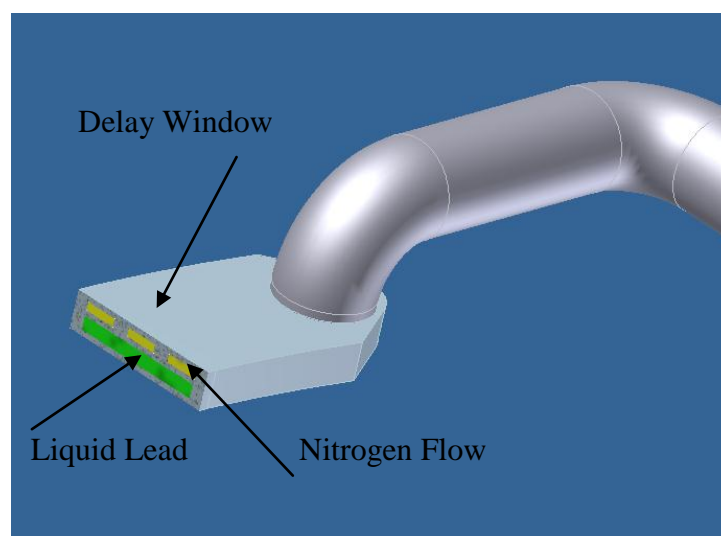
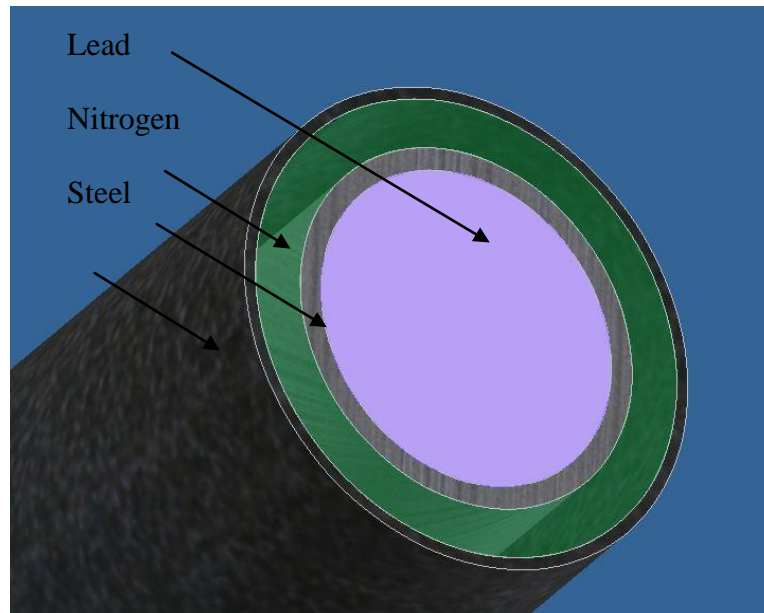


Figure 4.45. Delay Window Section



**Figure 4.46. Liquid Lead and Nitrogen Pipe Section**

After simulating the warming system for the lead in order to turn it liquid, the temperature distribution obtained is that shown on Figure 4.47 and Figure 4.48, where maximum value rises up to 375 °C and 400°C respectively . Table 4.6 show the parameters for the liquid lead in the delay window.

**Table 4.6. Lead Parameters for Delay Window**

Lead parameters	Graphite Target	
	50 kW	200 kW
Lead temperature inlet, °C	20	20
Maximum lead temperature, °C	375	375
Pressure drop over the lead, Pa	1,03 e+05	1,03 e+05
Lead consumption channel l/s	0.55	0.55
Lead velocity at the inlet, average value, m/s	1,5	1,5
Lead velocity at the outlet, average value, m/s	1,47	1,47

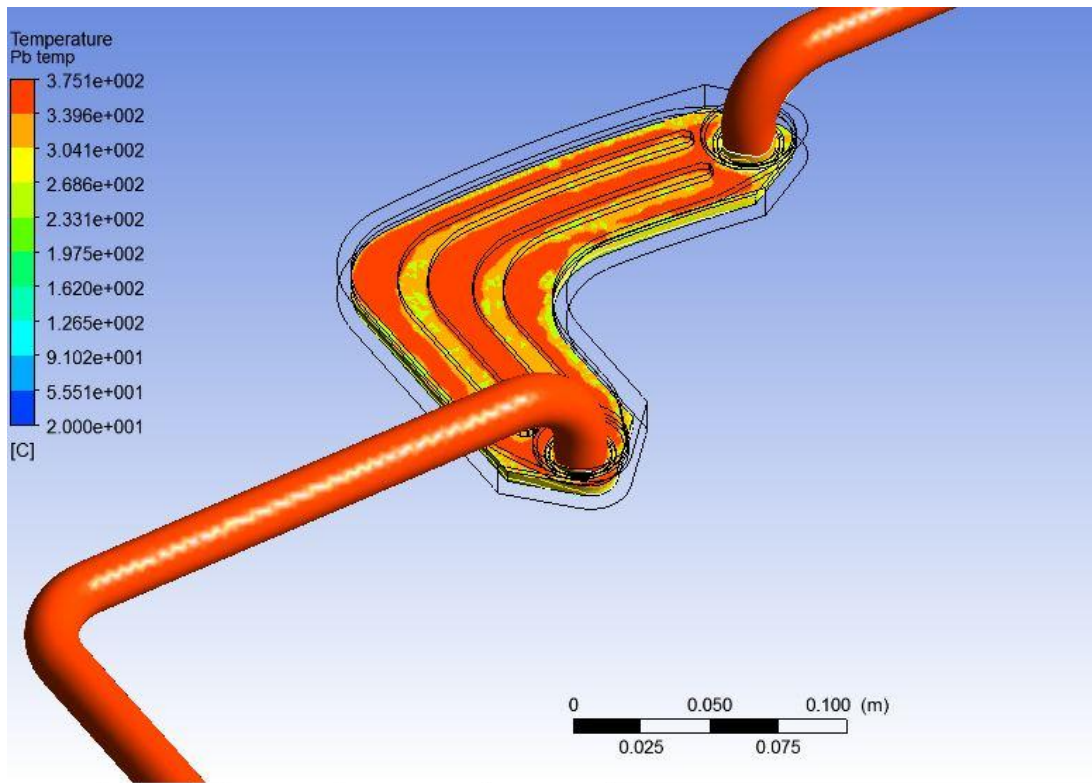


Figure 4.47. Liquid Lead Temperature Distribution

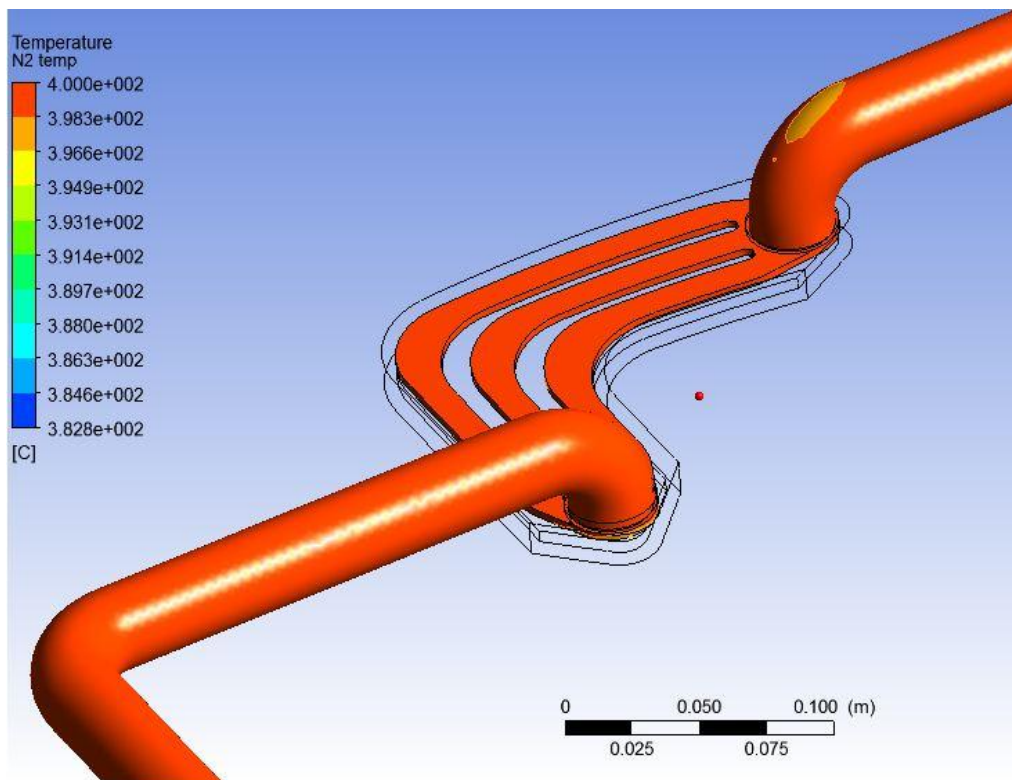


Figure 4.48. Nitrogen Temperature Distribution

## CHAPTER 5. TESTING AND MEASUREMENTS

### 5.1. Graphite's Evaporation Rate Test

In order to define which kind of graphite would be chosen for the converter, some tests and measurements have been performed since different values for evaporation rates are found in literature.

The experimental setup consists on a evaporation chamber in which the graphite sample is located under vacuum. The graphite sample is properly shaped and clamped in the special holder where is heated by direct electrical current passing through the sample. The active part of the sample has dimensions  $6 \times 3 \times 1 \text{ mm}^3$ . During the measurements the vacuum in the evaporation chamber is at the level of  $10^{-6}$  mbar. Two Quartz Crystal Monitors (QCM) measure the amount of graphite evaporated in function of the temperature.

Before measurement the samples have been cleaned at  $2300 \text{ }^\circ\text{C}$ , well above the experimental temperatures, to evaporates all the eventual impurities and residuals of machining.

To determine the evaporation rate the amount of graphite evaporated at each temperature has been measured by means of the two QCM detectors. The mass of graphite evaporated is obtained by measuring the frequency shift, respect its resonant frequency, of the QCM detectors, as defined by the Sauerbrey equation:

$$\Delta f = - \frac{2 f_0^2}{A \cdot \rho_q \cdot v_q} \cdot \Delta m$$

where:

- Quartz resonance frequency,  $f_0 = 10 \text{ MHz}$
- Quartz surfaces,  $A = \pi r^2 = \pi d^2 / 4 = \pi (7.95 \text{ mm})^2 / 4 = 0.496 \text{ cm}^2$
- Quartz density,  $\rho_q = 2.648 \text{ g/cm}^3$
- Propagation velocity of the wave into the quartz,  $v_q = 3.336 \cdot 10^5 \text{ cm/s}$

The QCM measurement resolution is of  $0.01 \text{ Hz}$ , corresponding to  $2.2 \times 10^{-2} \text{ ng}$

---

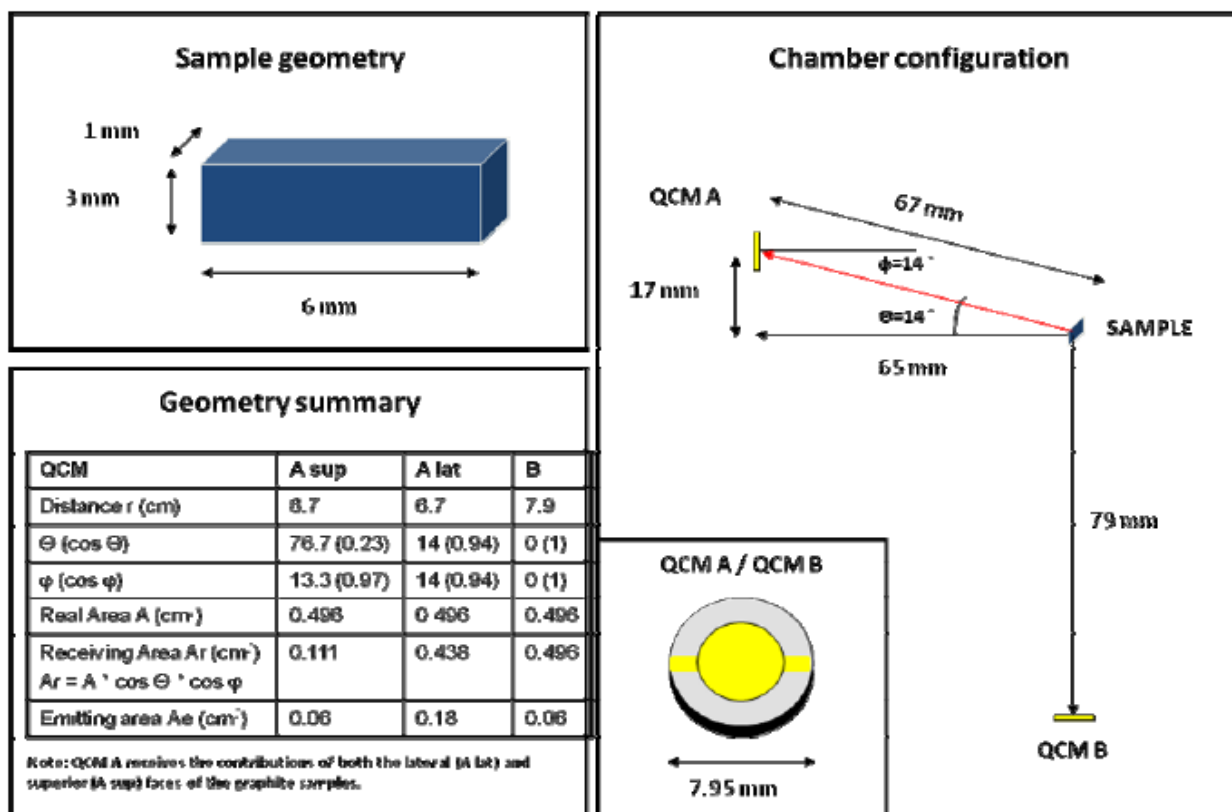


Figure 5.1. Sample geometry and detectors positioning

Figure 5.1 shows the geometry and the detectors position. The results of measurements are reported in Table 5.1, 5.2 and 5.3; averaged on detectors QCMA and QCMB. Tables shown the measured QCM frequency shift, the received graphite mass on the detector surface and the graphite evaporation rate calculated by the evaporation model of Ref. 1&2, in function of the sample temperature. The evaporation rates of the different graphites are summarized in Figure 5.2 and Figure 5.3, while—Figure 5.4 shows the comparison of evaporation rates for different commercial graphites.

Table 5.1. Main parameters of graphites used for the measurements

CARBON LORRAIN (1116 PT)		POCO AF5 (ZFX-5Q)				MPG8		
Grade	2318	Apparent Density (g/cm <sup>3</sup> )	1.78	Modulus of Elasticity (N/mm <sup>2</sup> )	14500	Property	Dir.	Value
Density (g/cm <sup>3</sup> )	1.86	Particle Size (µm)	1	Tensile Strain to Failure (%)	78	Density (g/cm <sup>3</sup> )		1.85
Grain size (µm)	5	Pore Size (µm)	0.3	Hardness (SSH)	86	Tensile Strength (MPa)	1	2*
Porosity (% volume)	6	Total Porosity (% volume)	20	Electrical Resistivity (µΩcm)	1950	Tensile Strength (MPa)	2	23
FS (MPa)	78	Open porosity (% of total)	80	Coefficient of Thermal Expansion (µm/m °C)	8,1	Tensile Modulus (MPa)	1	10
CTE (10 <sup>-6</sup> °C <sup>-1</sup> )	5.7	Compressive Strength (N/mm <sup>2</sup> )	195	Thermal conductivity (W/m°C)	70	Ultimate Compressive Strength (MPa)	1	80
Resistivity (µΩcm)	1600	Flexural Strength (N/mm <sup>2</sup> )	115	Oxidation threshold (°C)	450	Ultimate Bending Strength (MPa)		35
Thermal Conductivity (W/m°C)	80	Tensile Strength (N/mm <sup>2</sup> )	90			Thermal Conductivity (W/m°C)	-	95
Shore Hardness	80					CTE (1 °C)	1	5,3 x 10 <sup>-6</sup>
Standard Max. Size (mm)	308x 308x 915					Electrical Resistivity (mΩcm)	-	18
						Ash Content, %	-	0.02

Table 5.2. Measured QCM frequency shift, the received graphite mass on the detector surface and the graphite evaporation rate for the MPG8 graphite, in function of the sample temperature.

Deposition Temperature & Time	Δf QCM [Hz]	Received Mass M <sub>r</sub> [ng]	Evaporation Rate [kg/m <sup>2</sup> s]	Evaporation Rate [mm/month]
T = 2200 °C t = 1800 s	- 25.16	55.17	1.03x10 <sup>-6</sup>	1.44
T = 2100 °C t = 1800 s	- 4.76	10.44	1.95x10 <sup>-7</sup>	0.27
T = 2000 °C t = 2700 s	- 0.71	1.56	1.94x10 <sup>-8</sup>	0.027
T = 1900 °C t = 3600 s	- 0.12	0.26	2.45x10 <sup>-9</sup>	0.0034
T = 1850 °C T = 14400 s	- 0.05	0.11	2.55x10 <sup>-10</sup>	0.00036

**Table 5.3. Measured QCM frequency shift, the received graphite mass on the detector surface and the graphite evaporation rate for the POCO AFS (ZFX-5Q) in function of the temperature**

Deposition Temperature & Time	$\Delta f$ QCM [Hz]	Received Mass $M_r$ [ng]	Evaporation Rate [kg/m <sup>2</sup> s]	Evaporation Rate [mm/month]
T = 2200 °C t = 1800 s	- 43.2	94.73	$1.76 \times 10^{-6}$	2.57
T = 2100 °C t = 1800 s	- 8.42	18.47	$3.44 \times 10^{-7}$	0.50
T = 2000 °C t = 2700 s	- 1.36	2.98	$3.7 \times 10^{-8}$	0.054
T = 1900 °C t = 3600 s	- 0.20	0.44	$4.08 \times 10^{-9}$	0.006

**Table 5.4. Measured QCM frequency shift, the received graphite mass on the detector surface and the graphite evaporation rate for the 1116PT Carbone Lorraine graphite, in function of the sample temperature**

Deposition Temperature & Time	$\Delta f$ QCM [Hz]	Received Mass $M_r$ [ng]	Evaporation Rate [kg/m <sup>2</sup> s]	Evaporation Rate [mm/month]
T = 2100 °C t = 1800 s	- 21.83	47.87	$8.92 \times 10^{-7}$	1.24
T = 2000 °C t = 2700 s	- 3.70	8.11	$1.0 \times 10^{-7}$	0.14
T = 1900 °C t = 3600 s	- 0.98	2.15	$2.0 \times 10^{-8}$	0.03

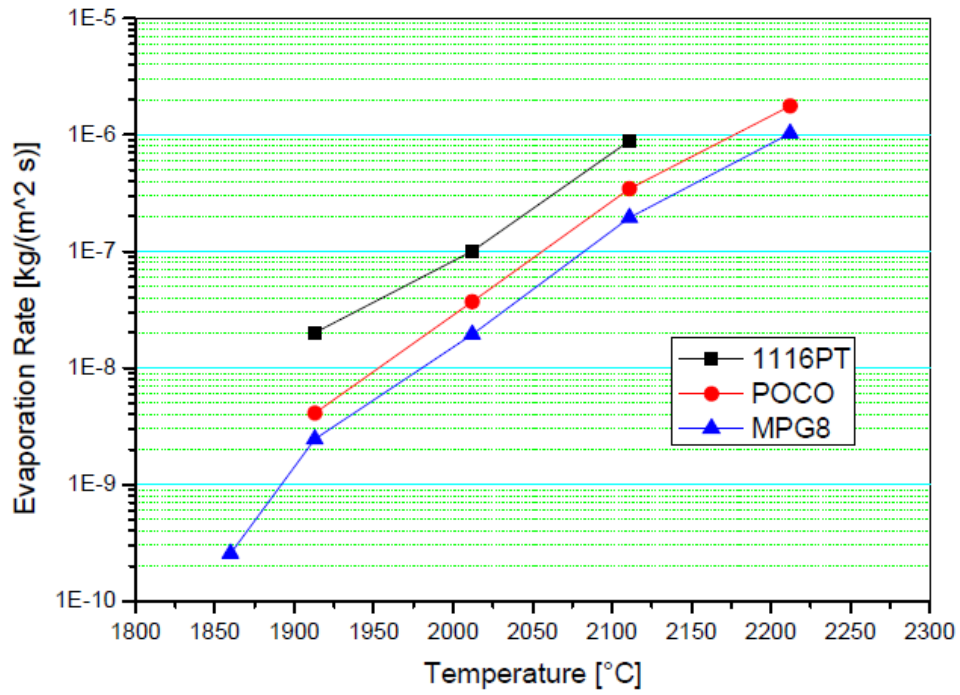


Figure 5.2. Graphite's evaporation rate in  $\text{kg}/\text{m}^3\text{s}$

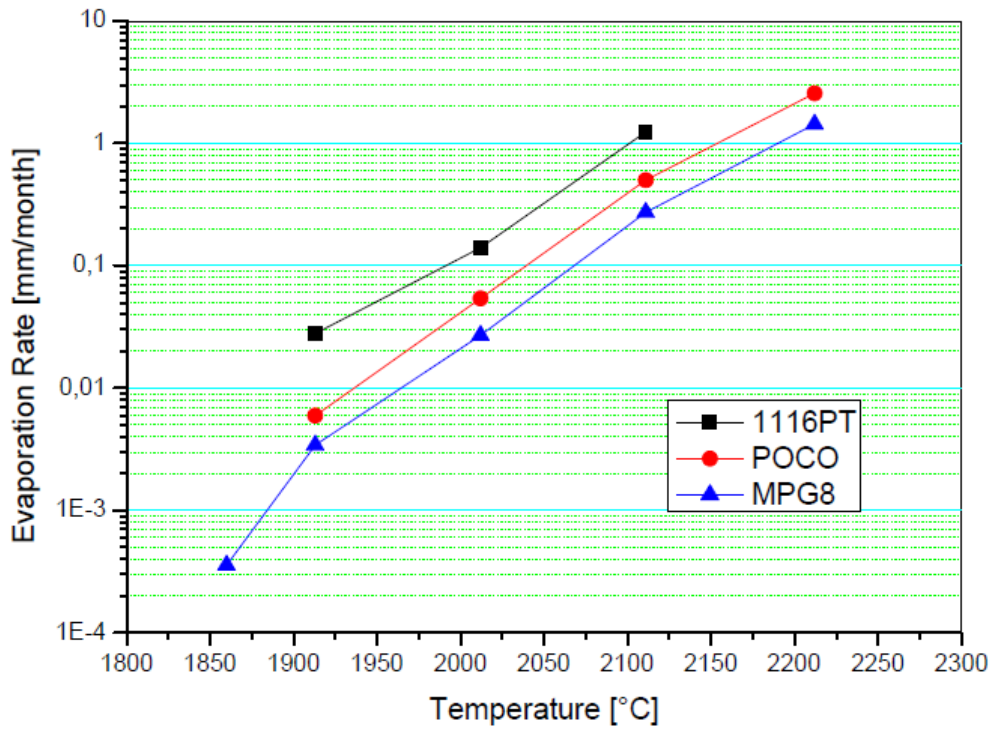


Figure 5.3. Graphite's evaporation rate in mm/month

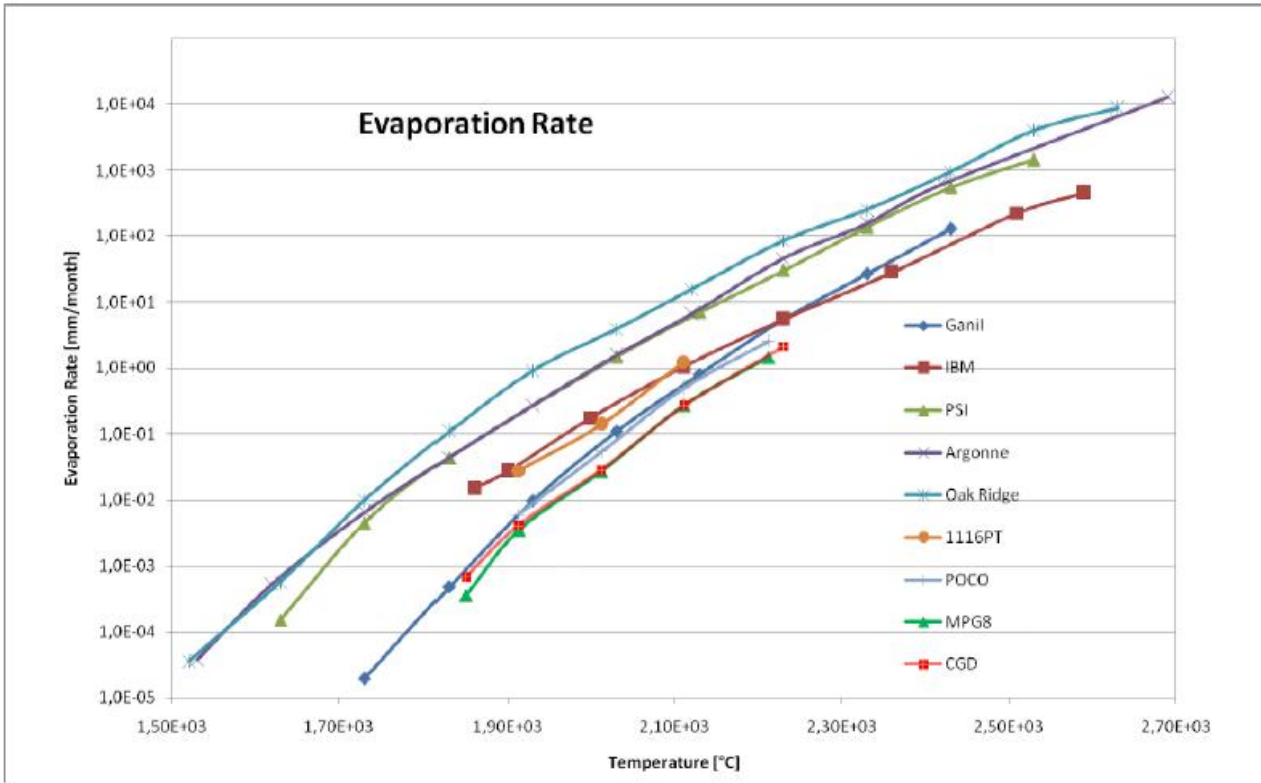


Figure 5.4 Graphite's evaporation for different commercial graphites

## 5.2. Delay Window Test

### 5.2.1. Experimental set-up

A dedicated test bench to investigate the performances of the “delay window” has been installed at the BINP (see Figure 5.5). The goal was to test the design parameters of the Delay Window in a “quasi” realistic SPIRAL2 configuration that guarantee good performances and a high safety level.

The set up is reproducing as close as possible the geometry of the Delay Window inside the “production module”, and in particular the distance between the surface of the Delay Window and the end of the vacuum chamber of the accelerator (350 mm) and its diameter (70 mm), as shown in the sketch of Figure 5.6.

The Delay Window was irradiated by an e-beam of 60 kW power and 1,7 mm minimum beam diameter. The beam size was determined disassembling the Delay Window after the experiment and measuring the hole produced by the beam with an optical microscope.

This prototype of Delay Window has been constructed rather smaller in comparison to that designed for SPIRAL2 but is reproducing very closely the active area interested by the 200 kW

deuteron beam. Figure 5.7 shows the Delay Window equipped of heating wires before the assembling of the test bench.

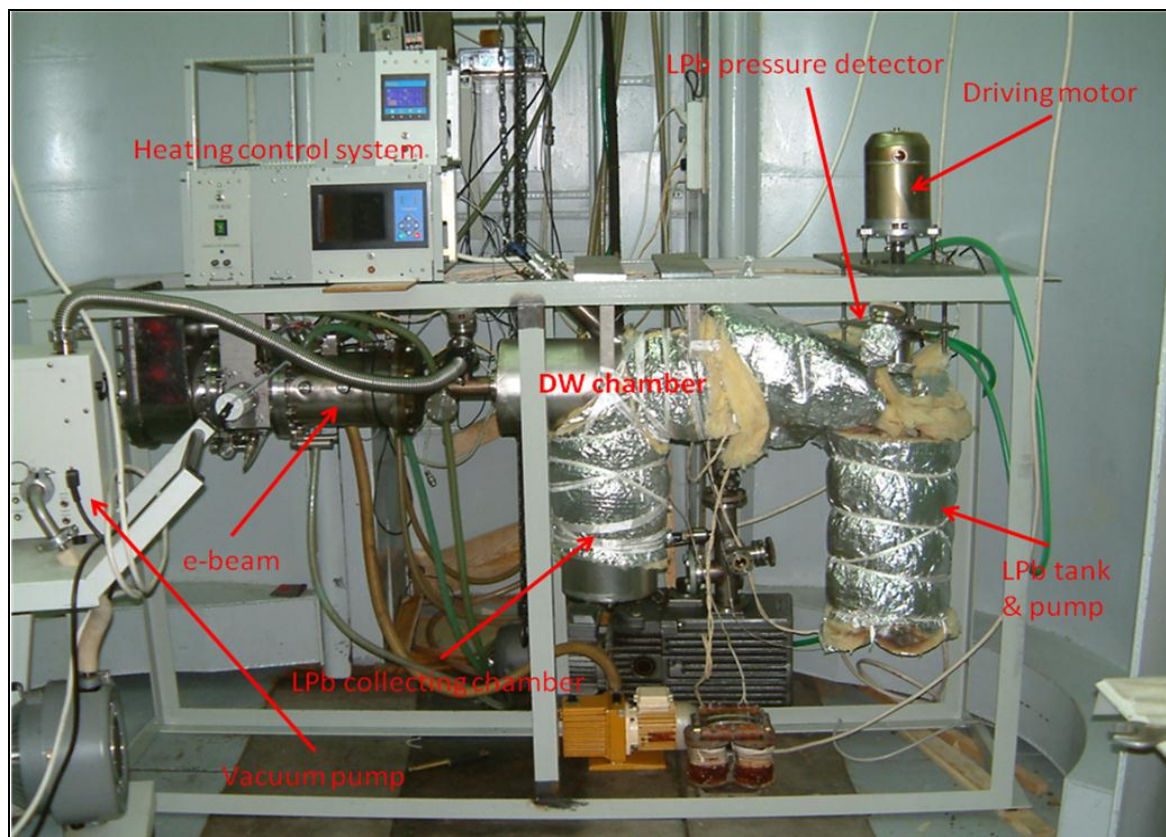


Figure 5.5. Set up for testing the "Delay Window".

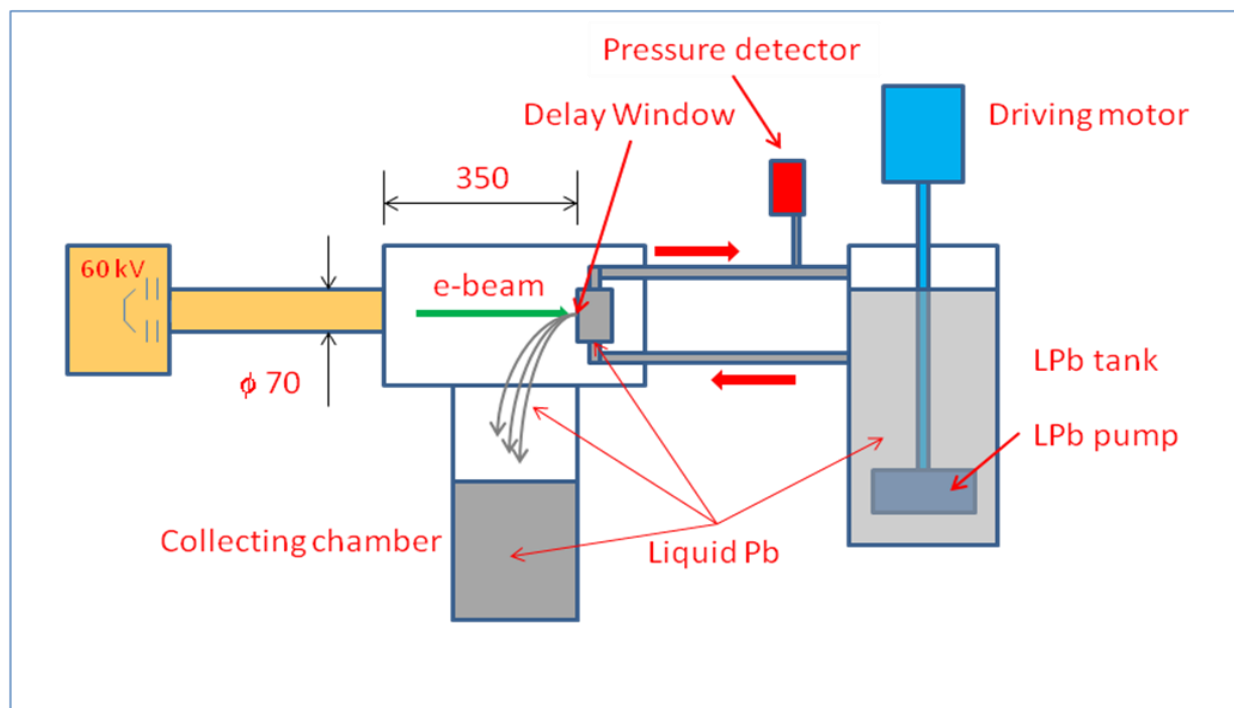


Figure 5.6. A sketch of the up for testing the "Delay Window".

The active area of the Delay Window is 70 mm wide, 40 mm height, 5 mm liquid lead thickness and 2 mm Stainless Steel wall thickness. Practically, the prototype differs from the real Delay Window only on its height that for constructing mechanical constraints will be about 600 mm. This will not influence the Delay Window performances because only the surface interacting with the beam (active area) is of practical interest.

The liquid lead tank was filled with about 10 liters of lead-tin alloy sufficient to guarantee, for this specific test, more than 5 minutes endurance of the full Delay Window system. The pump is immersed in the liquid lead and is drive by an electrical motor (48V, 25A, 4Nm). The entire system is operated at a temperature of 350°C.

The “collecting chamber” has the function to collect and recover the liquid lead coming out of the Delay Window after the melting of the first wall. This chamber is only heated on the upper part were the Delay Window is located, while the lower part is relatively cold and the liquid lead solidify, like in the “production module”.

The Delay Window and the “collecting chamber” are operated under vacuum ( $3,4 \times 10^{-5}$  mbar), as well as the electron beam device. In the other hand, the liquid lead circuit is operated in atmosphere. This aspect reproduce rather closely the situation at SPIRAL2 where the production module will be under vacuum and the liquid lead in a neutral atmosphere.

Three kinds of diagnostics are here considered and investigated. The first diagnostic is based on the variation of the vacuum level after the melting of the Delay Window. In fact, the liquid lead vapor will induce a fast rising of the vacuum level. The second one consist on measuring the absorbed current of the electrical motor driving the liquid lead. After the melting of the Delay Window the absorbed current as to decrease because its load is decreasing. The third diagnostic consists on measuring the pressure of the liquid lead returning back to tank. After the melting of the Delay Window the pressure in the return circuit will decrease considerably. A dedicated device has been developed and it is tested for the first time (see Figure 5.8).

---

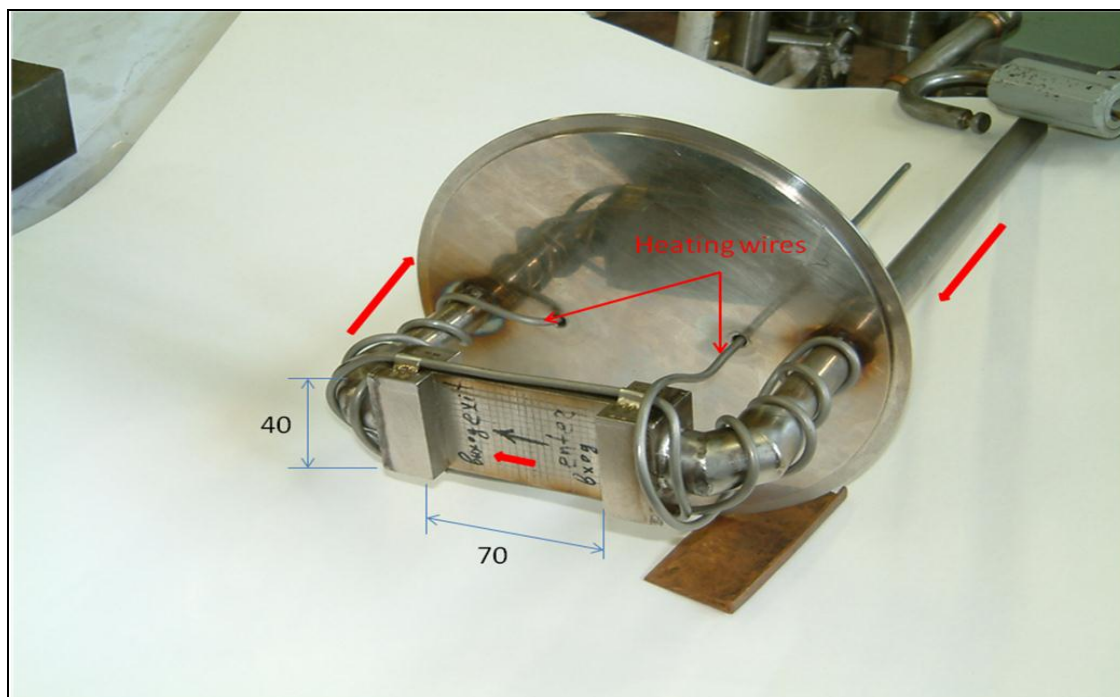


Figure 5.7. The Delay Window equipped of heating wires before the assembling of the test bench.

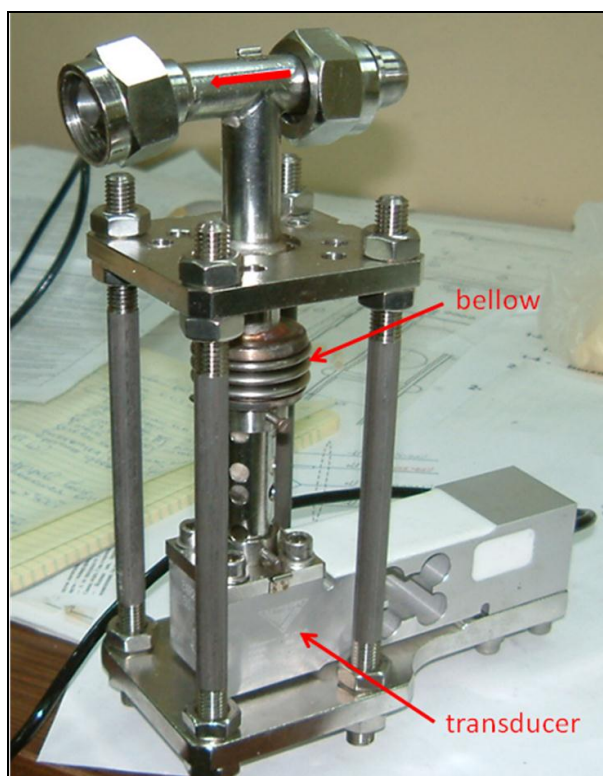


Figure 5.8. The pressure detector ready to be tested.

### 5.2.2. Experimental results

The experiment has multifold purposes and is aimed to demonstrate the performances of the Delay Window as a safety device. In addition, the response of the proposed detection devices are tested. Taking into account that the power density corresponding to 200 kW is about  $70 \text{ kW/cm}^2$ , the e-beam has been focused to furnish a much bigger power density. The minimum e-beam diameter ( $2\sigma$ ) obtained on the Delay Window surface was of 1,7mm. Then, the beam current was

increase till to get the melting of the first wall of the Delay Window. The main design parameters for the Delay Window are summarized in Table 5.5.

**Table 5.5. Main design parameter of the delay window**

Parameter	Measure unit	Value
Thickness of liquid lead jet (100 MeV deuteron)	mm	5
Width of the delay window	mm <sup>2</sup>	70 x 40
Thickness of the walls (Stainless Steel )	mm	2
Velocity of the Liquid PbSn	m/s	1,4
Temperature of liquid lead jet	°C	350
Active protection time in case of failure	s	60

The main results of the experiment are summarized in Table 5.6.

**Table 5.6. Main results of the experiment on the Delay Window prototype**

Parameter	Before melting	After melting
e-beam current	---	45 mA
Beam diameter ( $2\sigma$ )	1,7 mm	1,7 mm
Beam power density	---	120 kW/cm <sup>2</sup>
Time of the measurements	---	120 s
Vacuum pressure	$3,4 \times 10^{-5}$ mbar	$3 \times 10^{-4}$ mbar
Motor absorbed current	28 A	25 A
liquid lead pressure	Unstable	Unstable

The melting of the first wall of the Delay Window was obtained with a beam current of 45 mA, corresponding to a beam power density of about 120 kW/cm<sup>2</sup>. Then, the liquid lead start to flow inside the “collecting chamber” (see Figure 5.9) and the vacuum pressure rapidly drop more than a factor 10, because of the liquid lead vapors.

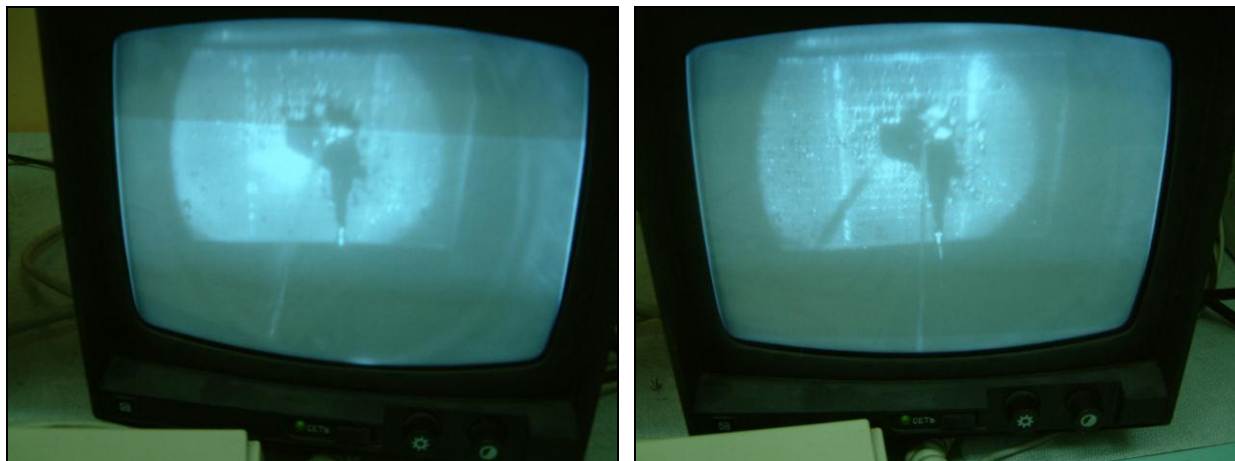


**Figure 5.9.** The liquid lead jet flowing from the Delay Window at the beginning of the measurement (left) and after 5 minutes (right).

At the same time the current absorbed by the driving motor changes from 28 A to 25 A (10%). By the contrary, because of electronic instability it was not possible to define correctly the variation of the pressure. The variation of the pressure before and after the melting of the Delay Window was detectable but not measurable with a good reliability. The total time of the measurement with the e-beam continuously shooting on the Delay Window was of 120 s, two times more than the active protection time demanded for SPIRAL2. After 5 minutes from the melting of the Delay Window all the liquid lead was completely transferred from the “liquid lead tank” to the “collecting chamber”.

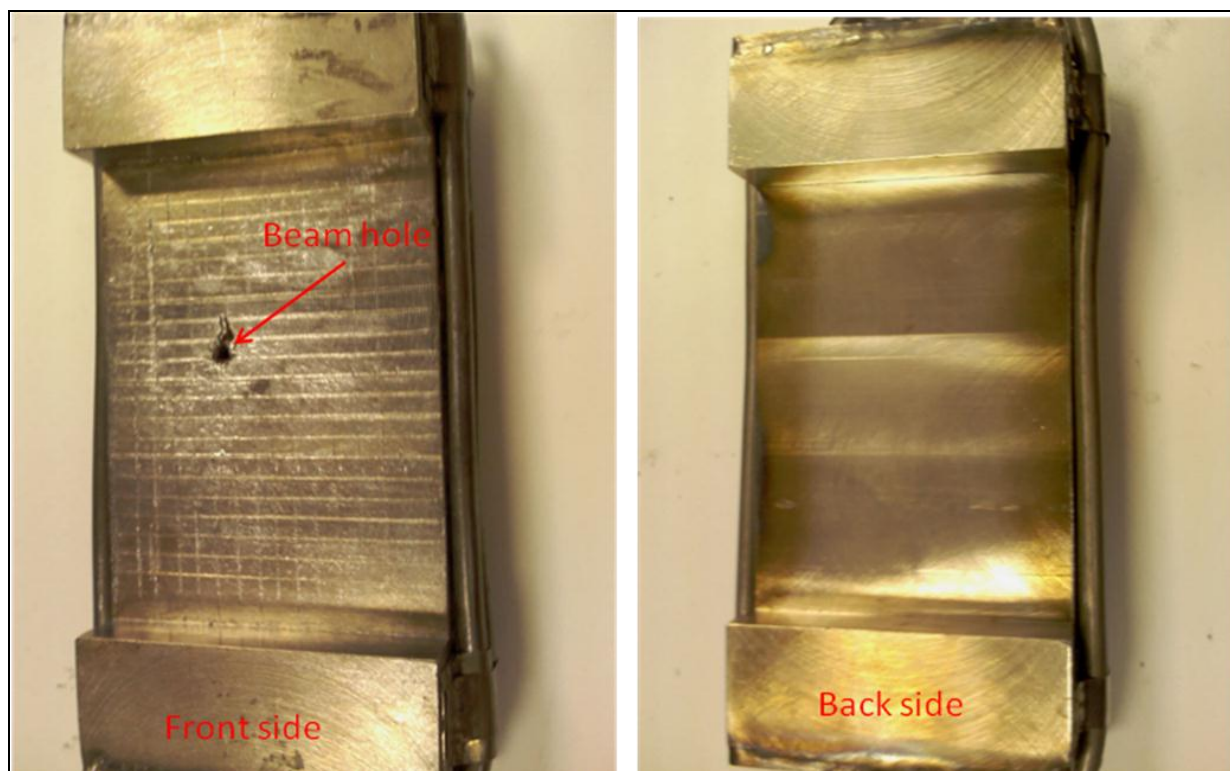


**Figure 5.10.** Visual inspection of the delay window, after the disassembling of the set up.

After having performed the experiment the set up was disassembled to have a visual inspection of the Delay Window and of the flange representing the end of the SPIRAL2 beam vacuum chamber. The Delay Window was cleaned of the residual lead and inspected on both front and back sides. The hole produced by the e-beam on the front wall was measured by an optical microscope and shows a diameter of 1,7 mm; while the back wall was not affected by the beam, as shown in Figure 5.10.

The flange in front to the Delay Window also was inspected (see Figure 5.11) and only a thin deposit of lead vapors was observed inside of the vacuum tube.

### 5.2.3. Long term test

A long term test of the Delay Window has been planned to be performed at LNL and at BINP. The tests will include the following items:

- measurements of pressure and flow rate in function of the rotation frequency of the liquid lead pump;
- measurement of the time reactivity of the pressure detector;
- study of the liquid lead jet from the damaged Delay Window in order to avoid lead contamination in the accelerator.

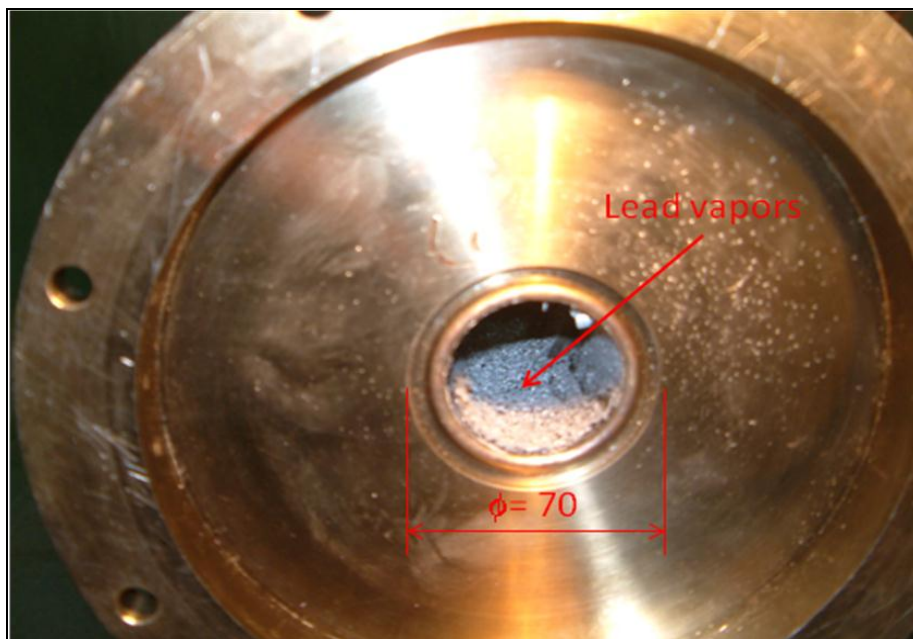


Figure 5.11. Visual inspection of the flange in front to the Delay Window, after the disassembling of the set up.

The test at LNL consist on checking the duration of the liquid lead pump and test the efficiency of the heat exchanger specially designed for the application to the Delay Window. The measurements at BINP will be performed with the e-beam to test the reliability of the Delay Window of realistic size ( $80 \times 5 \text{ mm}^2$ ). The set-up is schematically shown in Figure 5.12 and its picture in Figure 5.13.

The set-up consist mainly of a liquid lead tank containing the lead-tin alloy and a pump specially designed for this application. An external electrical motor is driving the liquid lead pump and make circulating the liquid lead alloy into the Delay Window. After passing through the Delay Window the LPB is going into a cooling system and the additional heat achieved from the converter is released in the heat exchanger. Here the heat from the converter is simulated by an electrical heater located on the surface of the Delay Window. A backing system is used to keep constantly the set-up at the working temperature ( $300 - 320 \text{ }^\circ\text{C}$ ) of the liquid lead.

The backing system is divided in three sections: the liquid lead tank, the Delay Window and the heat exchanger. The temperature is controlled by a set of thermocouples and automatically controlled. The liquid lead pressure and flow rate are measured before and after the Delay Window by means of detectors specially designed for this purpose.

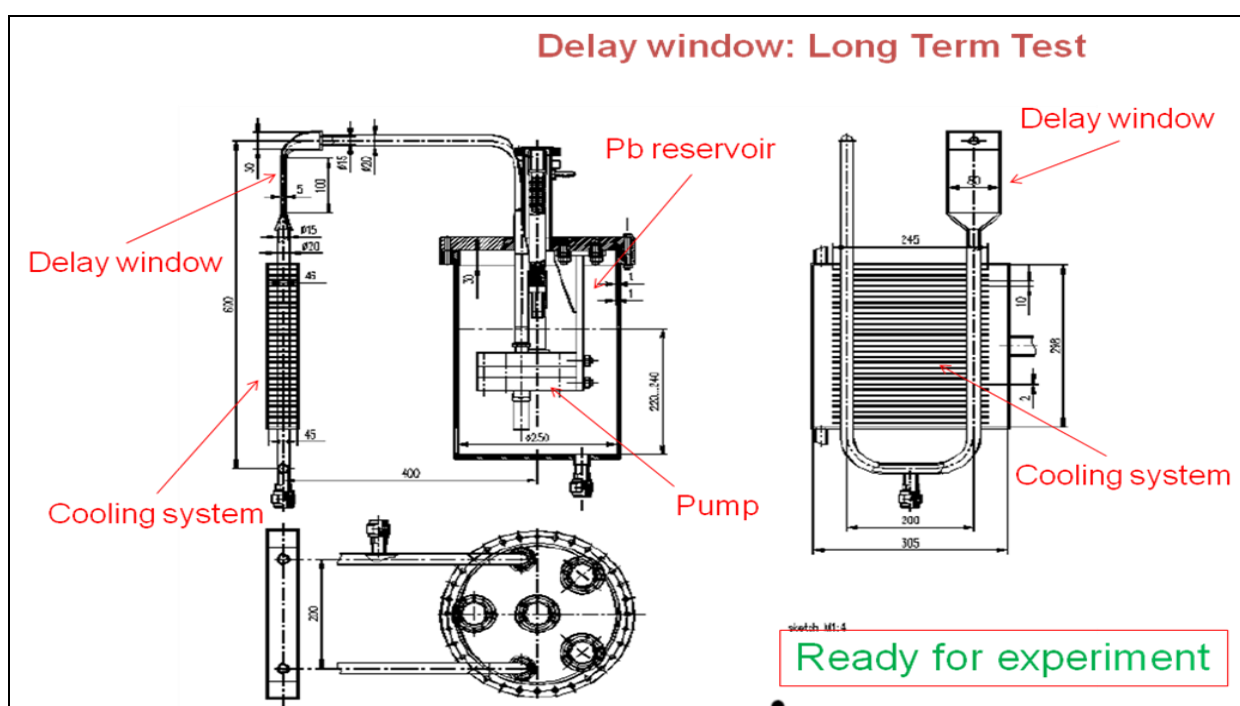


Figure 5.12. A sketch of the set-up for the long term tests of the Delay Window.



**Figure 5.13.** A picture of the set-up for the long term experiment of the Delay Window.

### ***5.3. Ball Bearings Test***

The ball bearing have to satisfy the following demands: operate at high temperature (250-300 °C), resist to high temperature's gradient (150 °C), rotate in a vacuum environment at the rotation frequency range of 5 - 20 Hz, in absence of lubricant. The minimum operational time is as long as one operation cycle (90 days) of the SPIRAL-2 Facility. For such a reason three different kinds of bearing have been proposed and tested at LNL.

#### ***5.3.1. Experimental Set-up***

A test bench system was prepared to evaluate the ball bearings and their performance during 90 days of continuous operation, corresponding to one operation cycle of the SPIRAL-2 Facility. (see Figure 5.14).

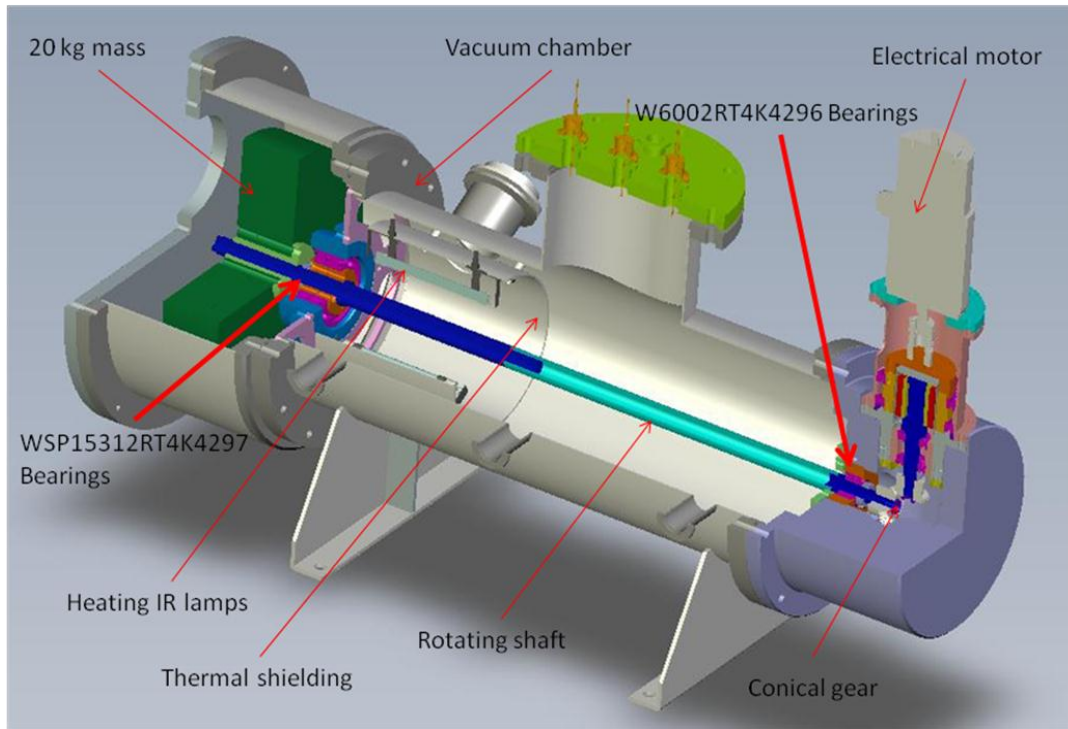


**Figure 5.14 – View of the test bench.**

The testing system is composed by a vacuum chamber with a rotating shaft along the horizontal axis. A mass of 20 kg is positioned at the ending of the shaft, simulating the weight of the graphite converter. Three infrared lamps [2] are installed at the internal of the chamber, just over the shaft and covered by a thermal shielding. The IR lamps supplies the heat and consequently the heated shaft transmit the heat to the bearings by thermal conductance. A turbo-molecular pump is used for evacuate the chamber and a Pfeiffer compact full range gauge [3] is used for vacuum measurement. An electrical DC motor [4] is connected to the shaft at 90° by a conic gear, providing rotation to the mass system. The complete system for the ball bearing test was designed and tested at the Laboratori Nazionali di Legnaro - Italy (see Figure 5.15).

The system is managed by a LabWindows program allowing remote control and monitoring through a Programmable Automation Controller (Field Point) [5]. The main control is done over the motor turns by analogical command of the voltage applied. For the motor monitoring are employed its current and frequency, obtained as analogical signals. The temperature is monitored by a double system of measurements, a K type thermocouple welded on the thermal shielding inside the vacuum chamber near the shaft and a Impac® IP-140 infrared-pyrometer [6] reading the temperature over the shaft in the nearest to the bearing. The vacuum and the vibrations of the system are also monitored.

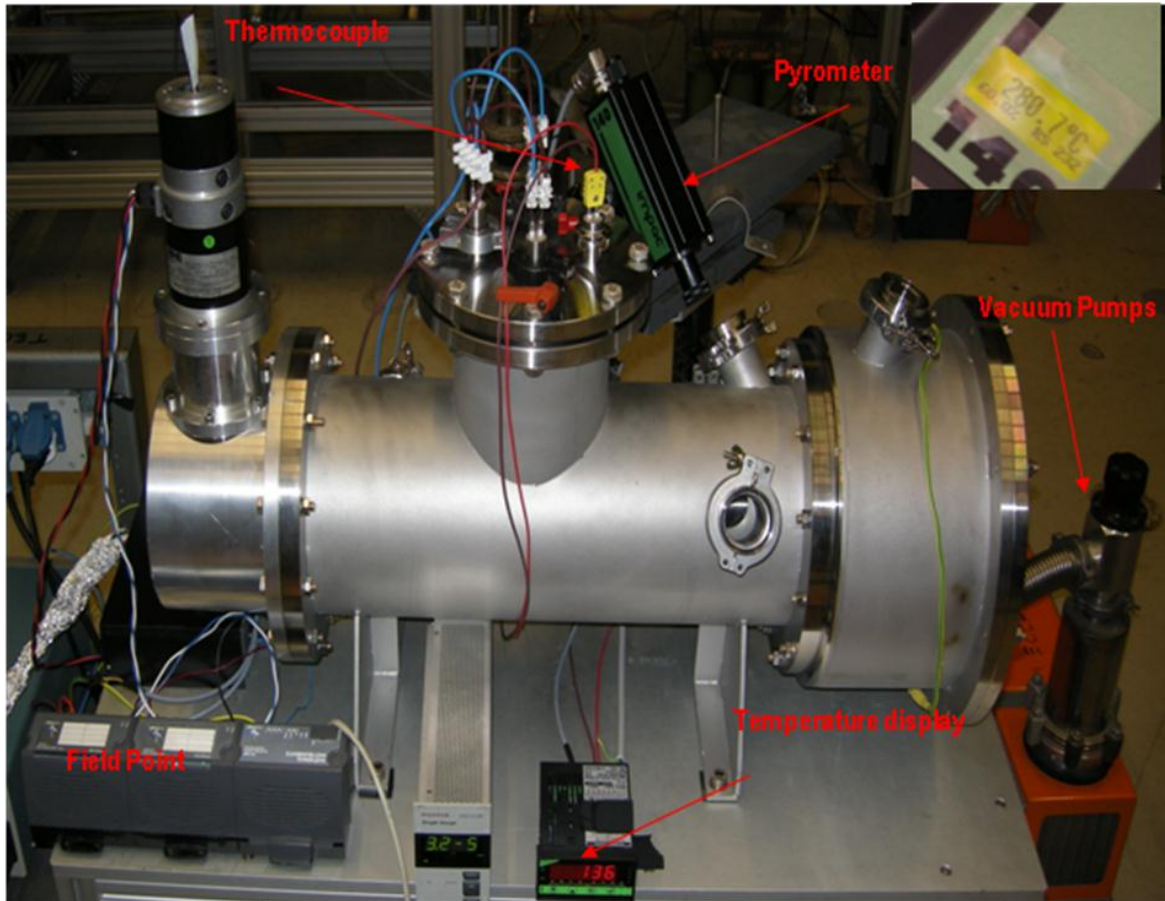


**Figure 5.15. Picture of the test bench at the Legnaro National Laboratories.**

The ball bearings used for this test were produced and supply by the company ADR [7]. Three different kind of bearings were proposed, their main characteristics are presented in Table 5.7.

Mechanical drawing of bearing WSP15312RT4K4297 and the corresponding picture are shown in Figure 5.1.

The bearing W6001RT4K4298 model is shown in

Figure 5.17, in the “galel” configuration. In this case are required four bearing around the shaft. The main advantage of this disposition is the reduction of the speed rotation of bearings.

For this test experiment the model WSP15312RT4K4297 was selected, mainly due to economical reasons, using less specials bearings for testing.

The third kind of bearings, the model W6002RT4K4296, was design to be installed on the shaft, in the nearest part to the electrical motor. In this region the bearings are subject to less severe conditions respect to the converter one. The local temperature is less than 50 °C and the gradient of temperature experiences by bearings is practically negligible. The mechanical drawing and its photograph are shown in Figure 5.18. .

*Table 5.7 - Ball bearing characteristics.*

Bearing characteristic	WSP15312 RT4K4297	W6001 RT4K4298	W6002 RT4K4296
Material codification	W	W	W
Rings material	Stainless Steel AFNOR X40CrMoVN16.2/ XD15NW	Stainless Steel AFNOR X40CrMoVN16.2/ XD15NW	Stainless Steel AFNOR X40CrMoVN16.2/ XD15NW
Hardness	675 HV mini	675 HV mini	675 HV mini
Temperature of use Max	<500 °C	<500 °C	<500 °C
Balls material	Ceramic AFNOR Si3N4	Ceramic AFNOR Si3N4	Ceramic AFNOR Si3N4
Hardness	1050HV 10 mini	1050HV 10 mini	1050HV 10 mini
Cage Material	Stainless Steel X105CrMo17/ AISI:440C	Stainless Steel X105CrMo17/ AISI:440C	Stainless Steel X105CrMo17/ AISI:440C
Lubricant	MoS2 Coating < 1 µm	MoS2 Coating < 1 µm	MoS2 Coating < 1 µm
Holes	40 mm	12 mm	15 mm
External Diameter	68 mm	28 mm	32 mm
Thickness	30 mm (2x15)	8 mm	9 mm
Number of balls	20 (2x10)	8	9
Nominal contact angle	25°	15°	15°

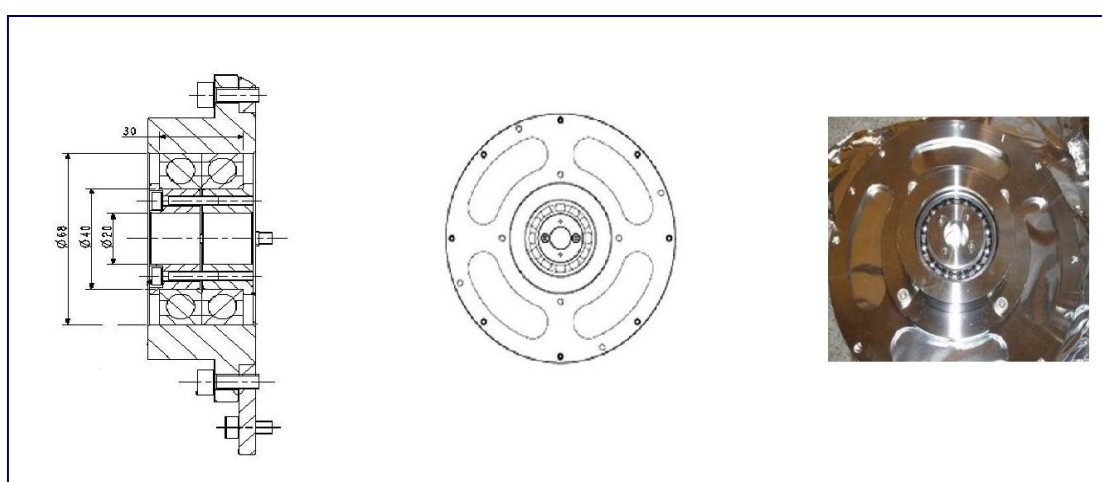
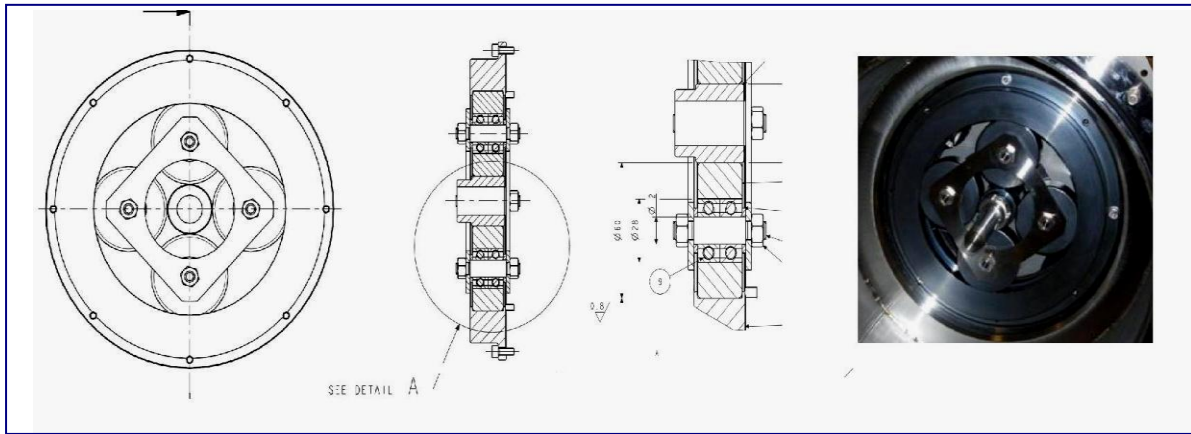


Figure 5.16. Bearing WSP15312RT4K4297. LEFT: mechanical drawing, RIGHT: photograph of the bearings installed on the test set-up.



**Figure 5.17 - Bearing W6001RT4K4298. LEFT: mechanical drawing design, RIGHT: photograph of the bearings installed on the test set-up.**



**Figure 5.18. - Detail of W6002RT4K4296 bearing. LEFT: mechanical drawing. CENTER: photography of the shaft ending with the conic gear corresponding to the mechanical drawing. RIGHT: photography of the conic gear connected to the electrical motor.**

### *5.3.2. Experimental Results*

The evaluation of the bearing was planned to be carried out during 90 days. A very first evaluation was done without heating with IR lamps in order to establish the base level of the system. The parameters used for establishment of base level and for 90 days experiments are presented on Table 5.8.

For the 90 days experiment, the rotation frequency of the shaft was set at 7 Hz (420 turns per minute) and the temperature was set at 270°C controlling the voltage applied to the IR lamps. The operational vacuum level was of  $\sim 10^{-6}$  mBar. The LabView data acquisition system records the data and display them on the computer screen. A typical view of the displayed data are shown in Figure 5.19.

**Table 5.8. Setting of the parameters for the 90 days experiment.**

Parameter	Base Level	90 days
Motor Voltage	4.0 V	4.0 V
Motor frequency	~ 7.0 Hz	~ 7.0 Hz
Vacuum Level	~10 <sup>-5</sup> mBar	~10 <sup>-6</sup> mBar
Temperature	25°C	270°C

The motor driver was controlled by the applied voltage while the frequency and absorbed current are continuously monitored. The temperature indicated on the screen correspond to that measured by the thermocouple welded to the thermal shielding. Independently, the IR pyrometer allows to define the real temperature on the shaft. The pressure on the vacuum chamber is also monitored. The results obtained in terms of current absorbed, rotation frequency and shaft temperature are shown in Figure 5.20, for all 90 days experiment. The average rotation speed corresponds to about 420 turns per minute.

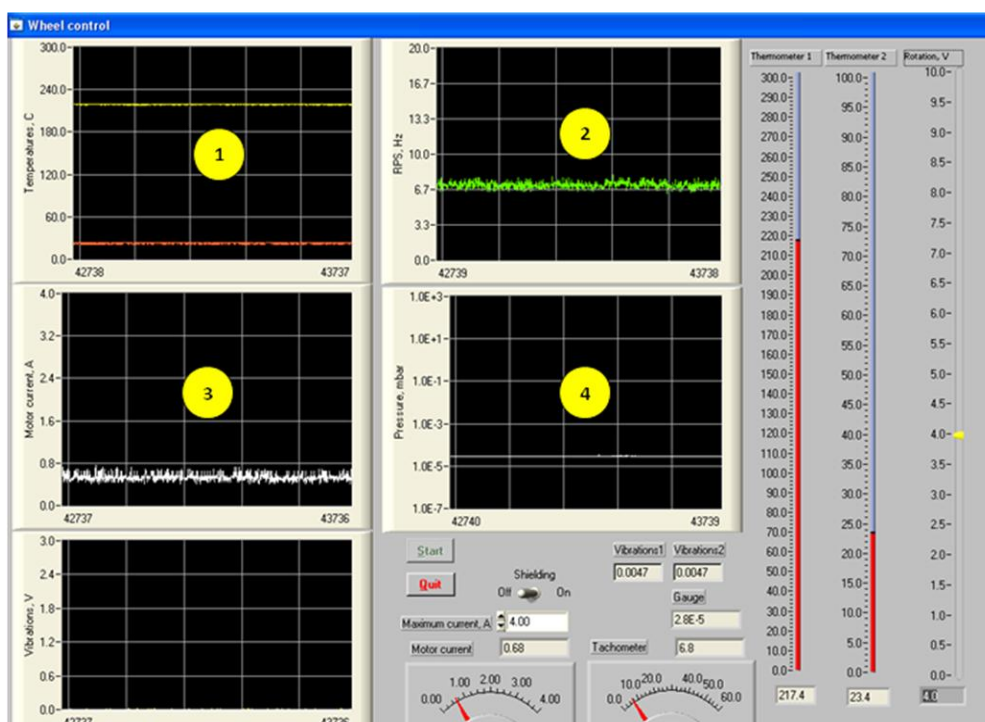


**Figure 5.19. An example of the display of the data of the test bench observed during the 90 days-experiment. Graphs in function of time: 1) temperature, 2) rotation frequency, 3) motor current, and 4) pressure in vacuum chamber; and indicators of the instant value of the main parameters are also shown.**

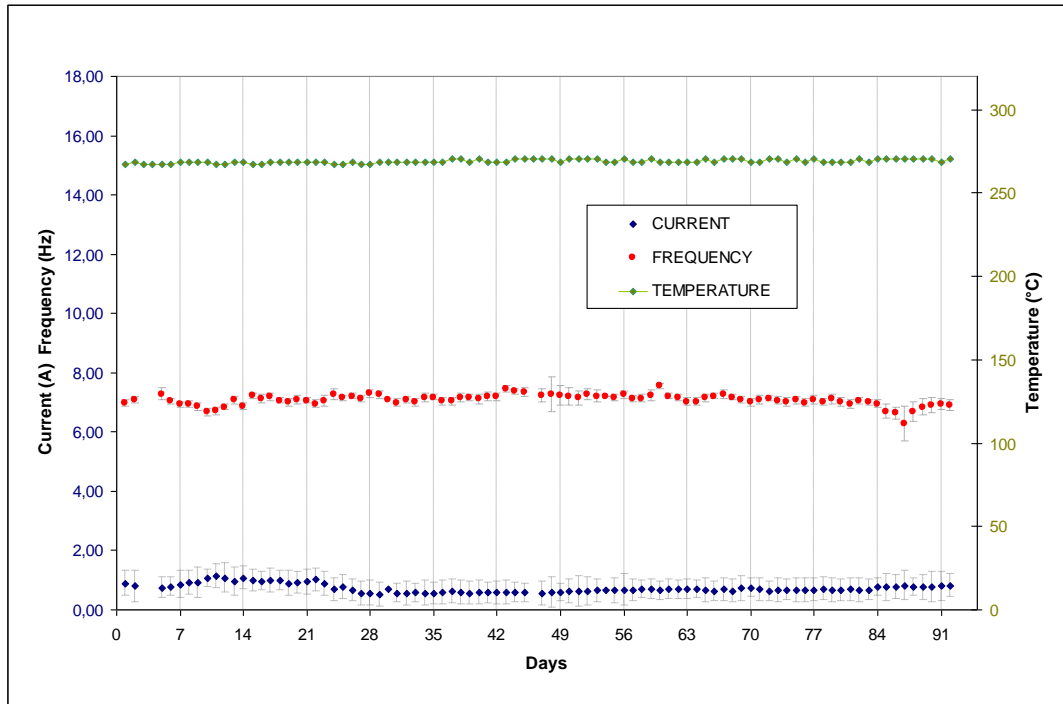


**Figure 5.20 - Results of 90 days experiment; motor current, rotation frequency and shaft temperature are reported in function of time (days).**

For monitoring, were carried out at least 60 measurements every day during 92 days precisely. The results observed in Figure 5.20 are the average calculated each day. On the basis of the data, statistical variation of measurements were determined. The variations related to the current and frequency were calculated. The absolute error of current and rotation frequency measurements are 10.9% and 3,62%, respectively. The reported measurements errors are acceptable for the objectives of the research. Motor current and motor frequency values are stable, statistical variations can be explained considering the electronic dead time of the motor controller.

Also the vibration levels of the system were monitored. The signals acquisition was done using an accelerometer coupled to VBA-Wintek [8] program. Analysis of spectral density of power (PSD), RMS and peak of vibration were done, monitoring during 2 hours each, 5 times/day. A vibration base-level was determined using only the vacuum pump turned on. The spectra obtained was used to compare the performance of the system relatively to the base condition. The RMS and peak base-level and an example of the RMS and Peak of 90 days experiment can be seen in Figure 5.21 and Figure 5.22.

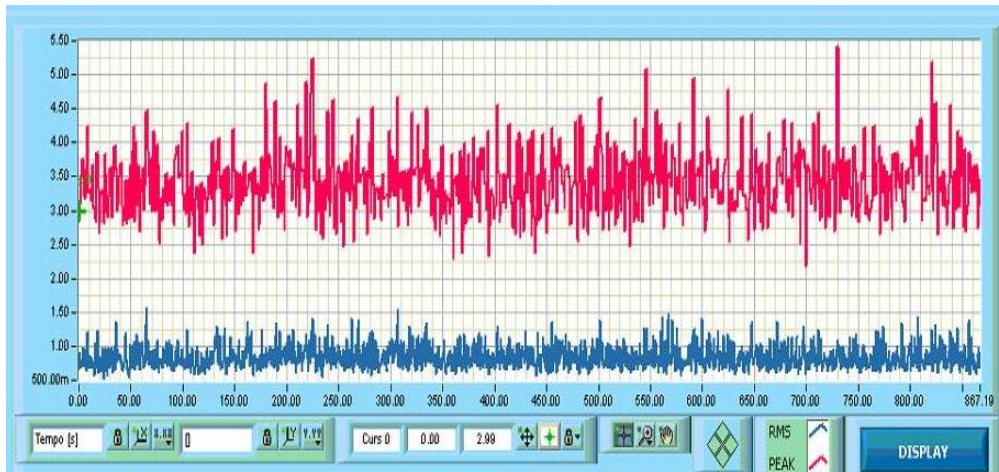


**Figure 5.21. Vibration base-level with only vacuum pump turned ON. Measurement duration 30 minutes. Results are shown as peaks and RMS of the acceleration in  $\text{m/s}^2$  in function of time. Red: peak signal, Blue: RMS signal.**

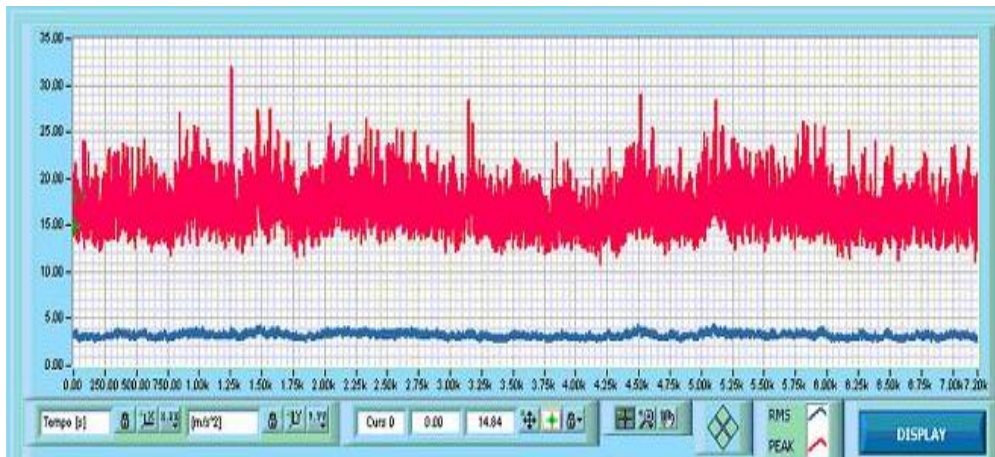


**Figure 5.22. An example of vibration analysis of the test bench for 90 days experiment. Results are shown as peaks and RMS of the acceleration in  $\text{m/s}^2$  in function of time. Duration of measurement: 2 hours. Red: peaks signal, Blue: RMS signal.**

An increasing of the vibration level was observed when rotation was turned ON, reaching even 5 times the vibration base-level. This behavior was expected considering the influence of all mechanical components, and their resonances, on the measurements, consequently was assumed as normal operation condition of the system. Variations above 5 times the RMS base level, were defined as an indication of a threshold of the performance of the ball bearings. Still during the 90-days experiment variations were not evidenced.

Summarizing, the bearings WSP15312 RT4K4297 were tested continuously during 92 days under vacuum, operating at  $270^\circ\text{C}$  and 7.0 Hz. The results satisfy completely the performances demanded for the application to the SPIRAL2 neutron converter.

#### 5.4. Additional Experiments

Based on the results obtained during the 90-days experiment, was possible to continue the evaluation of the bearings. A series of 3 experiments, one week each, were carried out. The main objective was to assess the performance of the bearings at higher temperatures and rotation frequencies. The motor frequency was increased in two step until 13 Hz and the temperature up to 320 °C. The setting parameters used for these experiments are presented on Table 5.9. The experimental results obtained for the main parameters studied, are presented on Figure 5.23.

Table 5.9. Setting of parameters for the additional experiments.

Parameter	1st week	2nd week	3rd week
Motor Voltage	4.0V	5.2V	7.0V
Motor frequency	~ 7.0 Hz	10.0 Hz	13.0 Hz
Vacuum Level	~10 <sup>-6</sup> mBar	~10 <sup>-6</sup> mBar	~10 <sup>-6</sup> mBar
Temperature	320°C	320°C	320°C

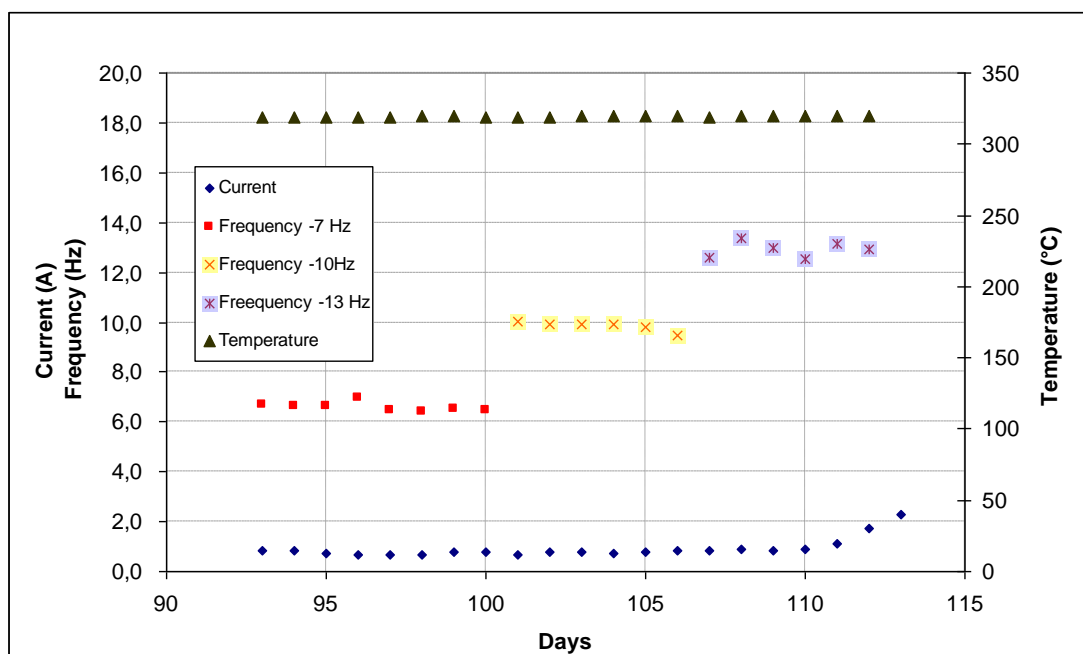
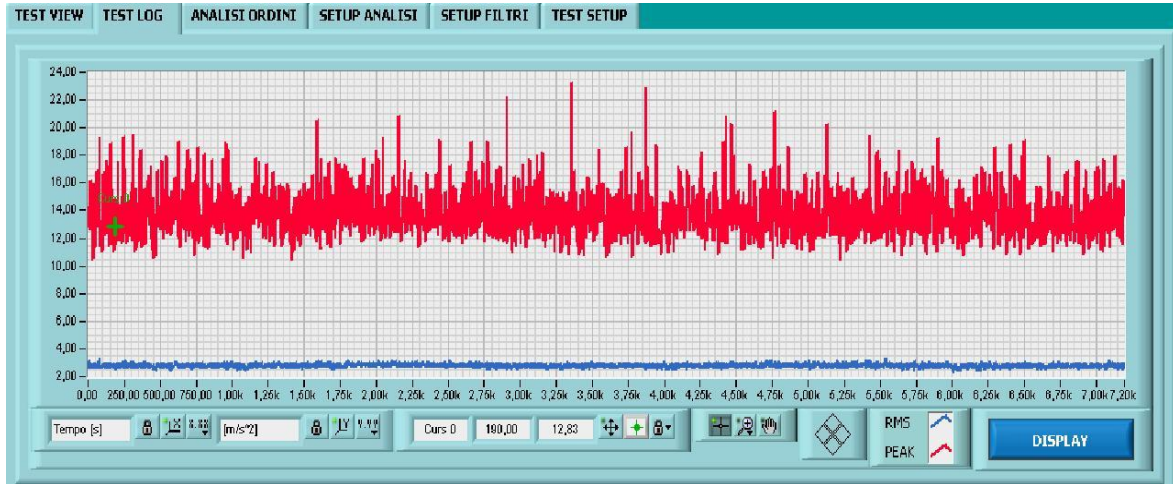


Figure 5.23. Variation of current and frequency at T~320°C. The experiments starts the 93th day of operation.

The results show similar values of the current absorbed by motor at 7.0 Hz and 10.0 Hz (during the first 2 weeks) and an increasing of the current absorbed when operating at 13 Hz of frequency. In addition, there were no evidence of significant changes on the vibration levels during three weeks. (See Figure 5.24).



**Figure 5.24.** An example of vibration analysis of the last three weeks experiments. Results are shown as peaks and RMS of the acceleration in  $\text{m/s}^2$  in function of time. Duration of measurement: 2 hours. Red: peaks signal, Blue: RMS signal.

## CONCLUSIONS

- The prototype of the neutron converter target has been successfully tested from the thermo-mechanical point of view by using a powerful electron beam. Two kinds of material converters have been tested: the MPG graphite and a new kind of graphite ad hoc developed made of  $^{13}\text{C}$  isotope. The MPG graphite has shown very good characteristics even if operating at severe conditions, while the  $^{13}\text{C}$  material needs additional development and improvement.
  - The operation at nominal conditions (50 kW) gives good results and demonstrates that the prototype can work for a long time in stable conditions.
  - Comparing the graphite properties to the thermo-mechanical calculations it is clearly visible that the converter will operate with a good safety margin, respectively for the 50 kW and 200 kW regime. The same results are concerning the metal parts of the converter (spokes) made in INCONEL 600 that shown an ultimate strength of 650 MPa.
  - The experimental measurement of the temperatures and numerical calculations (ANSYS) showed to be in good agreement. The comparison allowed to come to a conclusion about the appropriateness of the developed method of numerical calculations in a thermo-mechanical analysis of a neutron production target within the wide range of loads applied. The cooling channels dissipate almost all of the heating power radiated from the converter.
  -
-

## REFERENCES

- [1] *The SPIRAL2 Project – APD Report*, January 2005 (rif. EDMS I-004609\_V1.0)
  - *Technical Report of the Radioactive Beam Section*, December 2007 (rif. EDMS I-011805\_V1.0)
  - [2] O. Alyakrinskiy, A. Antoshin, M. Avilov, D. Bolkhovityanov, S. Fadeev, V. Golikov, K. Gubin, N. Lebedev, P. Logatchev, V. Popov, S. Shiyankov, L.B. Tecchio ; Nucl. Instrum. and Meth. in Phys. Res. A578 (2007) 357-369.
  - [3] *Properties and Characteristics of Graphite*; POCO-Graphite Inc., [www.poco.com](http://www.poco.com).
  - [4] J. Bermudez, L.B. Tecchio, E. Udup; *Test of Ball Bearings for the Neutron Converter* (rif. EDMS SP2\_DT\_8324\_I-020633V1.0)
  - [5] G. Heidenreich; *Meson Production Target at PSI*, 2<sup>nd</sup> High-Power Targetry Workshop, Oak Ridge, TN, October 10-14, 2005.
  - G. Heidenreich et al.; *Improvement of the Operational Reliability of Target E*, PSI-Scientific Report 1998, Vol. VI, p. 16.
  - [6] Y. Huguet ; *Cahier des Charges Relative ° l'Etude et la Réalisation d'un Moteur Electrique pour le Convertisseur de SPIRAL2*, (rif. EDMS SP2\_CC\_8324\_I-020981\_V1.0).
  - [7] L.B. Tecchio, M. Tonezzer. M. Loriggiola, M. Lollo; *Measurement of the Graphite Evaporation: Addendum*, (rif. EDMS SP2\_DT\_8324\_I-015959\_V1.0)
  - [8] G. Normand; *Calculs d'erreurs pour les deutons 50 et 200 kW pour la LHE-production*, 23 Mars 2010, Version 1.0.
  - [9] M. Avilov, M. Blinov, J. Bermudez, K. Gubin, P. Logatchev, D.G. Modestov, V.V. Plokhoi, S.I. Samarin, S. Shiyankov, L.B. Tecchio, E. Udup ; *The Delay Window, Dossier de Justification de la Definition*, (rif. EDMS SP2\_DT\_8324\_I-020743\_V1.0).
  - [10] P. Logatchov et al.; *Report on the Fulfillment of the ISTC Project #3682 During the First Year*, (rif. EDMS SP2\_DT\_8324\_I-015958V\_1.0).
  - [11] J. Bermudez, L.B. Tecchio, E. Udup; *Dossier de justification de la definition (DJD) – The neutron converter design*, (rif. EDMS SP2\_DT\_8324\_I-020637\_V1.0).
  - [12] M. Blinov, K. Gubin, P. Logatchev, L.B. Tecchio; *Preliminary Tests of the Delay Window*, (rif. EDMS SP2\_NT\_8324\_I-018108\_V1.0).
  - [13] J. B. Marion and J.L. Folwer. *Fast neutron Physics*. INTERSCIENCE PUBLISHERS, Inc. New York 1960. Russian edition: Fast neutron physics. Volume 1: Experimental technique. Moscow, GOSATOMIZDAT Publishers, 1963.
  - [14] A.A. Samarsky, *Introduction to numerical methods*. Moscow, NAUKA Publishers, 1987.
  - [15] Nelder J.A., Mead R.A., *Simplex Method for Function Minimization // Computer Journal*. Vol. 7,P. 308 - 313).
  - [16] Table of Isotopes. Eighth edition by Richard B. Firestone. CD Version 1.0 March 1996. WILEY INTERSCIENCE.
  - [17] V.T. Gromov, *Introduction to the radiation physics of solid*. RFNC-VNIITF Publishers, Snezhinsk, 2007.
  - [18] L.B. Begrambekov, A.A. Gordeyev, E.A. Milyaeva, P.L. Leykin, P.A. Shigin, O.I. Buzhinsky, T. Tanabe, *Hydrogen sorption in graphite and carbons for low-energy ion implantation*. J. MATERIALOVEDENIE, #7, 2006.
-

- [19] Y.S. Nechayev, *The nature of hydrogen sorption by carbon nanomaterials and prospects of developing a superabsorber*. J. MATERIALOVEDENIE, #2, 2006.
  - [20] M.T. Robinson and O.S.Oen. Appl. Phys. Lett. 2 (1963) 30.
  - [21] M.T. Robinson and I.M. Torrens, Phys. Rev. B 9 (1974) 5008.
  - [22] J. F. Ziegler, *TRIM-91 User Manual*, IBM-Research, 28-0 Yorktown, New York 10598 (1991).
  - [23] V.V. Dremov, F.A. Sapozhnikov, S.I.Samarin, D.G. Modestov, N.E. Chizhkova. *Monte-Carlo + Molecular Dynamics Modeling of Radiation Damages in Pu*. Journal of Alloys and Compounds. 444 - 445 (2007) 197 - 201.
  - [24] S.I. Samarin and V.V. Dremov, *Calculation of the distribution of primarily displaced atoms in graphite*. Presentation at ISTC 3682 Meeting in Novosibirsk, 19-23 May 2008.
  - [25] G. Acosta, M. Blinov, J. Bermudez, P. Logatchev, S. Shiyankov, L.B. Tecchio, E. Udup, V. Zaitsev; *Report on the Test of Delay Window*, (rif. EDMS SP2\_NT\_8324\_I-022737\_V1.0).
-